Master's Theses

Master's Theses and Graduate Research

1991

Magnetism, superconductivity, and muon bonding in $RBa_2Cu_3O_{6+}$[delta] oxides

Wayne Dawson

San Jose State University

Follow this and additional works at: https://scholarworks.sjsu.edu/etd_theses

INFORMATION TO USERS

This manuscript has been reproduced from the microfilm master. UMI films the text directly from the original or copy submitted. Thus, some thesis and dissertation copies are in typewriter face, while others may be from any type of computer printer.

The quality of this reproduction is dependent upon the quality of the copy submitted. Broken or indistinct print, colored or poor quality illustrations and photographs, print bleedthrough, substandard margins, and improper alignment can adversely affect reproduction.

In the unlikely event that the author did not send UMI a complete manuscript and there are missing pages, these will be noted. Also, if unauthorized copyright material had to be removed, a note will indicate the deletion.

Oversize materials (e.g., maps, drawings, charts) are reproduced by sectioning the original, beginning at the upper left-hand corner and continuing from left to right in equal sections with small overlaps. Each original is also photographed in one exposure and is included in reduced form at the back of the book.

Photographs included in the original manuscript have been reproduced xerographically in this copy. Higher quality 6" x 9" black and white photographic prints are available for any photographs or illustrations appearing in this copy for an additional charge. Contact UMI directly to order.

U·M·I

Magnetism, superconductivity, and muon bonding in RBa_2Cu_3 $O_{6+\delta}$ oxides

Dawson, Wayne Kenneth, M.S.

San Jose State University, 1992

MAGNETISM, SUPERCONDUCTIVITY, AND

MUON BONDING IN $RBa_2Cu_3O_{6+\delta}$ OXIDES

A Thesis

Presented to

The Faculty of the Department of Physics

San José State University
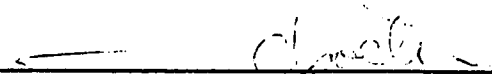
In Partial Fulfillment

of the Requirements for the Degree
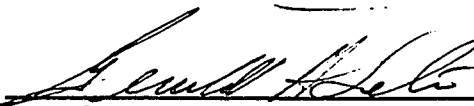
Master of Science

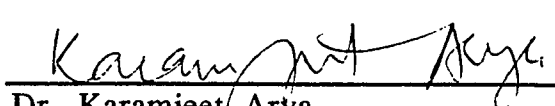By

Wayne Dawson

December, 1991

APPROVED FOR THE DEPARTMENT OF PHYSICS
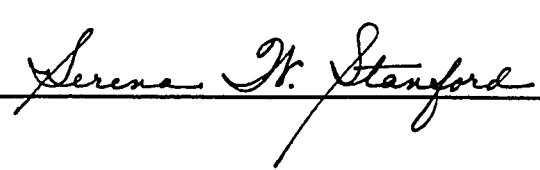
_____
Dr. Carel Boekema

_____
Dr. Gerald Selter

_____
Dr. Karamjeet Arya

APPROVED FOR THE UNIVERSITY

_____

ABSTRACT

MAGNETISM, SUPERCONDUCTIVITY, AND MUON BONDING IN $RBa_2Cu_3O_{6+\delta}$ OXIDES

by Wayne K. Dawson

Muon spin relaxation (μSR) has been used in conjunction with search calculations to find the nature and location of the muon sites in non-superconducting $RBa_2Cu_3O_{6+\delta}$ ($0.0 < \delta < 0.5$) and superconducting $RBa_2Cu_3O_{6+\delta}$ ($0.5 < \delta < 1.0$), where R corresponds to the rare-earth ions. The search method employs two independent methods: magnetic-dipole-field calculations and potential-energy calculations. The results consistently indicate that the Balmer(2) site is a strong candidate for muon-oxygen bonding. Other sites are also observed which are dependent on the oxygen content (δ). The muon-stop sites were used to predict the magnetic structures of both $PrBa_2Cu_3O_7$ and $PrBa_2Cu_3O_6$. The μ^+-sites were also used to locate the proton sites in $H_xYBa_2Cu_3O_7$. The location of the proton sites implies a correspondence between hydrogen and muon bonding for the novel transition metal oxides. Finally, interpretations are made about the mechanism of high temperature superconductivity, based in part on μSR data.

Acknowledgements

I *gratefully* acknowledge and extend sincere appreciation to the following people, contributors, institutions, and companies.

§ § §

§ My advisory committee, who have made incalculable contributions to my own future and prosperity over the years during which I have known them: Dr. Karamjeet Arya, Dr. Carel Boekema, and Dr. Gerald Selter.

§ D. Wayne Cooke, who has carried on the LAMPF-μSR program which allowed this research to be possible, and Marshall Maez and Bryan Bennett, who provided technical support in the μSR work at LAMPF.

§ Roger L. Lichti, who provided me with extensive insight into the concepts behind μSR at LAMPF, and an understanding of the electronics associated with such experiments.

§ Kwai-Chow Chan and Chris Halim, who have helped me in the development of my computational programming background.

§ Jeff A. Flint and Stephen P. Weathersby, who have worked with me in μSR data acquisition and analysis and helped me understand the data analysis programs.

§ Art Chavez and the rest of the staff at the DAC who provided me with technical support and the computer time on the VAX.

§ Convergent Technologies (now Unisys) who contributed a miniframe computer which provided a substantial part of the computational data through out this work.

Dedication

To my friends and family, who encouraged me to carry through with my dreams and visions when I had no energy left to fight for them. Those who kept me focused on the fundamental principle of scientific investigation:

When proposing the solution to a physical problem, the simplest solution is often the best--Occum's razor.

Table of Contents

List of Figures

List of Tables

Glossary of Term Symbols and Abbreviations

<u>Roman Symbols Used in Abbreviations</u>:

A1, A2	<u>A</u>rt 1 (A1) and the <u>A</u>rt 2 (A2) muon-stop sites in R123y, <u>A</u>rt sites are denoted by A.
a, b, c	The lattice constants in an orthorhombic crystal lattice.
AFM	<u>A</u>nti<u>f</u>erro<u>m</u>agnetic
amu	<u>a</u>tomic <u>m</u>ass <u>u</u>nits.
B	<u>B</u>rutus muon-stop site in R123y.
B1, B2	<u>B</u>almer 1 and <u>B</u>almer 2 muon-stop sites in R123y.
BCS	<u>B</u>ardeen-<u>C</u>ooper-<u>S</u>chriffer.
B.G.	The <u>B</u>ack <u>G</u>round decay events in a muon spectrum.
C	<u>S</u>on muon-stop site in R123y.
D1, D2	<u>D</u>enny 1 (D1) and <u>D</u>enny 2 (D2) muon-stop sites in R123y, <u>D</u>enny sites are denoted by D.
DEM	<u>D</u>awson-<u>E</u>wald <u>M</u>ethod.
ESR	<u>E</u>lectron <u>S</u>pin <u>R</u>esonance
F, B, U, L	The counters (<u>F</u>ront, <u>B</u>ack, <u>U</u>pper, <u>L</u>ower) on a muon spectrometer.
FM	<u>F</u>erro<u>m</u>agnetic
GCD	<u>G</u>aussian <u>C</u>harge <u>D</u>istribution.
HF	<u>H</u>artree <u>F</u>ock.
High-T_c	<u>H</u>igh transition temperature (T_c)
INS	<u>I</u>nelastic <u>N</u>eutron <u>S</u>cattering
IR	<u>I</u>nfra<u>r</u>ed spectroscopy
L12	<u>L</u>in 1 and/or <u>L</u>in 2 muon-stop sites in R123y.
LAMPF	<u>L</u>os <u>A</u>lamos <u>M</u>eson <u>P</u>hysics <u>F</u>acility.
LY	<u>L</u>ynn model.
MDF	<u>M</u>agnetic <u>D</u>ipole <u>F</u>ield.
MES	<u>M</u>össbauer <u>E</u>mission <u>S</u>pectroscopy.
MP	<u>M</u>orse <u>P</u>otential.
MPw/CT	<u>M</u>orse <u>P</u>otential <u>w</u>ith <u>C</u>oulombic <u>T</u>ail.
MR	<u>M</u>agnetic <u>R</u>esonance
μSR	<u>M</u>uon <u>S</u>pin <u>R</u>elaxation.
NMR	<u>N</u>uclear <u>M</u>agnetic <u>R</u>esonance
NQR	<u>N</u>uclear <u>Q</u>uadrupole <u>R</u>esonance
Oe	<u>O</u>erstad (a comparable unit for Gauss in magnetism).
PE	<u>P</u>otential <u>E</u>nergy.
R	Denotes any one of a specified set of the <u>R</u>are Earth ions.
R123y	$RBa_2Cu_3O_{6+\delta}$ crystal structure.
RHF	<u>R</u>estricted <u>H</u>artree <u>F</u>ock.

RHF-SCF	Restricted Hartree Fock Self Consistent Field.
RRP	Rodriguez/Rüegg Potential.
RT	Room Temperature
SC	Superconductivity
SCF	Self Consistent Field.
SJSU	San Jose State University.
T	Temperature.
T_c	Superconducting transition Temperature.
TF	Transverse Field.
TMS	Tri-methyl-Silane
T_N	Néel transition Temperature.
TQ	Tranquada model.
UHF	Unrestricted Hartree Fock.
UHF-SCF	Unrestricted Hartree Fock Self Consistent Field.
ZF	Zero Field.
ZF-μSR	Zero Field Muon Spin Relaxation.
ZP	Zero-Point.

Greek Symbols Used in Mathematical Equations:

α	Symbol used in the Morse potential (in units of Å^{-1}).
β	Constant denoting effective charge.
δ	Chemical shift in the NMR spectrum.
Δ	Volume of an orthorhombic cell (Δ = abc).
ΔV_μ	Distribution of potential energy in the zero point region of the muon site.
γ_H	Gyromagnetic ratio for a proton.
γ_I	Gyromagnetic ratio for a particle I.
γ_μ	Gyromagnetic ratio for the muon.
η	Symbol used in the Lippincott potential (in units of Å^{-1}).
λ	Exponential relaxation rate of the muon.
μ_B	Bohr Magneton (9.27×10^{-24} J/T).
μ_o	magnetic permeability constant.
ω	Angular frequency of precessing particle.
ω_μ	Angular frequency of precessing muon.
ω_H	Angular frequency of precessing proton.
σ	Gaussian relaxation rate of the muon.

<u>Chemical</u> <u>Formulas</u> <u>in</u> <u>Abbreviated</u> <u>Form</u>:

β^+ Positron (e^+) or positive beta particle (the $\overline{}$ over the top of the e^+ indicates anti-matter).

β^- negative beta particle (matter).

e^- Electron.

$H_x Y1237$ $H_x YBa_2 Cu_3 O_7$.

μ^+ muon.

ν_e Electron-type neutrino.

$\overline{\nu_e}$ Electron-type antineutrino.

ν_μ Muon-type neutrino.

$\overline{\nu_\mu}$ Muon-type antineutrino.

π^+ Pion particle.

p^+ Proton (H^+).

R   Rare Earth (a general term indicating a specified set of rare earth ions).

$R123y$ $RBa_2 Cu_3 O_y$.

$R123(6+\delta)$ $RBa_2 Cu_3 O_{6+\delta}$.

214 $La_{1-x} Sr_x CuO_{4+\delta}$.

2212 $Bi_2 Sr_2 Ca_1 Cu_2 O_8$.

2233 $Tl_2 Ca_2 Ba_3 Cu_3 O_{10}$.

Chapter 1

Introduction

One of the principal ingredients in the advancement of today's electronics technology is the exploration of materials which reside at the edge of our present understanding. The so-called high temperature superconductors fit this classification of unusual materials and have attracted considerable attention since early 1987.

The discovery of high temperature (high-T_c) superconductors[1,2,3] has thrown the doors of speculation wide open for anyone who wishes to explain the mechanism which causes the high-T_c transition properties. These high-T_c properties have occurred in a seemingly uncharacteristic material: an oxide insulator with poor electrical conductivity at room temperature. These oxides would have been viewed by many physicists as common rocks less than a decade ago. Many high-T_c cupric oxides have been found in the last few years. A list of a few of the oxide superconductors to date would include $La_{2-x}Sr_xCuO_{4+\delta}$ (214), $YBa_2Cu_3O_{6+\delta}$ (123), $Bi_2Sr_2CaCu_2O_8$ (2212), and $Tl_2Ca_2Ba_3Cu_3O_{10}$ (2233).[4]

The electromagnetic properties of a novel substance provide the foundation for correlating physical properties with the mechanisms which drive them. Spectroscopy is probably the most informative technique available for probing the electronic and magnetic properties of an unfamiliar substance. Spectroscopic techniques are typically divided into three groups: optical, magnetic

resonance, and mass spectroscopy. The optical branch involves all forms of light from microwaves to x-rays. Optical spectroscopy is often used to elucidate the electrical properties of a sample. The magnetic resonance (MR) branch involves such techniques as nuclear magnetic resonance (NMR) , electron spin resonance (ESR), nuclear quadrupole resonance (NQR), *etc*. MR data is used to decipher the bonding properties and the magnetic properties of the substance. Mass spectroscopy is used to determine the structure and chemical composition of an unknown material.

An investigation into the magnetic properties and the mechanism of the high-T_c superconductors must rely in part on a probe of the internal magnetic fields of the material at an atomic scale (*i.e.*, ~ Å). Most of the MR spectroscopy techniques only provide information about the bulk properties of the material. Mössbauer emission spectroscopy (MES), and NMR techniques generally involve substitution of already existing lattice sites with a different probe ion. Other methods, such as electron spin resonance (ESR) can probe the interstitial regions of the lattice; however, they are affected by other magnetic resonance probes (probe-probe interactions) and other band broadening effects such as nuclear quadrupolar interactions. Both NMR and ESR require the application of an external magnetic field in order to detect the behavior induced by the probe. On the other hand, muon spin relaxation (μSR) (pronounced "mu - S - R": *vide infra*) is an internal magnetic ion probe. Further, by using μSR spectroscopy, magnetic fields in the interstitial locations of the material can be measured without the overlapping effects of probe-probe interactions, quadrupole

interactions, and/or electromagnetic effects brought on by the changing the type of probe at the lattice sites or the presence of an externally applied field.

In this thesis, we will only examine the results of μSR on one of the most notorious of the high-T_c superconductors: $YBa_2Cu_3O_{6+\delta}$ (Y123(6+δ)) and its rare-earth doped analogs ($RBa_2Cu_3O_{6+\delta}$: R = rare-earth, and 0.0 $\leq \delta \leq$ 1.0). The experimental work was performed at the Clinton P. Anderson Meson Physics Facility (LAMPF), a part of Los Alamos National Laboratories. The computational work was conducted both at San Jose State University (SJSU), with the muon-spin-probe group ($\mu\sigma\pi$), and at LAMPF as part of a collective effort within the μSR-LAMPF collaboration.

Muon spin relaxation (μSR) employs positive muons (μ^+) to probe the internal magnetic environment in a sample. A detailed explanation on μSR will be presented in chapter two, titled "General Properties of μSR." In oxides such as α-Fe_2O_3,[5-9] and $SrTiO_3$,[10] the μ^+ bonds to the oxygens at temperatures below 150 K forming a muon-oxygen (μO^-) bond similar to a hydroxyl (OH^-) bond. In the chapters that follow, it will be shown that the muon exhibits the same μO^- bonding behavior in the $RBa_2Cu_3O_{6+\delta}$ oxides as seen in other transition metal oxides.[14-17]

Chapter three is an analysis of the search method which was used to find the muon sites. The discussion starts with the development of a semi-emperical potential-energy function which can be used to describe muon-oxygen (μO^-) bonding. The reasoning behind the selection of a μO^- potential is presented. Following this discussion, there is a detailed explanation of the search calculations,

which include potential-energy (PE) calculations, and magnetic-dipole-field (MDF) calculations. In addition, possible improvements to the present computational method are presented.

To make any extensive physical interpretation about the μSR data, the muon's location must be determined. The only way to obtain this information is via a combined study where experimental and computational techniques are used to deduce the whereabouts of the muon in the crystal lattice.

In chapter four, a search for the muon-stop sites is conducted on samples of $RBa_2Cu_3O_y$ {R123y: R = Gd, Ho (y = 7); and R = Er, and Y, (y = 6)}.[14-15] A bulwark of consistent, convincing evidence has been obtained to support the presently established muon-stop sites in all of the $RBa_2Cu_3O_y$ structures. The majority of this work has been completed and published.[14-17]

In chapters five and six, both the μSR data and the location of the μ^+-stop sites (found in chapter four) are used to make interpretations about the magnetism of other R123y structures. After conclusively establishing the regions where the muon localizes, interpretations were made about the magnetic properties of new $RBa_2Cu_3O_y$ samples which came to our attention. The focus of our analytical work was based on the following compounds $PrBa_2Cu_3O_7$, $PrBa_2Cu_3O_6$,[16-17] $PrBa_2(Al_zCu_{1-z})_3O_7$,[17] and $H_xYBa_2Cu_3O_7$.[18-20]

Chapter five, which is titled "Zero-Field μSR on Praseodymium Doped $YBa_2(Al_zCu_{1-z})_3O_{6+\delta}$", is an examination of the magnetism which is found in samples of $(Pr_xY_{1-x})Ba_2Cu_3O_7$, $PrBa_2Cu_3O_6$, and $PrBa_2(Al_zCu_{1-z})_3O_7$.[17,21-23] Generally, magnetic rare-earth doped samples of $RBa_2Cu_3O_y$ (R = Dy, Er, Eu, Ho, Nd, Sm, Tm, or Y) do not

adversely affect the superconducting properties; a curious result in of itself since, in conventional "BCS" superconductors, the presence of any form of magnetism is sufficient to rapidly effect a drop in the superconducting transition temperature (T_c).[24-28] In sharp contrast to the other magnetic rare-earth ions, the Pr *does* depress the T_c very rapidly even in small quantities.

Chapter six, which is titled "Zero-Field μSR on Hydrogen Doped $YBa_2Cu_3O_7$," is an interpretation of the results from zero field μSR measurements on $H_xYBa_2Cu_3O_7$ (0.0 < x < 5.0).[18-20] The hydrogen doped $YBa_2Cu_3O_7$ has been a source of controversy because it has been thought that the hydrogen forms a CuH bond. The formation of CuH bonding is very uncharacteristic of typical transition metal oxides where an OH^- bond is usually observed.

Chapter seven, which is titled "Predictions on the Oxide Superconductors Based Upon μSR Studies of $RBa_2Cu_3O_7$," is a final culmination of postulates and predictions which were made based upon μSR data. There is some experimental evidence to support the predictions made; however, the true power of this thesis will be reflected in its ability to make predictions which extend beyond the limits of the research data presently available. Such is the real art of a scientific investigation.

In the chapters that follow, we will see how μSR has been used to explore one of the most exotic materials of recent years-- $RBa_2Cu_3O_y$. We will see that this spectroscopic method (μSR) offers a remarkable and informative way to explore the internal magnetic properties and/or structures of the cupric oxide materials.

Chapter 2

General Properties of μS R

In this chapter, the experimental set up for muon spin relaxation (μSR) is discussed in detail. The intent of this chapter is to inform the reader how μSR is performed, and how μSR differs from other magnetic resonance probes at the experimental level. Some examples of experimental data are provided to help explain the concepts discussed in the text.

In μSR, positive muons (μ^+) are employed to probe the internal magnetic environment in a sample. The muon is a light particle having $\frac{1}{9}$ the mass of a proton. Because of the smaller mass, the muon can exhibit the same quantum mechanical motions associated with electrons (in effect, a heavy hole) and, at the same time, the muon can exhibit behavior similar to a proton. The regions of localization for the muon is typically the same as the proton in both insulators and in metals. The vibrational frequencies will differ by roughly a factor of three between the H^+ and the μ^+ in the same environments.[29-31]

The muon is an unstable particle which has a mean half-life of 2.2 μs, whereupon it decays into a β^+ particle (positron e^+). The origin of muons is from the decay of positive pions (π^+)

$$\pi^+ \dashrightarrow \mu^+ + \overline{\nu_\mu} \qquad \tau_\pi = 26 \text{ ns}$$

$$\mu^+ \dashrightarrow e^+ + \nu_e + \overline{\nu_\mu} \qquad \tau_\mu = 2.2 \text{ μs}.$$
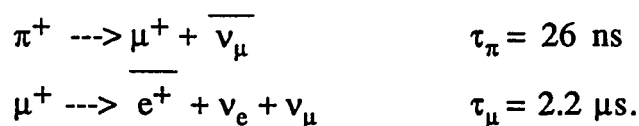
where v_μ refers to a muon-type neutrino, $\overline{v_\mu}$--a muon-type antineutrino, v_e--an electron-type neutrino, τ_π--the half life of the pion, and τ_μ--the half life of the muon.

Muons are useful in magnetic resonance because they exhibit non-conservation of parity--their spin polarization is always right handed (*i.e.*, the positron's linear momentum vector is oppositely directed to the spin angular momentum vector). The linear momentum of the positron which results from a muon decay is always along the spin-axis of the muon (Fig. 2.1). As applied to μSR, the parity violation is useful because the initial spin polarization of the μ^+ is known *before* it enters the sample, and therefore the phase of the positron (decayed muon) is distinguishable if we know the time interval between the time the muon entered the sample and the time of its subsequent decay. If there were no parity violation, then the phase of the muon could be either 0 or π relative to the initial spin polarization, and the muon spectrum would consist of only the exponential decay associated with the half-life of the muon.[29-31]

There are three important parameters which come out of μSR, the asymmetry (A_s), the muon spin relaxation function G(t), and the frequency (f). If the muon localizes in the sample, we can deduce the magnitude of the local magnetic field (B_{loc}), because the frequency (f) is proportional to B_{loc}. When we know the region where muon bonding occurs, then A_s and G(t) can be used to make physical interpretations about the magnetic field distribution (ΔB_{loc}) in the region(s) where the μ^+ localizes. As a result, B_{loc}, A_s, and G(t) can help us deduce the magnetic structure--if the sample is an insulator, or the vortex structure--if the sample is a type II superconductor.
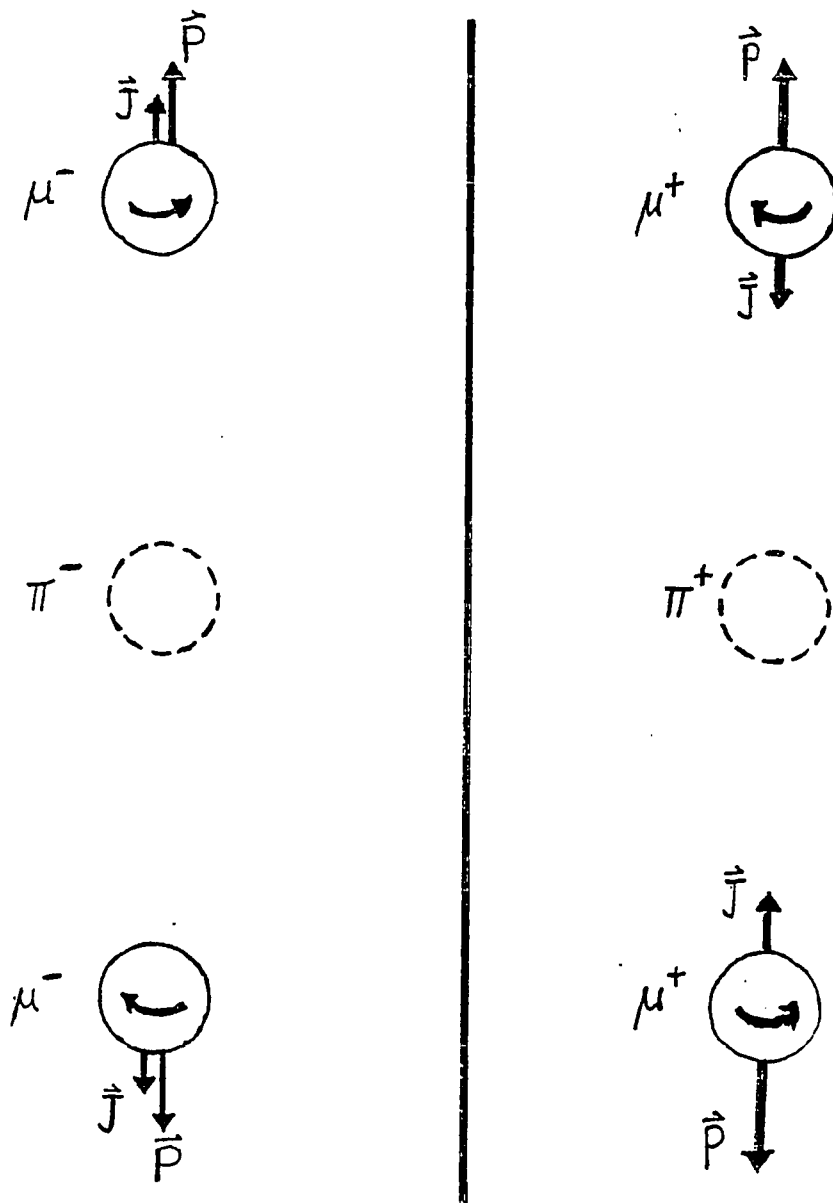
Figure 2.1. Illustration of parity violation for the pion decay into muons. Both the positive and the negative pions are depicted to show the symmetry relationship between the two types of decay. Only one possibility is allowed, for a given pion decay event. The momentum conservation is the result of the formation of a neutrino which moves in the opposite direction of the muon. Note that the spin polarization for the μ^+ (J) is opposite to the linear momentum (P) of the μ^+.

A time histogram is generated by detecting the resulting positrons on the β^+ particle counters with photo-multipliers. Usually a quartet of positron detectors are set up in a plane perpendicular to the muon polarization (Fig. 2.2). If an external magnetic field is applied to the sample, then the field is generally applied perpendicular to the muon polarization and perpendicular to the quartet of detectors (Fig. 2.2), a technique referred to as transverse field.

A meaningful muon time histogram requires a careful experimental setup. First, a source of spin polarized muons is needed. The most useful source of muons is a nuclear science facility where large numbers of muons can be generated with roughly 90% or better spin polarization depending on the meson physics facility. Cosmic muons is another source--they exhibit 1% spin polarization. Second, the entry of a single muon into your sample region must be recorded. Third, the possibility that a stray muon follows close behind the first one must be eliminated. Finally, the possibility that some muon, which is already in the sample, decays after a second muon has entered the sample must be avoided. The time domain necessary to generate an acceptable muon decay event is about 10 μs during which time only one muon is allowed to enter the sample and only one muon decay event is allowed. If any of the above rules is violated, the recorded information must be rejected.

The M counter (Fig. 2.2) detects the muon entering the sample whereupon it starts up a clock which also records any signals from the positron detectors during the 10 μs interval. One set of counters $(F_1, B_1, U_1,$ and $L_1)$ is within the cryostate and two sets are outside
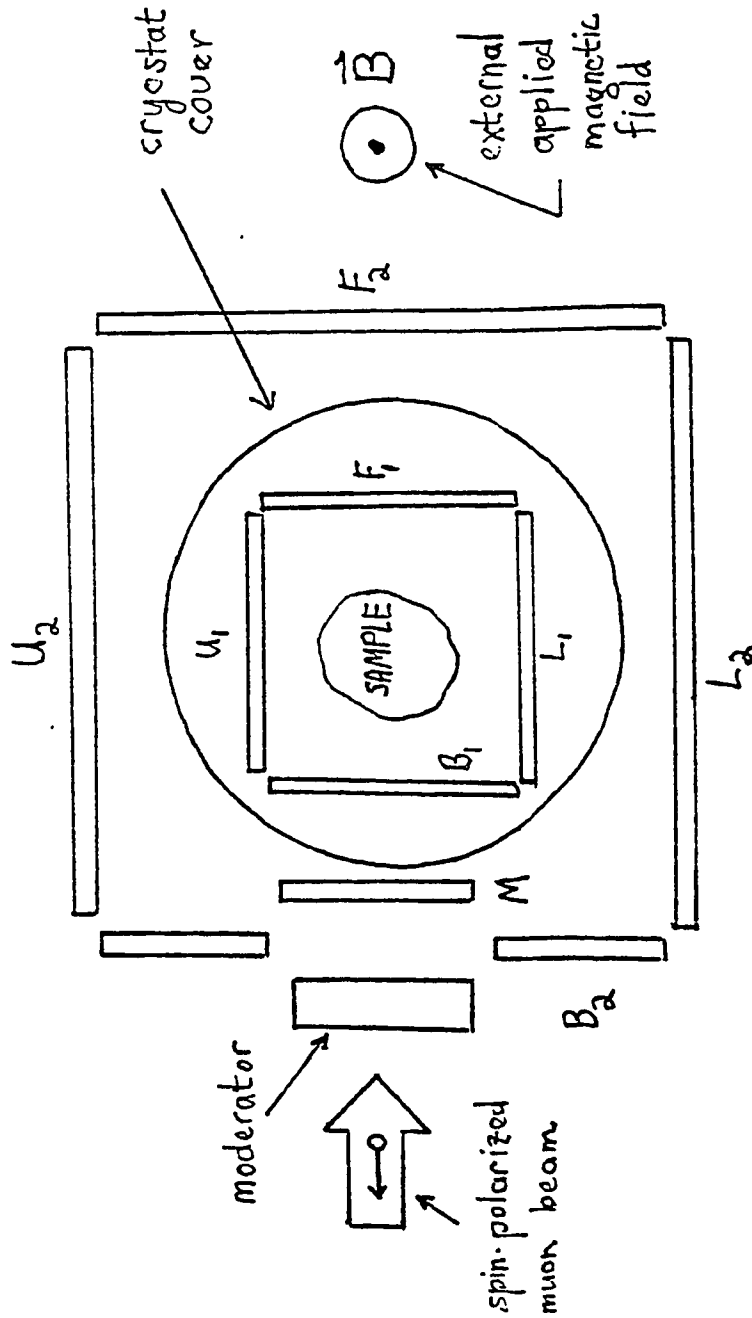
Figure 2.2. Diagram of the μSR experimental set up. The view is looking down on top of the cryostate. The objects labeled U_1, U_2 etc. are the counters. The number one counters are located inside of the cryostate. Therefore, muons decay events which occur on the number one counters are the result of events which occur within the sample. The purpose of the various counters are discussed in the text. For more specific details, see reference (29-31).

CⅢD》ᴎ

PERP   4619.115   PR.SBCO   H# 2   10K   1000T
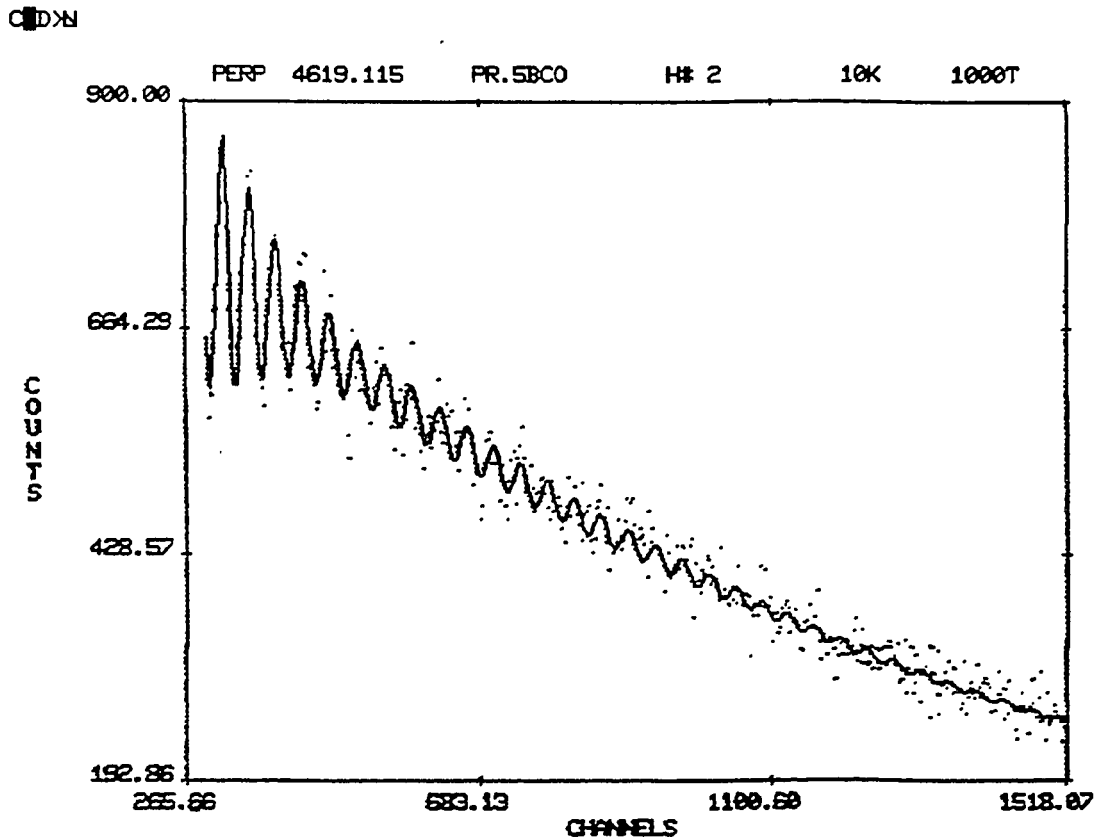
Figure 2.3. The time histogram of muon decay events in a sample of $(Pr_{0.5}Y_{0.5})Ba_2Cu_3O_7$ (¡superconductor!) measured using µSR in a 1 kOe transverse applied field at 10 K. The zero-field data has a similar appearance; however, the amplitude of the oscillations is significantly reduced. The line represents a fit of the data using the equation provided in the text.

$(F_2, B_2, U_2,$ and $L_2;$ $F_3, B_3, U_3,$ and $L_3).$ (The third counters are not shown in the figure.) When the muon decays, the direction of the positron's linear momentum is parallel to the angular momentum vector of the precessing muon. The decay event is registered on one of the four pair of detectors: front (F), back (B), lower (L), or upper (U). The decay event must register on only one of the four sets of detectors, for example the $F_1,$ $F_2,$ and F_3 counters. If the event appears on any one of the other sets within the 10 μs time interval, the event must be deleted from the data. In this way, a muon spectrum is generated.

Since the error of these statistics decreases as $\frac{1}{\sqrt{N}}$, a sufficiently detailed muon spectrum can be generated with more than 300,000 counts on an individual pair of counters (e.g., F_1 and F_2) when no external field is applied (zero field--see Fig. 2.3).

The muons from an accelerator are generated at random time intervals. A large number of the muon decay events are deleted because they fail to satisfy all of the above mentioned requirements.

For NMR, an external field must be applied to the sample in order to detect the resonant frequency of the magnetic nuclei.[35-36] For μSR, it is possible to apply an external field to see muon resonance and it is also possible to inject the muon with no applied field (zero field). Under either experimental condition, the resulting time histogram looks identical to the free induction decay of NMR (Fig. 2.3) but the signal from the μSR spectrum has the exponential decay due to the muon life time. When the exponential decay is removed, the interpretation of signals seen in μSR (in transverse

field) and NMR are identical (Fig. 2.4). Parameters such as transverse relaxation (T_2), longitudinal relaxation (T_1), and asymmetry (A_S) can readily be interpreted in the same way for both means of spectroscopy. The free induction decay spectrum is converted to a frequency spectrum via the discrete Fourier transform method. The resulting spectrum has the appearance of a typical magnetic resonance spectrum (Fig. 2.5).[35-36]

If the magnetic moment on the muon is precessing due to the presence of a local magnetic field, then the frequency of the precessing muon can be recorded in the form of a time histogram which can be described by the following equation

$$N(t) = N_0 e^{-t/\tau_\mu}\left[1+\sum_{i=1}^{n}\left(G^{(i)}A_S^{(i)}\cos(2\pi f^{(i)}+\phi^{(i)})\right)\right] + B.G.$$

where n (above the Σ) is the number of sites where the muon stops, N_0 is the total number of muons decay events starting at t = 0--the time the muon enters the sample, $G^{(i)}(t)$ is the relaxation function of the muon at the ith site, $A_S^{(i)}$--the asymmetry , $f^{(i)}$--the frequency, and $\phi^{(i)}$--the phase, and B.G.--the background decay events.[29-34]

One of the unique contributions that μSR makes is in its ability to probe the internal magnetic fields of the sample without the application of an externally applied field. Therefore, a magnetic material can be probed without any external manipulation of the internal environment (as happens when an external field is applied). Furthermore, the hyperfine structure generated by other probe ions
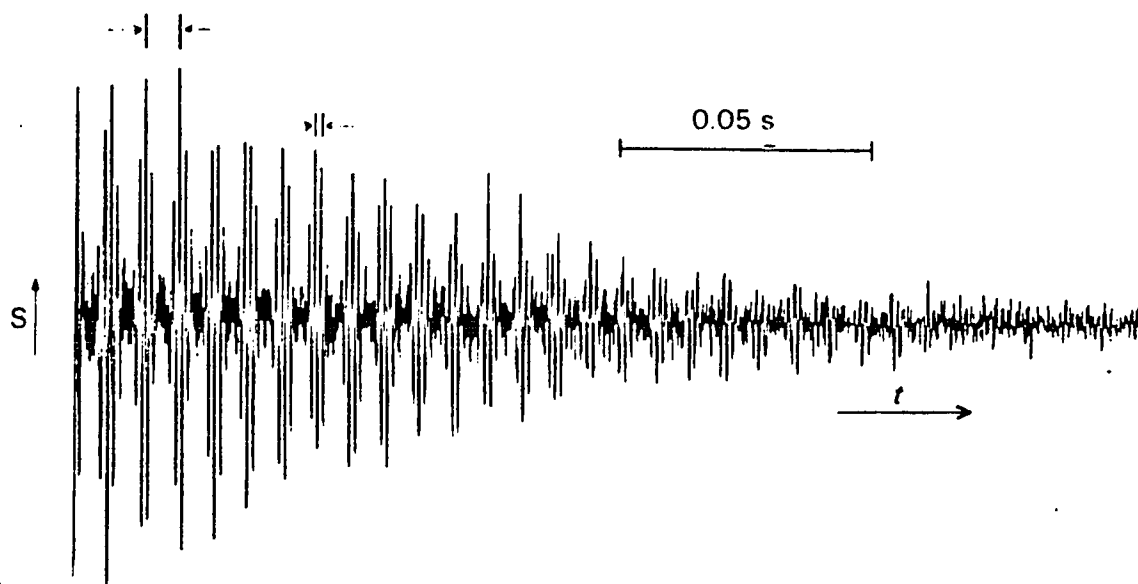
Figure 2.4. The free induction decay for a ^{13}C NMR spectrum of methyl iodide (CH$_3$I). The major difference between the μSR spectrum and this NMR spectrum is that the signal from the muons decays over time. The modulation in the signal is the result of the carrier frequency (25 MHz in this case) and the resonant frequency of the ^{13}C in the CH$_3$I. Taken from Robin K. Harris. Nuclaer Magnetic Resonance Spectroscopy, A Physiochemical View (Longman Scientific & Technical: Burnt Hill, Harlow, Essex, 1986). (Reference 36.)
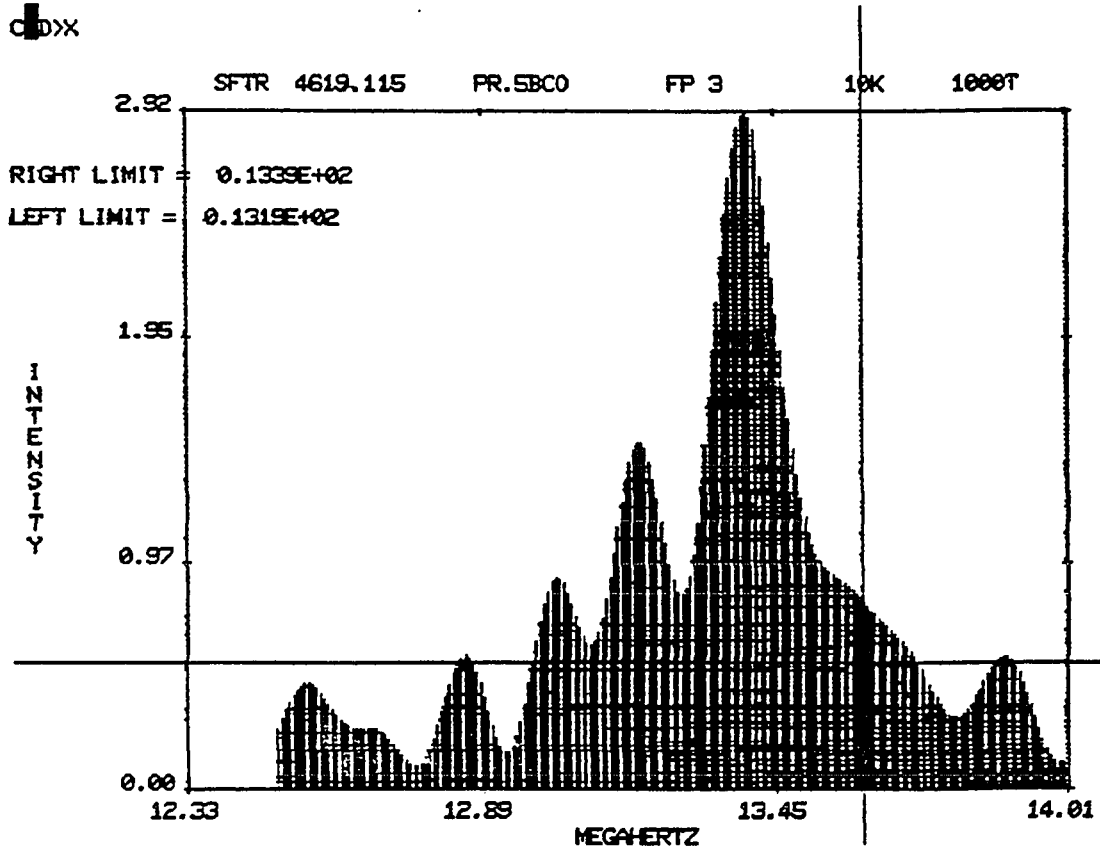
Figure 2.5. The Fourier transform of the μSR data in Figure 2.3. The frequency at 13.4 MHz is due to the applied field (1 kOe transverse field) in the normal regions of the sample, and the frequency at about 13.2 MHz is the result of the field in the superconducting regions of the sample.

is minimized because only one probe is allowed to enter at a given time interval. Thus, complicated hyperfine structures due to the presence of numerous over lapping probe spins (the *nuclear - Overhauser -enhancement* effect) is eliminated; only the peaks corresponding to specific magnetic environments remain.

When an external magnetic field is applied to a sample during μSR spectroscopy, each histogram (*e.g.*, F) requires more than 250,000 good events to generate a usable spectrum. When the muons are injected into a sample in zero field, a single useful histogram requires a minimum of 750,000 counts to generate a spectrum in which f, G(t), and A_s can be successfully determined. At LAMPF, spectrums such as these generally take quite a long time to acquire, given the random distribution of muons generated in the accelerator beam during any given time interval. As it turns out, the μSR done at LAMPF has been done with an interest toward minimizing the time it takes to get a good spectrum but with an eye toward maximizing the good data obtained. Typical sampling times for a given spectrum can sometimes require two hours to complete, especially in zero field μSR. A run such as this corresponds to approximately 1.5 M counts.

To understand the data we get on the local magnetic fields of $RBa_2Cu_3O_{6+\delta}$ crystals (both the superconducting and non-superconducting structures), we must first determine where the muons will most probably localize. In the chapters that follow, we will show how the μ^+-stop sites were found in $RBa_2Cu_3O_{6+\delta}$. Then, once the μ^+ location had been conclusively verified, μSR was used to

make interpretations about the magnetic environment surrounding the muon in a variety of different R123y structures.

Chapter 3

Search Calculations For Muon Sites in $RBa_2Cu_3O_y$

3.1. Introduction

In this chapter, we examine the development of a potential energy function, and the search method used in finding the muon-stop sites.

In every scientific investigation, assumptions are made which determine the type of results which are found. In this chapter, and the chapters that follow, the critical assumptions that supports this work is that the $RBa_2Cu_3O_{6+\delta}$ structures exhibit muon behavior which is typical of the majority of transition metal oxides already studied.[5-13] What follows from this premise is (1) that muon-oxygen bonding (μO^-) will be observed, and (2) that the μO^- bond location and orientation can be found using a combination of zero-field μSR, magnetic-dipole-field (MDF) calculations, and potential-energy (PE) calculations.

Starting from the above foundations, three essential steps should be considered in order to obtain reasonable results. First, a potential energy function must be developed which describes μO^- bonding accurately to first order. Second, a computational search method must be developed to find possible muon sites in the material. Preferably, the search should use more than one independent method to find the muon sites. Finally, a sample of material must be found which will yield useful μSR data and also have internal magnetic fields which are propitious to MDF calculations.

The location of the candidate sites are obtained from PE calculations using functions which describe the μO^- potential. The functions are typically semi-empirical approximations of covalent bonding between two atoms. The proposed sites are located by mapping the PE surfaces of the interstitial regions of the crystal, and their existence is verified using the μSR frequency data, and MDF calculations. The MDF calculations are a definitive test of any theory on muon bonding because the observed μSR signal at a particular site *must* be close to the same value as the magnitude of the magnetic field which is predicted by the MDF calculations at the specified muon site.

Muon bonding is strongly dependent on the density of the conduction electrons. For example, in metals such as Fe, muon localization at particular sites is not observed because the muons diffuse through the lattice via quantum tunneling.[37] On the other hand, in typical insulating transition-metal oxides, at temperatures below 150 K, the muon localizes at approximately 1 Å from the oxygen atoms forming a muon-oxygen bond (μO^-), analogous to the hydroxyl bond (OH^-). Typical oxides which show this behavior are Fe_3O_4,[5-8] $FeTiO_3$, α-Fe_2O_3, Cr_2O_3,[9,11,12,13] and $SrTiO_3$.[10]

Muon localization is verified using zero field (ZF) measurements and a fit of the precession frequency, the relaxation rate, and the asymmetry. If the material is a metal, then the relaxation rates will have an exponential character because of the diffusion of the muon through the metal. Furthermore, there is no fixed frequency because of the random orientation of the local field, and there is a small asymmetry because of the large fraction of μ^+ which are lost to

electron capture (forming muonium) and the subsequent loss of spin polarization.[29-31] If the oxide possesses long-range magnetic ordering due to a magnetic ion (such as Fe in Fe_3O_4), then fixed frequency signals in the muon spectrum will be seen.[32-34] For oxides with long-range magnetic ordering the relaxation functions are typically Gaussian in character, whereas oxides with random magnetic ordering will commonly exhibit exponential square root relaxation functions (spin glasses--zero frequency signal). We expect, and have observed, similar μ^+ behavior for the $RBa_2Cu_3O_y$ oxides.[29-34] The asymmetry provides an indication of the percentage of muons that are stopping at the particular μ^+-stop site. If all of the spin polarized muons were to occupy the same site, then theoretically, the asymmetry should be $\frac{1}{3}$ as a consequence of the experimental geometry.

To find the muon sites we need to be able to compare the MDF calculations with μSR data from samples of $RBa_2Cu_3O_{6+\delta}$ which are known to have highly localized magnetic moments that order in a periodic fashion (*e.g.*, ferromagnetic ordering). If the magnetic ordering consists of ions with highly localized moments, then the internal magnetic fields are easily calculated using classical magnetic-dipole calculations. The covalent ordering mechanisms which appear in such materials as iron[37] are not well approximated by point dipoles because the electron spins are highly delocalized and therefore shared by many atoms simultaneously). Such complex systems require techniques from quantum mechanics which demand extensive computational power and often do not predict the correct the ground state energy of the magnetic or superconducting material.

A example of such an technique is "unrestricted Hartree Fock self consistent field" (UHF-SCF) cluster calculations.[38] In addition, the results often are strongly dependent upon the assumptions that are made about the magnetic model.[38]

A common method used to introduce localized dipolar ordering in a sample consists of replacing a non-magnetic rare-earth ion (such as Y), with a magnetic (4f electrons) rare-earth ion (such as Gd, Er, Dy *etc.*). The resulting magnetically ordered structure produces large local magnetic fields which are easily measured by the muon probe, which has a large gyromagnetic ratio (135.5 MHz/T, *c.f.* the gyromagnetic ratio of hydrogen--42.6 MHz/T).

From previous work, it has been found that the magnetic dipole fields in transition metal oxides are an order of magnitude larger than any covalent fields such as the supertransfer fields.[32-34] Therefore, the magnetic signal from the rare-earth ions can be readily approximated using MDF calculations. Such calculations are used as an independent method for comparing the experimental μSR data (*i.e.*, B_{loc}) with the approximate locations of the candidate sites found by PE calculations.

3.2. Development of the Muon-Oxygen Bonding Potential

We examined several possible muon-oxygen bonding potential energy functions to find the approximate location of the muon sites in R123y.[39] It was important to find the strengths and weaknesses of all of these functions when they were used in potential energy calculations. In these comparisons, we present the three standard types of potentials that we found in the literature: the Rodriguez/Rüegg potential,[40] the Morse potential,[41] and the Lippincott potential.[42-44]

To start this section, we define the terms from chemistry and physics which are going to be used. From the onset of this discussion, three significant figures will be assumed for all of the computations presented. First, r_0 corresponds to the equilibrium bond distance (Å) between the μ^+ and the O^{2-} where the potential energy becomes a minimum. Second, R indicates the distance at which the μO^- bond will become unstable, i.e. where $\dfrac{\partial^2 V_R(r)}{\partial r^2}\Big|_{r=R} = 0$.

Third, k_{eff} is the effective spring constant for the μO^- bond, i.e. $k_{eff} = \dfrac{\partial^2 V_R(r)}{\partial r^2}\Big|_{r=r_0}$. Fourth, to describe the oscillation frequency of the μO^- bond, the reduced mass of the muon must be used (m_μ). The reduced mass is defined as follows

$$m_{12} = (m_1^*)(m_2^*) \,/\, (m_1^* + m_2^*) \ \times (1.66 \times 10^{-27} \ kg),$$

where m_1^* is the atomic mass of atom number 1 (in atomic mass units--amu), m_2^* is the atomic mass (amu) of atom 2, and 1.66×10^{-27} kg is the mass of a proton in kilograms. For the muon, the reduced mass ($m_{\mu O}$) becomes

$$m_{\mu O} = (.110) \times (1.66 \times 10^{-27}) = 1.83 \times 10^{-28} \text{ kg,}$$

where $m_1^* = m_\mu^* = .111$ amu and $m_2^* = m_O^* = 16.0$ amu. Fifth, the spectroscopic properties of the muon bond must be examined so that physical comparisons can be made. The oscillation frequency of the μO^- bond will be expressed in both Hertz (f_o), where

$$f_o = \frac{1}{2\pi} \omega_o = \frac{1}{2\pi} \sqrt{\frac{k_{eff}}{m_{\mu O}}},$$

and also in wave numbers ($k_{wave}^{\mu O}$), where

$$k_{wave}^{\mu O} = f_o/c.$$

Wave numbers (cm^{-1}) are typically used to describe IR spectra. Finally, to compare the muon bond to a more familiar bond (OH^-), the wave numbers of $k_{wave}^{\mu O}$ will be compared with the wave numbers for the OH^- bond (k_{wave}^{HO}). The reduce mass for the hydrogen bond (m_{HO}) will be

$$m_{HO} = .941 \times (1.66 \times 10^{-27} \text{ kg}) = 1.56 \times 10^{-27} \text{ kg}.$$

where $m_H^* = 1.00$ amu, and $m_O^* = 16.0$ amu.

The following equations are obtained for the Rodriguez/Rüegg potential[40]

$$V_R(r) = \beta \left\{ -\frac{1}{r} + \frac{1}{\gamma r_0}\left(\frac{r_0}{r}\right)^{\gamma} \right\}$$

$$k_{eff} = \frac{\partial^2 V_R(r)}{\partial r^2}\Big|_{r=r_0} = \frac{\beta}{r_0^3}(\gamma - 1)$$

$$R = \sqrt[\gamma-1]{\frac{1}{2}(\gamma+1)}\ r_0$$

where r_0, R, and k_{eff} are defined above, and γ is a dimensionless semi-empirical constant associated with R. The constant β is the Coulombic constant

$$\beta = \frac{|e|^2}{4\pi\epsilon_0}\alpha = 14.4 \text{ eVÅ } \alpha \quad (\text{where } \alpha = \frac{|q_O||q_\mu|}{\epsilon_r}),$$

where 14.4 eVÅ is the Coulomb constant for a unit electron charge ($|e| = 1.6 \times 10^{-19}$ C, $k|e|^2 = 14.4$ eVÅ), and q_μ and $|q_O|$ are the effective formal charges (dimensionless) for the muon and the oxygen respectively. (Typically, $q_\mu \sim 1$, and $|q_O| \sim |-2|$.)

The following equations describe the Morse potential,[41]

$$V_M(r) = D_o(1 - e^{-\alpha(r-r_o)})^2 - D_o$$

$$k_{eff} = \frac{\partial^2 V_M(r)}{\partial r^2} \Big|_{r=r_0} = 2D_o\alpha^2$$

$$R = r_o + \frac{1}{\alpha} \ln(2) \ , \ \text{or} \quad \left(\quad \alpha = \frac{\ln(2)}{R - r_o} \quad \right)$$

where r_o, R, and k_{eff} have the same meaning as above, and α ($\mathring{A}^{-1}$) is associated with the strength of the muon-oxygen bond.

For the Lippincott potential,[42-44] we obtain the following

$$V_L(r) = D_o\left(1 - \exp\left[\frac{-\eta(r-r_o)^2}{2r} \right] \right)$$

$$k_{eff} = \frac{\partial^2 V_L(r)}{\partial r^2} \Big|_{r=r_0} = D_o\frac{\eta}{r_o}$$

$$\left(\quad \eta = \frac{4r_o^2\ R}{(R^2 - r_o^2)^2} \quad \right)$$

where η ($\mathring{A}^{-1}$), like α in the Morse potential, is associated with the strength of the muon-oxygen bond.

To compare these three potentials, we began by examining the classical effective spring constant and the resulting oscillation frequency of the bond. In order to make the results comparable, R was fixed at the same value for all of the potentials V_R, V_M, and V_L.

The comparisons of spectroscopic properties for the muon are based upon the initial parameters (r_0, R) selected for one of the potentials.

In this comparison, we selected the following semi-empirical constants for the Rodriguez/Rüegg potential: ϵ_r = 5.57, q_O = -2.00, and q_μ = +1.00. These constants are associated with the hopping times of the muon in Fe_3O_4 as postulated by Rüegg,[40]

$$\beta = \frac{|e|^2}{4\pi\epsilon_0} \frac{q_\mu |q_O|}{\epsilon_r} = 14.4 \text{ eV\AA} \frac{(1)|(-2)|}{5.57} = 8.27 \times 10^{-29} \text{ Nm}^2$$

we find for the following initial values (r_0 = 1.05 Å, and γ = 8.32)

$$k_{eff} = \frac{\alpha}{r_0^3}(\gamma-1) = 523. \frac{N}{m}$$

and, using

$$f_0 = \frac{1}{2\pi}\sqrt{\frac{k_{eff}}{m_{\mu O}}}$$

where m_μ is the reduced mass (kg) corresponding to the μO^- bond,

$$f_0 = \frac{1}{2\pi}\sqrt{\frac{523. \frac{N}{m}}{1.83 \times 10^{-28} \text{ kg}}} = 2.69 \times 10^{+14} \text{ Hz}.$$

From the equations generated above, R = 1.30 Å.

In standard IR spectroscopy, where we define $k_{wave}^{\mu O} = f_0/c$, we find that $k_{wave}^{\mu O}$ = 8970 cm^{-1}. If the bond were an OH^- bond, then the

resulting vibrational frequency in wave numbers becomes $k_{wave}^{HO} =$

3070 cm^{-1}, which is lower than typical values for OH$^-$ bonds in other substances (3600 cm^{-1}).

The same parameters (r_0 = 1.05 Å, and R = 1.30 Å) were applied to the Morse potential along with the value of the equilibrium bond value D_0 = 3.48 eV = 5.57 x 10^{-19} J (a value established for OH$^-$ bonding[45-47]). From these initial values, the resulting equations are

$$k_{eff} = 2D_0\alpha^2 = 856. \frac{N}{m} \quad (\text{ where } \alpha = \frac{\ln(2)}{R - r_0}) ,$$

$$f_0 = \frac{1}{2\pi} \sqrt{\frac{856. \frac{N}{m}}{1.83 \times 10^{-28} \text{ kg}}} = 3.44 \times 10^{+14} \text{ Hz}.$$

For the μO$^-$, $k_{wave}^{\mu O}$ = 11,500 cm^{-1}, and for the OH$^-$ bond, k_{wave}^{HO} = 3,930 cm^{-1} (higher than 3600 cm^{-1}).

The same parameters as the Morse potential (r_0 = 1.05 Å, R = 1.30 Å, and D_0 = 5.57 x 10^{-19} J) were applied to the Lippincott potential. From these initial values, the obtained equations are

$$k_{eff} = D_0 \frac{n}{r_0} = 881. \frac{N}{m}$$

$$f_0 = \frac{1}{2\pi} \sqrt{\frac{881. \frac{N}{m}}{1.83 \times 10^{-28} \text{ kg}}} = 3.49 \times 10^{+14} \text{ Hz}.$$

For the μO^-, $k_{wave}^{\mu O}$ = 11,600 cm^{-1}. For the OH$^-$, k_{wave}^{HO} = 3,990 cm^{-1}.

All three potentials yield oscillation frequencies (f_o) that are either on one side or the other of the nominal value for an OH$^-$ bond, and all are of the same order of magnitude. Furthermore, k_{wave}^{HO} is within the possible range of values typical for OH$^-$ bonds. Therefore, based upon oscillation frequency alone, any one of these three potentials could be invoked to approximate the Hamiltonian in the case of small perturbations.

A potential energy function must satisfy four basic criteria, if the function is to be used as an approximation of the actual potential in the Hamiltonian operator.[41] First, the function must approach some finite value when r becomes large. Second, function should yield only one expectation value (r_o= $<r>$) for the equilibrium distance between the muon and the oxygen. Third, the potential energy must approach an extremely large value as r approaches zero, so that the probability of finding two particles occupying the same point is zero (the Pauli exclusion principle). Lastly, the potential energy function must yield the quantum vibrational energy levels of the μO^- bond which can be expressed in terms of an anharmonic oscillator

$$E(n) = -D_o + k_1(n + \tfrac{1}{2}) + k_2(n + \tfrac{1}{2})^2 + k_3(n + \tfrac{1}{2})^3 \ . \ \ . \ \ . \ \ .$$

where D_o is the same constant that is used in the Morse potential, n is the principal quantum number of the harmonic oscillator equation, k_1 is the energy of the harmonic oscillator solution (k_1 = $\hbar\omega_o$), and k_2,

k_3, *etc.* are higher order terms which express the anharmonic part of the solution of the particular potential energy function.

3.2.1. The Lippincott Potential (V_L)

The Lippincott potential[42-44] only passes the first and second conditions above. V_L fails the third condition because V_L settles to a finite value at r=0. This is not useful in describing the type of bonding we are studying in this problem. For the application at hand, this potential does not appear to generate any significant improvement in the muon bond approximation and is not useful in describing the repulsion of the muon when at distances closer than r_o.

3.2.2. The Morse Potential (V_M)

To a first approximation, the Morse potential (MP)[41] satisfies all four of these conditions stated above. However, upon close examination, we must consider some crucial assumptions. First, the potential applies only to diatomic molecule in an isolated system. In an isolated system the most probable energy states will be those for which n (the principal quantum number) is small. Therefore, the separation between the two atoms deviates little from $<r>$. Furthermore, in an isolated system, even if one chooses $r >> <r>$ as an initial condition, the two atoms will eventually return to their

equilibrium position $<r>$ simply because there are no other competing forces present.

Therefore, whereas the MP may be a valid approximation for small perturbations about $<r>$, it is not accurate for large R and must be modified significantly to be incorporated into the context of a crystalline environment. One of the simplest modifications which can be made to better depict a crystalline environment is to incorporate a long range "Coulombic tail" in the total potential. The Coulombic tail takes into account the long range Coulombic attraction between the muon and the oxygen.

3.2.3. Rodriguez/Rüegg Potential (V_R)

The first three conditions are easily satisfied using the Rodriguez/Rüegg potential (RRP).[40] Furthermore, V_R satisfies the third condition even better than V_M. The vibrational energy levels are not well satisfied in this approximation because at small equilibrium bond distances ($r \approx r_0$), the MP is known to provide an acceptable approximation of the vibrational modes and the results of the RRP are not particularly close to the MP values for a given choice of r_0, and R. However, early attempts to use RRP to locate the muon sites in Fe_2O_3 were very successful despite the somewhat questionable nature of the potential.

A desirable compromise between utilizing a continuous potential like the RRP (which is easy to calculate), and the MP (which is not accurate for large bond separations), is to employ the MP with a "Coulombic tail" (MPw/CT) when the bond distances exceeds some

specified distance.[48]   So far as computation is concerned, the RRP is much simpler to use than the MPw/CT function.   Therefore, for the purpose of simplicity and because of the previous success of RRP for Fe_2O_3, we chose to start with the RRP in our initial calculations.   At a later time we compared these results with other calculations utilizing the MPw/CT function in the application of the Ewald method.

3.3.   Calculation of Muon Potential Energy in Crystals

The search method employs two essentially independent means to deduce the muon's whereabouts--potential energy calculations and magnetic dipole field calculations.[5-13,32-34]   The two methods exhibit independence because the electronic structure of the sample is only minutely affected by the magnetic effects.   Although any potential energy model utilizing electron density functions $(\rho(r)=|\Psi(r)|^2)$, such as the Kohn-Shams Density-Functional-Formalism,[38] must ultimately be able to express the magnetic fields (or superconducting properties) of the electronic structure, the resulting magnetic (or superconducting) contributions are often calculated as small correction terms to the overall value of $\rho(r)$ and do not significantly affect the μ^+ localization.   The use of MDF calculations and PE calculations places a greater significance on the proposed sites since the likelihood of both methods yielding agreement with experimental data is very small unless the selected site is valid.

The potential energy calculations were performed on $RBa_2Cu_3O_{6+\delta}$ (δ = 0.0, 0.5, and 1.0) using a screened Coulombic potential.

We began with the assumption that these $RBa_2Cu_3O_y$ (R123y) structures behaved like typical oxides in which the muon bonds to the oxygen, so a Morse-like potential (the RRP--V_R *vide supra*) was employed to describe the potential of the μO^- bond,

$$V(r_{\mu j}) = \beta\left\{-\frac{1}{r_{\mu j}} + \frac{1}{\gamma r_0}\left(\frac{r_0}{r_{\mu j}}\right)^\gamma\right\},$$

in which

$$V(r_\mu) = \sum_{j=1}^{\infty} V(r_{\mu j}),$$

where r_μ is the location of the muon in the R123y lattice, $r_{\mu j}$ is the distance of the muon from the jth oxygen in Å, V is the potential in eV, and β, γ, and r_0 are semi-empirical constants (β = 5.17 eVÅ, γ = 8.32, and r_0 = 1.05 Å).

Metallic oxides generally exhibit an ionic character in their bonding. Therefore, the muon-cation interaction is expressed by screened Coulombic potentials. The following cation valencies were used in the calculations: R^{3+}, Ba^{2+}, $Cu^{2.5+}$ in the CuO-plane layers and Cu^{2+} in the CuO-chain layers.

For calculation of the PE in R123y, the relative dielectric constant was set at 5.6, a typical value for a transition metal oxide material.[49] A typical value of the dielectric constant in CuO is about ϵ = $10\epsilon_0$. Regardless of the actual value of ϵ in R123y, because we

Variation of PE at (.5,.0,.0)

radius of calculation (Å)
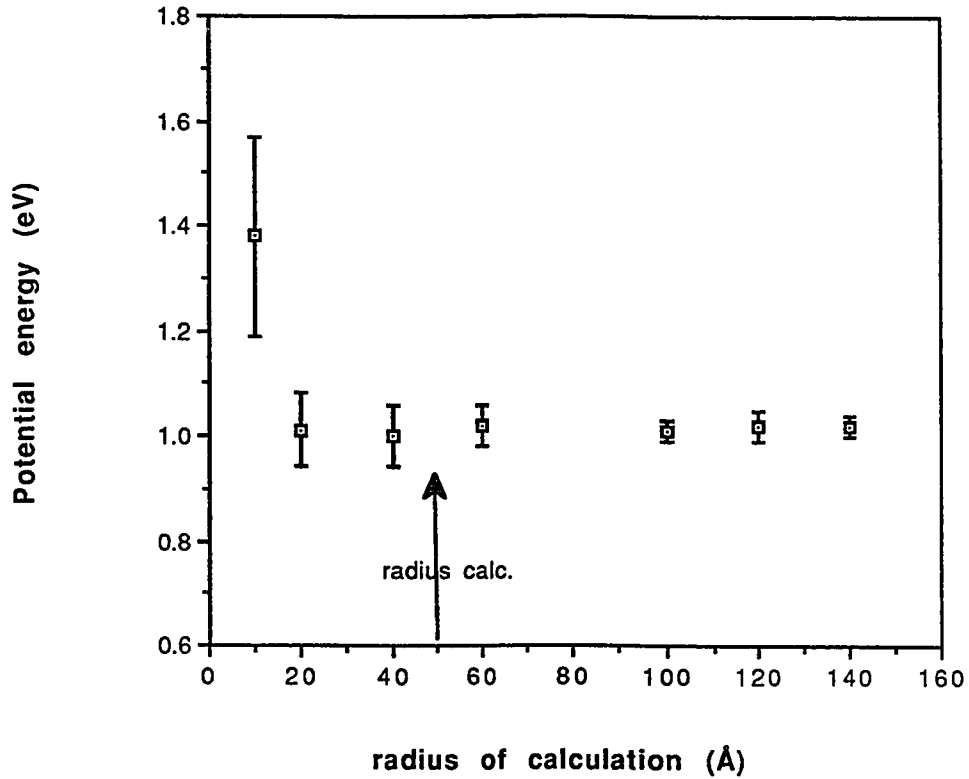
Figure 3.1. Variations in the potential energy (eV) at the the location $r_{\mu k}$ = (x/a, y/b, z/c) = (.5, .0, .0) as a function of the radius of calculation ($R_{calc.}$). The data shows that the potential reaches a stable value at a 40 Å radius of calculation ($R_{calc.}$).

The error bars are based upon the standard deviation for a set of lattice locations ($r_{\mu k}$). Averages for the potential at 40, 60, 100, 120, and 140 Å (R_{calc}^j) are calculated for each lattice site, producing

$$V(r_{\mu k}) = \sum_{j=1}^{all\ j} V(r_{\mu k}, R_{calc}^j) ,$$

The deviation of the site ($r_{\mu k}$), using a particular radius (R_{calc}^j), from the average ($V(r_{\mu k})$) is calculated ($\Delta V(r_{\mu k}, R_{calc}^j)$). The error bars in the picture are the calculated standard deviation of the values ($\Delta V(r_{\mu k})$) for all of the lattice sites ($r_{\mu k}$ at fixed R_{calc}^j). The set of $r_{\mu k}$ which was used is finite; therefore, the standard deviations are only an estimate.

are using a classical PE computation (RRP), the difference in dielectric constant will only affect the magnitude of the final potential (V_R) and not the location of the muon sites themselves.

The Coulombic potentials were calculated within a finite sphere of 50 Å. The series has been found to converge whenever the net charge in each unit cell is set to zero and only those unit cells which lie within a sphere of radius R are considered in the summation. The latter method ensures that the lattice summations vary by less than 0.1 eV between different choices of R. The lattice summation already shows stability within the range of 0.1 eV for R ≥ 36 Å (approximately 9 perovskite unit cells). In Figure 3.1, the deviation between successively larger radii are examined out to a 140 Å spherical shell. The fluctuations rapidly settle to a specific value for a radius greater than 40 Å. Establishing a net charge of zero within the unit cell minimizes the number of unit cells that must be included to produce a limiting value on the potential. It should be noted that lattice summations that converge at a rate of $\frac{1}{R}$ generally require far more that 36 Å in order to yield a stable limiting value. However, by creating a net zero charge in the lattice, each unit cell behaves like an electric dipole (because of the balance of positive and negative charges). Therefore, when the calculations are handled in this way, the summation will actually converge at the rate of $\frac{1}{R^2}$ instead of $\frac{1}{R}$.

The results of these calculations are only approximate using the potentials above, because known effects of oxygen polarization[45-46] (or possible oxidation due to O^{1-}) and lattice relaxation[45-46,50-53] have not been taken into account. However, as known from earlier search calculations in other oxides, the results are indicative, and

quite informative, when combined with magnetic-dipole-field calculations, which are described below.

In addition to the search for potential-energy minima using mapping, we also employed a simple Monte Carlo method mimicking the muon implantation and thermalization process. For a random location in the unit cell, the potential energy is calculated and compared to that of a randomly generated point at a search distance of 0.1 Å (this distance is about equal to the amplitude for zero-point vibration of a muon localized in a μ-O bond[11-13,57]). In most cases a lower energy is found; then for this lower-energy point a random point at 0.1 Å was generated, for which the energy is calculated and compared, and this procedure is iterated. In case no lower energy is found, the "search radius" is reduced by a factor of 0.5 and a new random direction is attempted. Running averages and standard deviations of the muon coordinates and energy are kept. When the calculations converge (*i.e.*, a minimum is found) the standard deviations provide a measure of the errors. This method is not particularly fast in finding energy minima, but can give useful information about the statistical distribution of the candidate muon-stop sites.

3.4. Ewald Potential Energy Calculations

In more recent work, these same calculations were performed using the Ewald method to gain faster convergence of the ionic potentials.[58-63] In the Ewald summation, the Morse potential was employed for oxygens which were close to the muon. The resulting

equation is the Morse potential with a Coulombic Tail (MPw/CT) which was described in an earlier section. The total potential can be described as follows

$$V(r_\mu) = \begin{cases} V_1(r_\mu) & r < R_O \text{ (oxygens only, otherwise, use } V_2) \\ V_2(r_\mu)\, r \geq R_O \text{ (all ions)} \end{cases}$$

in which $V_1(r_\mu)$ is the Morse potential

$$V_1(r_\mu) = \sum_{j=NN} \left(D_o(1 - e^{-\alpha(r_{\mu j}-r_o)})^2 - D_o \right)$$

where D_0 (eV) is a constant associated with μO^- bonding, NN is short for "nearest neighbor," r_0 (Å) is the μ-O bond distance, and α (Å^{-1}) is a parameter associated with the strength of the μO^- bond; and $V_2(r_\mu)$ (eV) is associated with the Ewald summation

$$V_2(r_\mu) = \frac{4\pi}{\Delta} \frac{e_\mu}{4\pi\epsilon_o(\epsilon_r)} \sum_G^\infty \left(\frac{S(G)\exp\left(\frac{-G^2}{4\eta}\right)\cos(G \cdot r_{\mu j})}{G^2} \right)$$

$$+ \frac{e_\mu}{4\pi\epsilon_o(\epsilon_r)} \sum_{j=1}^\infty \left(\frac{2}{\sqrt{\pi}} \frac{q_j}{r_{\mu j}} \int_{r_o}^\infty \exp(-\eta r_{\mu j}^2)dr \right)$$

where **G** is a reciprocal lattice vector for the R123y structure, Δ is the volume of the unit cell {Δ = abc (Å^3)--where a, b, and c are the lattice constants of the crystal}, e_μ (C) is the charge of the μ^+, r_o (Å) is the μ-O bond distance, η (Å^{-2}) is an adjustable parameter proportional to the width of the Gaussian charge distribution (see next section for details), and S(**G**) is the appropriate structural factor with an ionic form factor ($f(r_{\mu j})$ = q_j),

$$S(\mathbf{G}) = \sum_{j=1}^{n(cell)} f(r_{\mu j}) \exp(\mathbf{G} \cdot \mathbf{r}_{\mu j})$$

where n(cell) is the number of ions in a single unit cell structure. The Ewald summation was calculated using a finite cell method, as was done for the RRP. Data from this summation were obtained using several values of η. By adjusting η, it is possible to find a value which yields faster convergence than a 1/R lattice summation. In the program, we found that we could obtain the same values for the potential energies using a wide variety of choices for η (.007 Å^{-2} < η < 1024 Å^{-2}).

As a sideline to the development of the Ewald method, the physical concepts associated with this method were employed in what will be referred to as the Dawson-Ewald method (DEM).

To utilize the DEM, we took advantage of the Gaussian charge distribution, which is the basis for the development of the Ewald method. The first term in $V_2(r_\mu)$ expresses the potential due to a Gaussian charge distribution (GCD), the second term (the integral)

expresses the overlap of the GCD into adjacent cells. Since η and $S(G)$ are functions of the spread of the charge distribution, the results from the Ewald method can be altered to describe a more covalent like charge distribution by simply dropping the second term in V_2 (*i.e.* dropping the integral). Further adaptations involve altering $S(G)$ to better describe the Fourier transform of the s-orbital wave functions. The process ultimately involves choosing individual values of η for each ion in the unit cell, in order to better describe ionic or covalent bahavior of that individual ion. Such an approach could also account for oxygen polarization. To do the same approach in the direct lattice, we would be forced to consider volume integration of the local regions in the lattice.

The reason for introducing this approach is that the s-orbitals can be easily approximated using Gaussian wave functions in the *variation method* used in quantum mechanics.[62,63] Although the results for the hydrogen atom are not exactly the same as a standard exponential s-wave function, they are close enough to justify the use of such a wave function in a variational calculation.[62,63] The calculations require a minimal increase in computer time, and can be run using the memory requirements of a typical IBM PC (equipped with an 80286 processor or better) or Macintosh (equipped with a 68020 processors or better). Therefore, since the wave function overlaps are better approximated with this method than they are with a classical calculation, and the computation time is roughly the same, this could improve to quality of muon search calculations.

An extensive quantity of data was obtained for various regions of the R123y lattice and compared with the ionic limit (the

calculations done using the classical ionic potential above); however, the method has yet to be employed for an actual search for possible muon-stop sites.

Preliminary results indicate that reasonable physical concepts can be retrieved from this method. First of all, when η is small, the Gaussian charge spread is large and we obtain a potential which resembles the free electron model as expected for metals. Likewise, when η is large, the charge spread approaches the same properties as a point charge and we obtain a potential which resembles the screened-Coulombic potential as expected for ionically bonded solids. The intermediate results for a narrow range ($0.25 \text{ Å}^{-2} < \eta < 1.0 \text{ Å}^{-2}$) exhibit behavior which suggest CuH bonding and need to be studied in greater detail. The CuH bonding was observed in Restricted-Hartree-Fock (RHF-SCF) cluster calculations for certain charge distributions.[64,65] The dependence would appear to be correlated with the local abundance of positive (or negative) ions within the $0.25 \text{ Å}^{-2} < \eta < 1.0 \text{ Å}^{-2}$ range. (The values of η correspond to a Gaussian charge spread of $\frac{a}{8}$ to $\frac{a}{4}$, where a is the lattice constant of R123y.) Such a success for a rather simple approach would imply that this method may serve as a good starting basis for the more accurate cluster calculations, especially since a general picture can be obtained in a fraction of the time required by RHF-SCF or UHF-SCF calculations.

3.5. Magnetic Dipole Field Calculations

For the magnetic fields measured by the muon spin probe, the major source of fields is assumed to be dipolar in nature. These fields come from magnetic rare-earth moments like the Gd^{3+} moment $(7.4 \pm 0.6 \ \mu_B)$[66-69] for $GdBa_2Cu_3O_7$. Other sources like supertransfer fields are presently not considered. Because of the $\frac{1}{r^3}$ dependence in the dipolar fields, these calculations are performed with the Lorentz sphere method.[32-34]

The magnetic-dipole-field calculations were performed using data from the magnetic moments obtained in the literature. The calculations are based on the classical expression for the interaction of two magnetic dipoles

$$B(r_\mu) = \frac{\mu_o}{4\pi} \mu_B \sum_{j=1}^{\infty} \left(\frac{3(m_j \cdot r_{\mu j})r_{\mu j} - m_j r_{\mu j}^2}{r_{\mu j}^5} \right).$$

where m_j (in units of Bohr magneton [μ_B]) is the magnetic moment on the jth ion, $r_{\mu j}$ (Å) is the distance of the muon from the jth oxygen, and $B(r_\mu)$ is the magnetic field (kOe) as seen by the muon at the position r_μ. The constant $(\frac{\mu_o}{4\pi} \mu_B)$ is equal to 9.27 kOeÅ^3.

As discussed in chapter two, the magnitude of the magnetic field at the muon site is proportional to the frequency through the equation

$$f = \frac{\gamma_\mu}{2\pi} |B|,$$

where |B| is the magnitude of the local magnetic field as seen by the muon, and γ_μ is the gyromagnetic ratio of the muon.

If the magnetic structure of the oxide is known, then the dipole fields can be calculated. The μSR frequency and relaxation data can then be compared with dipole calculations based upon the magnitude that is obtained for the magnetic field. The frequency is the major source of information; however, the relaxation data should correspond to the relative distribution of local fields at the muon site. If that local fields are non-uniform, then the relaxation rates should be large; the converse is also true.

3.6. Summary

The reasoning behind a search calculation for the muon sites in most transition metal oxide has been discussed. The selection of the potential energy functions is presented by way of a comparison of three standard semi-empirical diatomic bonding potentials. A brief discussion of magnetic dipole calculations is also presented.

In the next chapter, the proposed search method will be used to determine the muon-stop sites in $RBa_2Cu_3O_7$, and $RBa_2Cu_3O_6$ (R1237: R = Gd, Ho; and R1236: R = Er, Y), based upon the magnetic dipole calculations and potential energy calculations

Chapter 4

Zero Field μSR on $RBa_2Cu_3O_7$ and $RBa_2Cu_3O_6$

4.1. Introduction

In this chapter, we utilize to search calculations discussed in chapter three, and try to determine where the muon is localizing in $RBa_2Cu_3O_7$ (R1237) and $RBa_2Cu_3O_6$ (R1236). Based upon where the muon localizes in these R123y structures, we make some postulates which will later be used and/or developed in chapters five, six, and seven.

A complete table of zero field results for the fundamental R1237 and R1236 structures is provided in Tables I and II. The results from these tables will be used to establish the muon-stop sites in the samples discussed in chapters five and six. We will first discuss the zero field (ZF) results for the rare-earth doped R1237 (R ordering) followed by the ZF results for oxygen depleted samples of R1236 (Cu ordering).

In the sections that follow, we define the magnetic moment (μ) of an ion (I) by the symbol μ_I. Values of μ_I will be expressed in units of Bohr magnetons ($\mu_B = 9.24 \times 10^{-24}$ J/T). The magnetic moment of the rare-earth ions (R) will be expressed as μ_R, the Cu in the CuO-planes as $\mu_{Cu(pl)}$, and the Cu in the CuO-chains as $\mu_{Cu(ch)}$.

Table I. Potential energy minima, predicted μSR signals (from MDF calculations), and observed μSR frequencies for samples of GdBa$_2$Cu$_3$O$_{7.0}$ (Gd1237), GdBa$_2$Cu$_3$O$_{6.5}$ [Gd123(6.5)], and also HoBa$_2$Cu$_3$O$_{7.0}$ (Ho1237).

positions			potential energy (Gd1237) (eV)	GdBa$_2$Cu$_3$O$_{6+\delta}$ system			HoBa$_2$Cu$_3$O$_{6+\delta}$ system		name of site
				predicted (MDF) frequency Gd123(6.5) (MHz)	predicted (MDF) frequency Gd1237 (MHz)	observed frequency (Gd1237) (MHz)	predicted (MDF) frequency Ho1237 (MHz)	observed frequency (Ho1237) (MHz)	
x/a	y/b	z/c							
0.00	0.16	0.230		14					Art
0.00	0.50	0.290		67	75				Brutus
0.00	0.52	0.470		119					Son
0.24	0.56	0.345		189					Denny
0.03	0.40	0.083	-1.53	4.19	5.3	4.6			Lin(1)
0.02	0.56	0.087	-1.48	4.54	5.7	4.6			Lin(2)
0.25	0.40	0.000	-1.25	2.71	2				Lin(3)
0.00	0.27	0.108	-1.32	4.77	5.4	4.6			Balmer(1)
0.27	0.01	0.137	-0.72	6.91	7.6	7.0	2.8	2.4	Balmer(2)

Table II. Potential energy minima, predicted µSR signals (from MDF calculations), and observed µSR frequencies for samples of YBa$_2$Cu$_3$O$_{6+\delta}$ [Y123(6+δ): 0.0 < δ < 0.4]. The model is applied to data from YBa$_2$Cu$_3$O$_6$(Y1236), HoBa$_2$Cu$_3$O$_6$ (Ho1236), and ErBa$_2$Cu$_3$O$_6$ (Er1236). Note: in these materials, the source of magnetic ordering is from the Cu ions, and that the material has two Néel temperatures. (Tq refers to the model proposed by Tranquada et al. and Ly refers to the model proposed by Lynn et al.)

name of muon site	predicted (MDF) frequencies				observed µSR frequencies			
	T > T_N2 (MHz)	T < T_N2 Tq#1 (MHz)	T < T_N2 Tq#2 (MHz)	T < T_N2 Ly (MHz)	Ho1236 T < T_N2 (MHz)	Er1236 T < T_N2 (MHz)	Er1236 T > T_N2 (MHz)	Y1236 T > T_N2 (MHz)
Art(1)	15.6	11.	27.	24.3				
Art(2)	19.2	13.	32.	33.				
Brutus	0.	0.	0.	0.	0.	0.	0.	0.
Son	0.	0.	0.	0.	0.	0.	0.	0.
Denny(1)	19.9	14.	34.	33.4		34.		19.
Denny(2)	20.5	14.	35.	35.		34.		19.
Lin(1)	0.4	0.9	3.6	5.4				
Lin(2)	0.4	0.9	3.6	5.4				
Lin(3)	0.3	2.	9.	18.				
Balmer(1)	1.4	2.2	7.9	9.7				
Balmer(2)	4.0	2.1	4.8	18.	4.0	4.9	5.4	4.2
Balmer(2)p	2.3	2.4	7.5	3.3	4.5	7.4	3.9	1.9
magnitude of Cu moments	(µB)	(µB)	(µB)	(µB)				
planes	0.57	0.40	0.96	0.97				
chains	0.00	0.040	0.192	0.46				

4.2. Zero Field Measurements on $GdBa_2Cu_3O_7$

The dipole fields for the Gd were calculated for both the antiferromagnetic (AFM) structure (proposed by McK. Paul et al.)[66,68] of $GdBa_2Cu_3O_{6+\delta}$ ($\delta \approx 1.0$) ($\mu_{Gd} = 7.4 \pm 0.6 \mu_B$) and the ferromagnetic (FM) structure[70] of $GdBa_2Cu_3O_{6+\delta}$ ($\delta \approx 0.5$) ($\mu_{Gd} = 6.9 \pm 0.7 \mu_B$), Table I. Potential-energy calculations were performed for a $RBa_2Cu_3O_7$ with average lattice constants calculated from LePage et al.,[71-73] and for $GdBa_2Cu_3O_7$. The results for Ho1237 are confirmed in a study made by P. Birrer et al., and by Y. Kuno et al.[67,74,75]

Our original studies on $GdBa_2Cu_3O_{6+\delta}$ ($\delta \approx 1$) (Table I), where the magnetic ordering along the c axis is antiferromagnetic, show μSR frequencies which also approach the experimentally observed data. We conclude that the muon localizes at the B2 site in all $RBa_2Cu_3O_{6+\delta}$ ($\delta = 0.0, 0.5, 1.0$) samples based upon the dipole calculations. The results suggest that there is some degree of the covalent bonding between the Cu(2) and the μO^- in $RBa_2Cu_3O_{6+\delta}$ (see chapter seven). However, there is also evidence of ionicity in these materials because we were able to approximate the μ^+-stop sites using classical potential energy functions. Thus, the μ-O distance is near 1 Å and the μO^- bonding can be described successfully by the Rodriguez/Rüegg-potential (RRP) and the Morse-potential-with-Coulombic-tail (MPw/CT) methods (for detail see chapter three).

In Table I, the possible muon stop site candidates are given for $GdBa_2Cu_3O_7$, together with the calculated potential energies, μSR frequencies expected for these sites, and the observed μSR

frequencies. The order in which the candidate sites are given is with respect to energy; further, likely sites have been given a name. The Lin and Balmer sites are similar to those found in $RFeO_3$,[76-78] and to those found by chemical cluster calculations.[79,80] Note that the rare-earth orthoferrites possess a perovskite structure and the $RBa_2Cu_3O_7$ crystal have an oxygen deficient triperovskite (Pmmm) structure. In Figure 4.1, the Lin and Balmer sites are depicted in the lower half of the unit cell.

In Figures 4.2 through 4.4, it can be seen that the magnetic fields at the proposed muon-stop sites are uniform. We can therefore assume that the frequency of the muon signal is roughly constant and clearly visible to the spectrometer.

As one can see from Table I and Figure 4.1, candidates for muon probing sites are located near the oxygens. The oxygen vacancies and other symmetrical sites[84-86] are ruled out because they exhibit either a maximum or saddle point in their potential energy surfaces at the respective stop site. Furthermore, and even more important, the dipole-fields seen at the sites are often zero (due to symmetry), or are not acceptably close to the observed μ^+ frequencies.

Surprisingly, positions near the CuO-plane layers are much less favorable than near the CuO-chain layers. Although the CuO-plane layers are negatively charged, muon probe sites are not found due to the repelling effect of the R^{3+} ions. This has also been reported by K.C. Chan et al.,[87] and is further substantiated by the fact that the expected μSR frequencies for these "no-name" sites are much too high. The μSR frequencies for $GdBa_2Cu_3O_7$ (measured by Golnik et
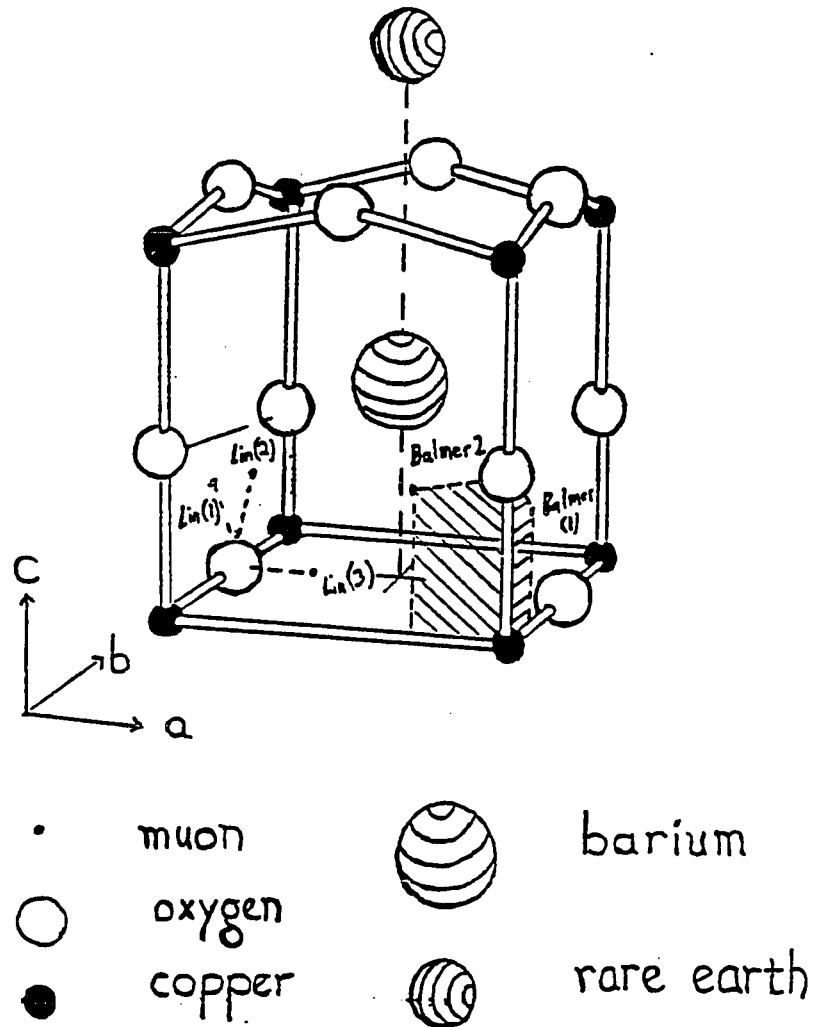
Figure 4.1. The location of the muon sites for $RBa_2Cu_3O_7$ (R = Dy, Eu, Er, Gd, Ho, Pr, Y, Y_xPr_{1-x}) based upon the magnetic dipole calculations and potential energy calculations. The Balmer(2) site (B2) appears in all of the $RBa_2Cu_3O_y$ structures so far investigated.

Figure 4.2. Local magnetic field distribution surrounding the B1 muon-stop site in Gd1237. The region is roughly 0.2 Å--a size greater than the zero-point vibrational amplitude. The grid indicates the magnitude of the internal magnetic field, and the arrows provide the direction of the field. The field seen at the B1 site is relatively uniform in direction (for Gd1237), and is estimated to have a (Gaussian) relaxation rate on the order of $\sigma = 1 \mu s^{-1}$

Balmer 1 site (B1)--$GdBa_2Cu_3O_7$
temperature range: $T < T_N$
scanning region:
$x/a = 0.000 \pm .075$
$y/b = 0.250 \pm .075$
$z/c = 0.108$

Figure 4.3. Local magnetic field distribution surrounding the B2 muon-stop site in Gd1237. The region is roughly 0.2 Å--a size greater than the zero-point vibrational amplitude. The grid indicates the magnitude of the internal magnetic field, and the arrows provide the direction of the field. The field seen at the B2 site is relatively uniform in direction (for Gd1237), and is estimated to have a (Gaussian) relaxation rate on the order of $\sigma = 1 \mu s^{-1}$

Balmer 2 site (B2)--$GdBa_2Cu_3O_7$
temperature range: $T < T_N$
scanning region:
$$x/a = 0.250 \pm .075$$
$$y/b = 0.000 \pm .075$$
$$z/c = 0.135$$

Figure 4.4. Local magnetic field distribution surrounding the L12 muon-stop site in Gd1237. The region is roughly 0.2 Å--a size greater than the zero-point vibrational amplitude. The grid indicates the magnitude of the internal magnetic field, and the arrows provide the direction of the field. The field seen at the L12 site is relatively uniform in direction (for Gd1237), and is estimated to have a (Gaussian) relaxation rate on the order of $\sigma = 1 \ \mu s^{-1}$

Lin 12 site (L12)--$GdBa_2Cu_3O_7$
temperature range: $T < T_N$
scanning region:
$$x/a = 0.000 \pm .075$$
$$y/b = 0.400 \pm .075$$
$$z/c = 0.084$$
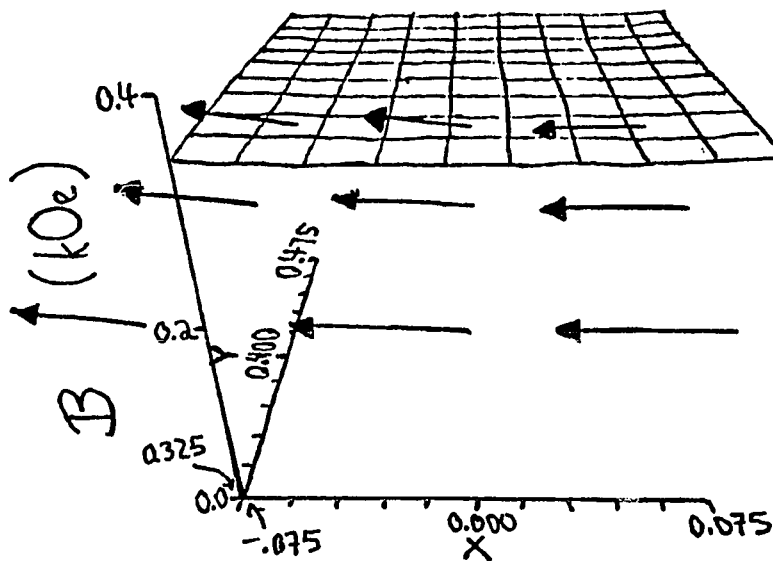
al.)[85] are 4.6 ± 0.2 MHz and 7.0 ± 0.2 MHz. In their $GdBa_2Cu_3O_y$ sample (with T_c = 60 K), the latter signal is much stronger than the former (which is hardly observed). Note that this feature is consistent with the fact that the 60-K $GdBa_2Cu_3O_y$ has many more oxygen vacancies in the CuO-chain layers (x ~ 6.6), thereby eliminating practically all of the Lin sites as μ^+-stop sites. The above indicates that all Lin and Balmer sites are good candidates for μ^+-stop sites in $RBa_2Cu_3O_{6+\delta}$.

4.3. Zero-Field Measurements on $YBa_2Cu_3O_{6+\delta}$

The observed zero field μSR measurements in $YBa_2Cu_3O_{6+\delta}$ ($\delta \approx$ 0) exhibit both a 4 MHz signal and a 19 MHz signal (Fig. 4.5).

The samples of Y1236 and Nd1236 have magnetic vacancies at the Y or Nd sites. Therefore, magnetic ordering is due solely to the Cu ions. The dipole fields for Y and Nd substituted R1236 oxides were calculated using the magnetic structure at zero Kelvin, as reported by Lynn *et al.* {Nd/Y: $\mu_{Cu(pl)}$ = 0.97 ± 0.09 μ_B (CuO-planes); $\mu_{Cu(ch)}$ = 0.46 ± 0.06 μ_B (CuO-chains)},[88] and the 80 K structure as proposed by Tranquada *et. al.* {Y: $\mu_{Cu(pl)}$ = 0.48 ± 0.08 μ_B (CuO-planes); $\mu_{Cu(ch)}$ = 0.00 ± 0.01 μ_B (CuO-chains)},[89-91] (see Table II).

The 4 MHz signal is most likely the Balmer(2) site (B2)--Figure 4.1. The uniform magnetic field seen at the B2 site is a strong indication that it is seen by the muon (Fig. 4.6).

The 19 MHz signal is most likely from the Denny site (D) (Fig. 4.5). The site exhibits a relatively uniform magnetic field with respect to the muon-stop site (Fig. 4.7).
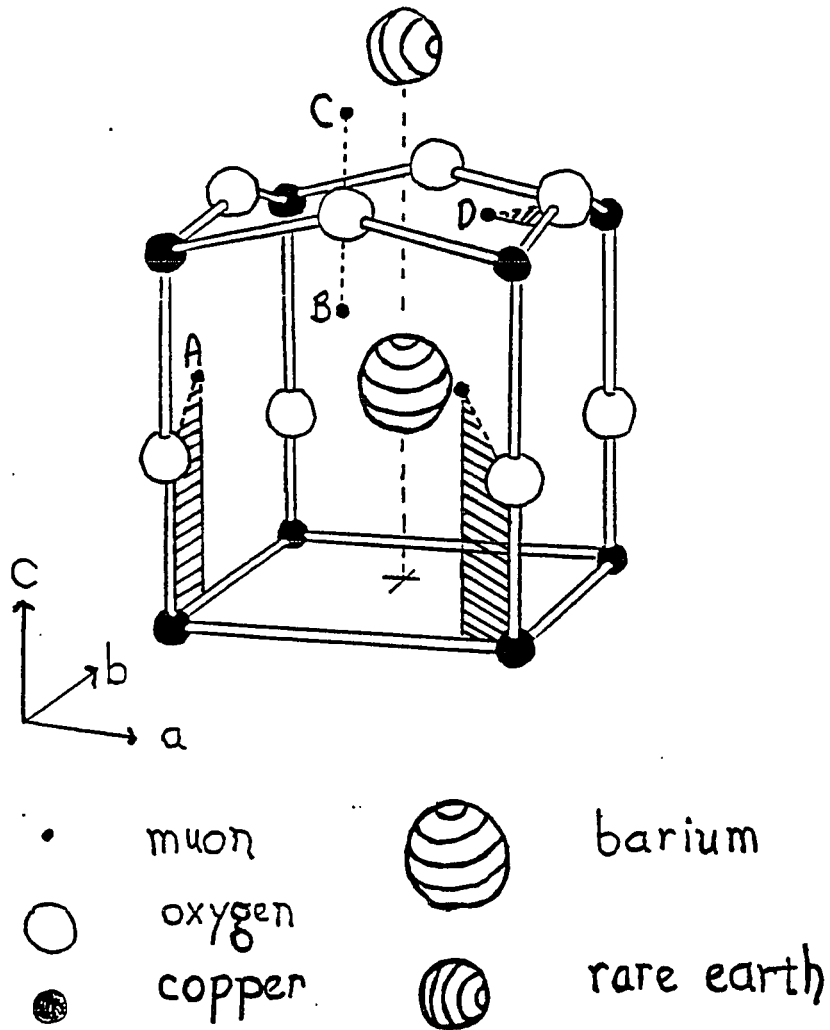
Figure 4.5. The location of the muon sites for $RBa_2Cu_3O_6$ (R = Er, Pr, Y, Y_xPr_{1-x}) based upon the magnetic dipole calculations and potential energy calculations. The Balmer(2) site (B2) appears in all of the $RBa_2Cu_3O_y$ structures so far investigated. The picture is based upon the potential-energy calculations.

Figure 4.6. Local magnetic field distribution surrounding the B2 muon-stop site in Y1236. The region is roughly 0.2 Å--a size greater than the zero-point vibrational amplitude. The grid indicates the magnitude of the internal magnetic field, and the arrows provide the direction of the field. The field seen at the B2 site is relatively uniform in direction and is estimated to have a (Gaussian) relaxation rate of $\sigma = 0.8 \ \mu s^{-1}$.

Balmer 2 site (B2)--$YBa_2Cu_3O_6$
temperature range: $T_{N2} < T < T_{N1}$
scanning region:

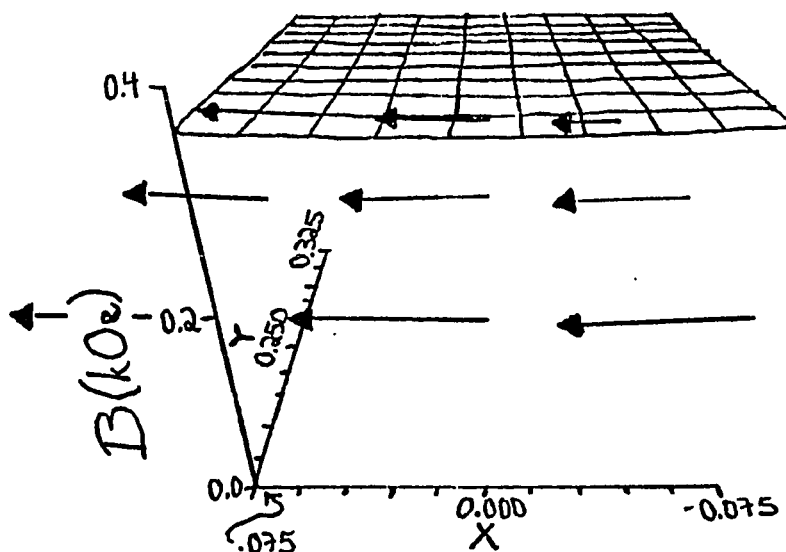$x/a = 0.270 \pm .075$
$y/b = 0.000 \pm .075$
$z/c = 0.135$
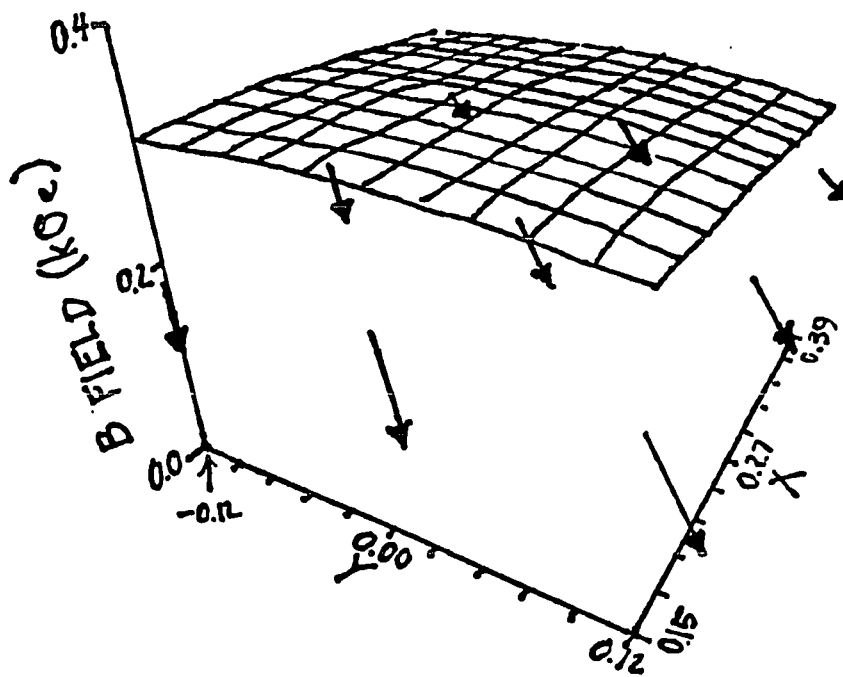
Figure 4.7. Local magnetic field distribution surrounding the Denny muon-stop sitein Y1236. The region is roughly 0.2 Å--a size greater than the zero-point vibrational amplitude. The grid indicates the magnitude of the internal magnetic field, and the arrows provide the direction of the field. The field seen at the Denny site is relatively uniform in direction but is estimated to have a (Gaussian) relaxation rate greater than $\sigma = 2 \ \mu s^{-1}$.

Denny site (D)--$YBa_2Cu_3O_6$
temperature range: $T_{N2} < T < T_{N1}$
scanning region:
$$x/a = 0.240 \pm .060$$
$$y/b = 0.560 \pm .060$$
$$z/c = 0.345$$
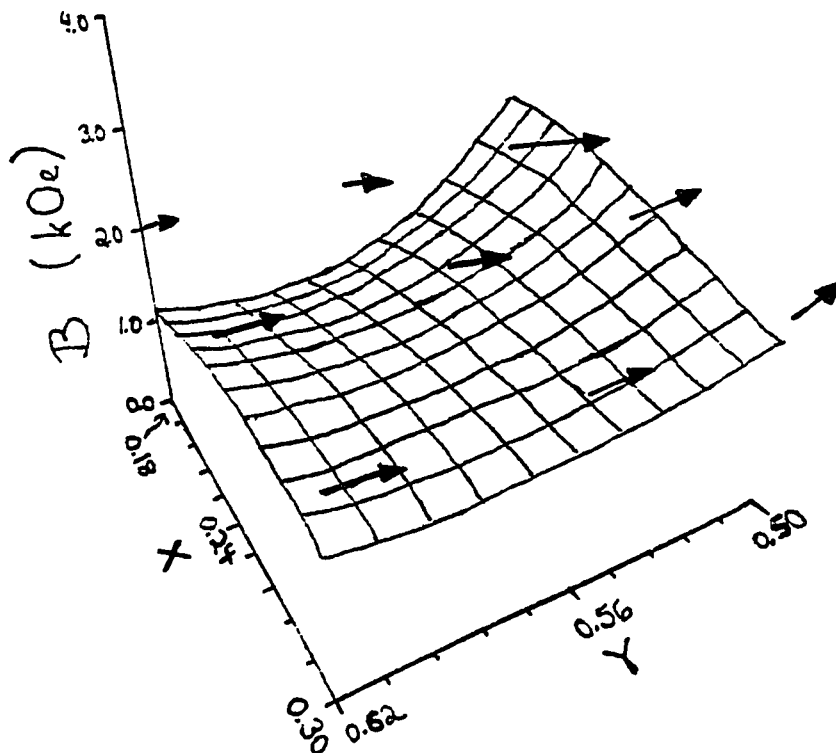
There is the possibility that the observed 19 MHz signal is actually an averaged combination of the signals from the Art site (A) and the D site (Fig. 4.5). In the Y1236 system, a barrier ($\Delta V_\mu \approx 0.4$ eV) exists between the A site and the Brutus site (B)--the nearest adjacent site. Therefore, little tunneling is likely between these two sites. On the other hand, there is a channel ($\Delta V_\mu \leq 0.1$ eV) between the B site and the D site--suggesting the possible presence of tunneling. However, it is more likely that the A site is simply not formed because its position relative to the Cu(2) and O(4) results in a weak Cu(2)-O(4) overlap and therefore creates a "highly strained" μO^- bond--raising the potential energy significantly. Furthermore, the relaxation rate seen at the Art site should be large, because the magnetic field distribution changes drastically in the local region surrounding the A site (Fig. 4.8).

There are indications that the researchers at KEK also found the field distributions seen at the Brutus site (B) (Fig. 4.9). The data contains a fast relaxing component (~ 20 μs^{-1}) with an asymmetry of 30% (approximately 1/3 of the total asymmetry).[92-93] The signal is attributed to possible "inhomogeneous static local fields" at the muon site. Research at LAMPF also reveals a zero frequency signal in $ErBa_2Cu_3O_{6+\delta}$ (mentioned below).

Evidence from LAMPF[94,95] on insulating $ErBa_2Cu_3O_{6+\delta}$ ($\delta = 0.2$) shows that the localization sites are a combination of the above two extremes. Data on these samples indicate two frequencies. At roughly 65 K, there is a shift in the frequency spectrum and asymmetry suggesting a phase transition in the magnetic structure. The most likely origin for this phase change is the presence of Cu(1)
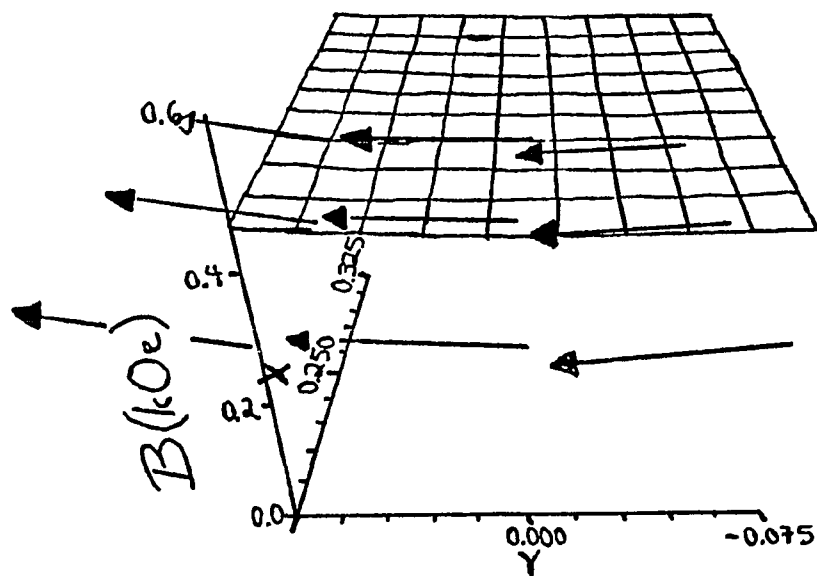
Figure 4.8. Local magnetic field distribution surrounding the Art muon-stop site in Y1236. The region is roughly 0.2 Å--a size greater than the zero-point vibrational amplitude. The grid indicates the magnitude of the internal magnetic field, and the arrows provide the direction of the field. The field seen at the Art site is not particularly uniform in direction and is estimated to have a (Gaussian) relaxation rate greater than $\sigma = 2. \ \mu s^{-1}$.

Art site (A)--$YBa_2Cu_3O_6$
temperature range: $T_{N2} < T < T_{N1}$
scanning region:

$x/a = 0.000 \pm .050$
$y/b = 0.160 \pm .050$
$z/c = 0.230$
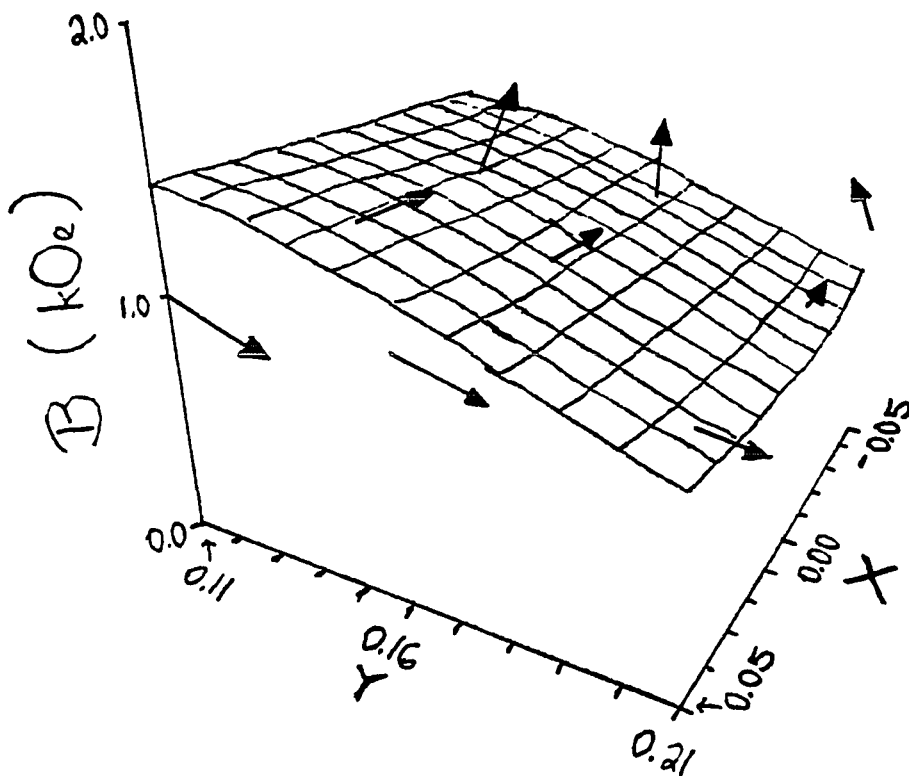
Figure 4.9. Local magnetic field distribution surrounding the Brutus muon-stop site in Y1236. The region is roughly 0.2 Å--a size greater than the zero-point vibrational amplitude. The grid indicates the magnitude of the internal magnetic field, and the arrows provide the direction of the field. The field seen at the Brutus site is extremely non-uni-form in direction and is estimated to have a (Gaussian) relaxation rate of $\sigma = 20 \ \mu s^{-1}$ according to the data at KEK (references 92 and 93).

Brutus site (B)--$YBa_2Cu_3O_6$
temperature range: $T_{N2} < T < T_{N1}$
scanning region:
$x/a = 0.000 \pm .120$
$y/b = 0.500 \pm .120$
$z/c = 0.290$
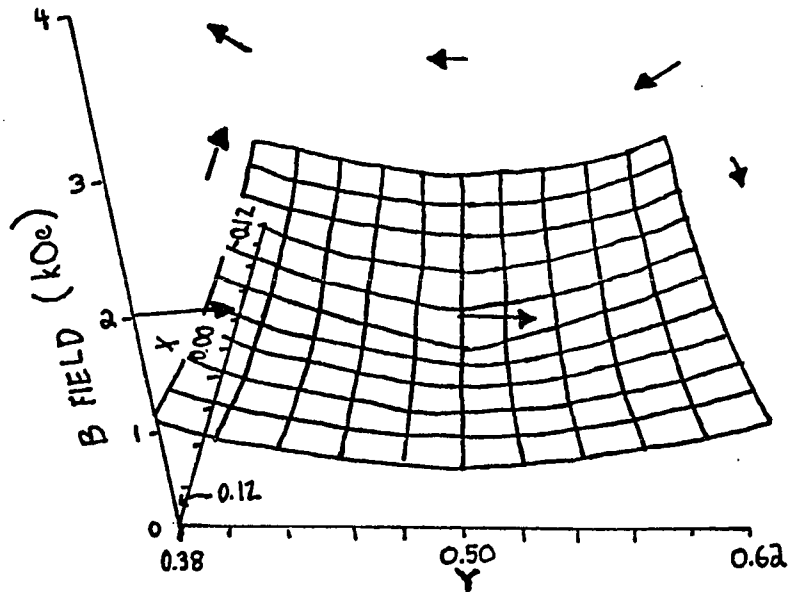
chain ordering, as has been seen in samples of Y1236. The two signals extrapolated to zero Kelvin are for the high temperature phase (3.9 and 5.4 MHz), and for the low temperature phase (4.9 and 7.4 MHz).[95] These two signals can be attributed to the chemically symmetrical Y1236 sites which exhibit non-equivalent magnetic environments. Two *weak* signals are also observed at zero Kelvin-- 34 MHz and roughly 0 MHz. The existence of small quantities of oxygen in the basal plane could bring about a signal from a region where the Balmer(2) site is located. *The Balmer(2) site is probably prevalent in all of these structures due to covalent tetrahedral bonding between the Cu(2)-O and the muon.*

In Table II, the possible muon stop site candidates are given for $RBa_2Cu_3O_6$, together with the calculated potential energies, calculated μSR frequencies (for the specific sites), and the observed μSR frequencies.

4.4. Discussion

In our studies, we found the following.

First, the experimental evidence when compared with the computational data indicates μ^+ localization in $RBa_2Cu_3O_{6+\delta}$ ($0.0 \leq \delta \leq 1.0$) occurs near the oxygens. The dominant μSR signal observed is from the Balmer(2) site (B2). The B2 signal is observed in nearly all oxygen concentrations ($0.0 \leq \delta \leq 1.0$). Other sites are often a composite of the two extremes for δ such as the Brutus and the Denny sites.

Second, The oxygen content strongly affects the muon localization, with the notable exception of the B2 site.

Third; the localization of the muon is independent of the choice of the lattice constants and/or the rare earth ion in $RBa_2Cu_3O_{6+\delta}$ (δ = 0.0, 0.5, 1.0).

Fourth, the use of the magnetic Cu structures as reported by neutron diffraction studies yield consistent results in our magnetic dipole-field calculations.

Last, our results suggest that a significant degree of the bonding in these transition-metal oxides is ionic.

In the potential energy calculations (PEC) on the $RBa_2Cu_3O_7$ (R1237) system (Fig. 4.1, Table I), we found that most of the candidate sites were located near the oxygens surrounding the basal plane[5] In sharp contrast, in the PEC on the $RBa_2Cu_3O_6$ (R1236) system, we found that most of the candidate sites reside near the oxygens located in the Cu-O planes (Fig. 4.5, Table II).

The major source of this contrast is due to the removal of oxygens in the basal plane. The remaining Cu^+ ions attract negatively charged particles. In the R1237 system, the comparatively large proportion of first and second nearest neighbor oxygens makes the potential energy relatively low in the basal plane. In the R1236 system, the larger number of first and second nearest neighbor oxygens are located around the Cu-O planes. Therefore, the net potential energy should drop in the Cu-O planes--relative to the Cu-Vacancy chains in the basal plane of the R1236 system.

Even though we see this shift in the PEC, the data from μSR still suggests that the B2 site is where the μ^+ goes. This is a strong indication that the μ^+ forms a covalent bond with the O^{2-} and $Cu^{2+\delta}$ at the B2 site. However, we also see the 0 MHz signal (the Brutus site) and the 19 MHz signal (the Denny site) in the Y1236 suggesting that there is a shift in the PE as predicted in the classical PEC. This is an indication that the structure is not exclusively covalently bonded.

A study of the μ^+-sites in R1237 as a function of the lattice constant has been performed. Very little change was observed in the relative location of the candidate sites (Table III). Table III is arranged according to increasing lattice constants in the c direction. The results show small fluctuations in the positions of the sites; however, the potential wells are shallow in the local regions (r $\approx$ 0.2 Å) surrounding the minima, so that these differences are not particularly significant ($\Delta V_\mu \leq 0.1$ eV), where V_μ is the local potential of the muon around r_0. In the local regions surrounding the muon-stop site, the potential energy changes were roughly linear and on the order of

$$\Delta V_\mu \approx (0.4 \text{ eV/Å}) \cdot r.$$

All of these calculations reveal a significant channel ($\Delta V_\mu \leq 0.1$ eV) is present in the region surrounding the Lin(1) and Lin(2) sites (L12). Within this region $\{\Delta(x/a) = \Delta(y/b) = 0.1, \Delta(z/c) = 0.03\}$, the muon should have enough zero point energy ($E_\mu \approx 0.1$ eV) to tunnel in the local regions surrounding these two sites.[32-34] This may be the reason for the comparatively weak signal associated with the L12 sites. The most notable variation occurs for the Lin(3) sites. A narrow horizontal channel is present along the b axis on either side

Table III(a). Variations of the ion positions with respect to the lattice constant.

rare earth ion	z/c ion position			lattice constant in (Å)		
	Ba	Cu	O	a	b	c
Pr	0.1840	0.3507	0.372	3.905	3.905	11.660
Gd	0.1855	0.3546	0.377	3.854	3.896	11.701
Y	0.1874	0.2365	0.379	3.827	3.877	11.708
Tm	0.1892	0.3595	0.380	3.529	3.860	11.715

Table III(b).   Variations in the minima with respect to the c axis lattice constant.

Balmer(1)	Pr1237	Gd1237	Y1237	Tm1237
x/a	0.00	0.00	0.20	0.00
y/b	0.26	0.27	0.26	0.27
z/c	0.110	0.105	0.110	0.105
U (eV)	-1.27	-1.32	-1.24	-1.32
Balmer(2)				
x/a	0.25	0.25	0.25	0.24
y/b	0.00	0.00	0.00	0.00
z/c	0.130	0.135	0.125	0.120
U (eV)	-0.71	-0.72	0.72	-0.78
Lin(1)				
x/a	0.00	0.00	0.00	0.00
y/b	0.40	0.40	0.40	0.42
z/c	0.088	0.084	0.840	0.088
U (eV)	-1.48	-1.52	-1.45	-1.52
Lin(2)				
x/a	0.00	0.00	0.00	0.00
y/b	0.60	0.60	0.60	0.58
z/c	0.088	0.084	0.840	0.088
U (eV)	-1.48	-1.52	-1.45	-1.52
Lin(3)				
x/a	0.26	0.26	0.28	0.28
y/b	0.46	0.44	0.50	0.48
z/c	0.010	0.010	0.000	0.000
U (eV)	-1.13	-1.26	-1.23	-1.29

of the oxygen (ΔV_μ < 0.1 eV) and another narrow vertical channel exists around the region (x/a = 0.26, y/b = 0.5) which leads directly xtoward the L12 sites. Such a channel may explain the absence of the predicted signal of $f_\mu \approx$ 2 MHz in Gd1237.[14]

We also conducted bandstructure calculations, using degenerate perturbation theory and tight binding approximations (using a pseudopotential in the Hamiltonian).[96] The program was written in the PASCAL language using a Convergent Technologies miniframe computer. A preliminary solution of the atomic wave functions, shows that the ratio of copper to oxygen valence should be about 0.7 for an overlap of the energies between the oxygens and the coppers to occur. This number is close to the ratio we assumed (0.8) in our potential energy calculations using the RRP. Indeed, when the predicted valences were applied to the PE calculations, for the B2 site was enhanced. We found the effective mass (m*) of the holes was roughly 15 m_e for this particular computational model; a value which compares with experimental results found in the literature (m*/m ~ 12).[97]

A study of alternative valence charge distributions (where Cu^v 1 ≤ v ≤ 2.5; and O^w -2.0 ≤ w ≤ -1.0) for the R1237 system shows that these changes do not adversely affect the localization of the candidate sites in the basal plane and, depending on the particular choice of the valence distribution, the localization tendency can even be enhanced (Tables IV, V, and VI). We could not allow for any Cu^{3+} ions when the oxygens were present in a state less than -2; therefore, we used various combinations of mixed valencies (time-averaged valence distributions) so we could incorporate at least some

Table IV. Alternative valence charge distrubutions for R1237 (Model A). The model reflect acceptable extremes in the oxygen valence, which was proposed to be -1 by some researchers, and introduces the effect of covalency in the rough approximation.

location	valence of the ion	
	O	Cu
planes	-1.5	1
chains	-1.333	1

name of stop-site	location			potential
	x/a	y/b	z/c	U (ev)
Lin(1)	0.00	0.32	0.07	-0.18
Lin(2)	0.00	0.68	0.07	-0.18
Balmer(1)	0.00	0.24	0.1 (not localized in region)	-0.06 (approximately)
Balmer(2)	0.24	0.00	0.13	0.39

Table V. Alternative valence charge distrubutions for R1237 (Model B). The model reflect acceptable extremes in the oxygen valence, which was proposed to be -1 by some researchers, and introduces the effect of covalency in the rough approximation.

location	charge valence	
	O	Cu
planes	-1.5	2
chains	-2	1

name of stop-site	location			potential
	x/a	y/b	z/c	U (ev)
Lin(1)	0.00	0.32	0.07	-2.27
Lin(2)	0.00	0.68	0.07	-2.27
Balmer(1)	0.00	0.24	0.1 (not localized in region)	-1.88 (approximately)
Balmer(2)	0.24	0.00	xxx (not localized in region)	-1.1 (approximately)

fraction of Cu^{3+} ($Cu^{+2.5}$ $Cu^{+2.25}$, *etc.*) into the Cu-O planes. By incorporating some Cu^{3+}, we have examined the possibility of this valence being present in the R1237 materials. Since the rare-earth ions and the barium ions are not expected to contribute a significant band overlaps with the conduction band of these materials (*i.e.*, they possess localized electrons), their valencies were fixed at +3 and +2 respectively. (The exception to this rule is Pr, which will be discussed in detail in an upcoming chapter.) We restricted the remaining valence choices to ones that would keep the net charge of the unit cell equal to zero.

Although the potential energies are different, the potential energy surfaces show wells in roughly similar regions. Model A (Table IV) is most likely the poorer representation of the overall charge distribution in the crystal since the total potential energy is much higher in all regions of the crystal lattice. Model B (Table V) does not show evidence of muon localization at the B2 site because the a channel (moun-oxygen bridge) exists between the Lin sites and the Balmer sites. However, when the valences for the CuO-planes (from the bandstructure calculations above), are applied to this model a potential energy minimum is found in at the B2 site. In model C (Table VI), the valence of the rare-earth ion was reduced slightly to balance the net charge in the lattice ($R^{2.8+}$). There is evidence that a minute overlap is present on the Gd1237 since the structure orders antiferromagnetically. In model C, the charge on the Cu(2) was set at +2.5, and the O(2) and O(3) at -1.7. The evidence would suggest that the charge distributions do play a significant role in the determining the muon sites.

Table VI.   Alternative valence charge distrubutions for R1237 (Model C) -- Balmer(2) site.   The model reflect the values of the charges as predicted by the bandstructure calculations.   The rare-earth ion has a reduced charge due to minor covalency effects.

location	valence		
	O	Cu	R
planes	-1.7	2.5	
chains	- 2	1	
rare earth			2.8

name of stop-site	location			potential
	x/a	y/b	z/c	U (ev)
Balmer(2)	0.18	0.00	0.09	-1.58 (approximately)

In the R1236 system, the material is clearly an insulator. We expect that this material should show rather conventional charge valences on the basis of studies of other transition metal oxide insulators. Therefore, we chose Cu^{2+} for the Cu-O planes and Cu^{1+} for the Cu-V chains. The oxygen was assumed to have a valence of about -2. Aside form the notable exception of the presence of a B2 site, the Brutus and Denny sites have been observed. This suggests that there is a significant degree of ionic bonding in R1236, but that corrections for covalency effects is necessary.

4.5. Summary

In this chapter, the muon-stop sites were found by means of the PE calculations and the MDF calculations, which were discussed in chapter three. The results show one common trend: the Balmer(2) site is favored in all of the R123y oxide structures. In addition, the information suggests that the nature of the bonding is at least in part ionic, or the calculations would not have yielded sensible results.

In the chapters that follow, the location of the muon at the Balmer(2) site will be utilized to make further predictions about the nature of other doped structures not discussed in this chapter.

Chapter 5

Zero-Field μSR on Praseodymium Doped $YBa_2Cu_3O_y$

5.1. Introduction

Over the past number of years, muon spin relaxation (μSR) has resolved the magnetic structure of various oxide superconductors. Measurement of insulating phases of the superconducting perovskite structures has shown that the magnetic ordering is antiferromagnetic in $La_{2-x}Sr_xCuO_4$ and $RBa_2Cu_3O_{6+\delta}$ R123(6+δ) ($0 < \delta < .5$).[21-23,98-105]

The high temperature superconductors have challenged many long standing theories about magnetism and superconductivity. Shortly after the 90 K superconductor $YBa_2Cu_3O_7$ (Y1237) was discovered, the structure was doped with magnetic rare-earth ions such as Gd, Er, and Dy.[106] The expectation was that these rare-earth ions would cause a decrease in the T_c--a typical situation for the classical BCS superconductors. Researchers found no such change in T_c, with these magnetic rare-earth dopants. After these early experiments, it became increasingly clear that magnetism and superconductivity shared a rather unconventional relationship in these novel oxides.

In the series $RBa_2Cu_3O_y$ (R123y) with R = rare-earth, the oxide with R = Pr is a notable exception from superconductivity: Pr1237 is a magnetic semiconductor (Figs. 5.1 through 5.3).[106-112] The mixed series $(Pr_xY_{1-x})1237$ reveals a variety of electric and magnetic
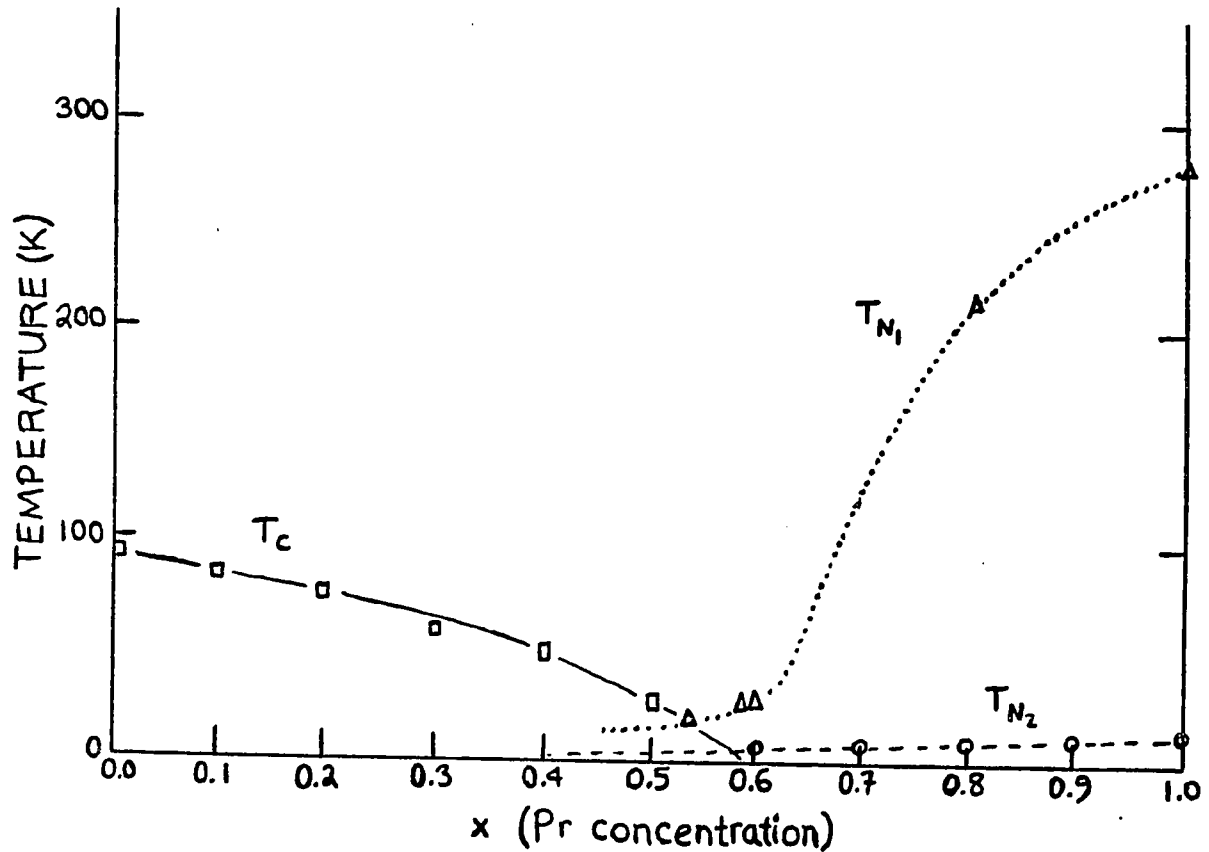
Figure 5.1. Measurement of transition temperature (T_{N1}, T_{N2}, and T_c) as a function of dopant concentration (x) for $(Pr_xY_{1-x})Ba_2Cu_3O_{7.0}$ ($0 \leq x \leq 1$). For $0.0 < x < 0.5$, the samples retain some degree of superconductivity. For $0.54 < x < 0.60$, the samples exhibits behavior reminiscent of a spin glass, and for $x > 0.6$, the sample becomes an antiferromagnet with magnetic structures as provide in a different frame. From D. W. Cooke et al., J. Appl. Phys. 67(9) (1990) 5061.
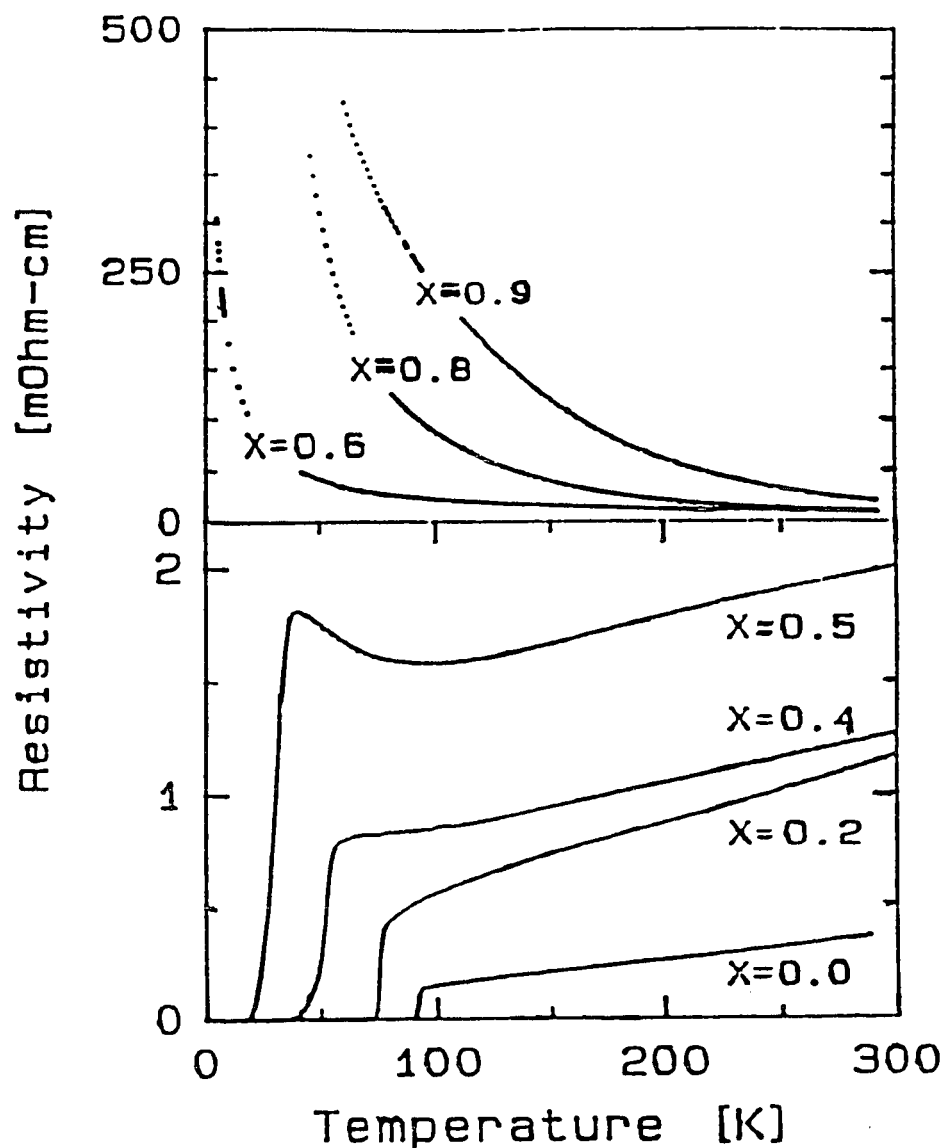
Figure 5.2. Measurement of resistivity as a function of temperature for praseodymium doped samples of $(Pr_xY_{1-x})Ba_2Cu_3O_{7.0}$. For $0.0 < x < 0.5$, the samples retain some degree of superconductivity. For $x > 0.5$, the samples become insulators with the presence of some form of magnetism (spin glass, antiferromagnet).

characteristics, especially near x ~ 0.55, where spin-glass-like behavior has been observed (Fig. 5.1).[21-23] Pr1236 also reveals quite remarkable magnetic properties in its insulating state (Fig. 5.4).[106-112]

Pr1237 shows three Néel temperatures: T_{N1} (about 285 K), T_{N2} (about 17 K), and an unexplained T_{N3} of 5.2 K. Below T_{N1}, Cu magnetism occurs in the Cu-O planes; below T_{N2} and/or T_{N3}, Pr magnetic ordering and/or Cu-O chain ordering exists (Fig. 5.3). Assigning T_{N2} to Pr magnetism implies rather unusual rare-earth magnetism with Néel temperatures two orders of magnitude higher than expected for typical magnetic rare-earth materials.[106-113] The alternative of additional Cu magnetism in the Cu-O-vacancy layers has been suggested from similar behavior in $YBa_2Cu_3O_{6+\delta}$ (when $0.0 \le \delta \le 0.4$). Further, this additional magnetism may invoke Pr magnetism at unusually high temperatures. Therefore, it is pertinent to determine if Pr magnetism exists at temperatures above, say, 10 K in Pr123y.

Muon spin relaxation (μSR) has helped in addressing this problem. We will examine zero-field (ZF) μSR results of $(Pr_xY_{1-x})123y$ (Refs. 21-23) and $PrBa_2(Cu_{1-z}Al_z)_3O_7$ (z = 0.08).[17] As the μ-probe site is presently well known in these oxides,[14-16] magnetic dipole fields can be calculated readily and compared to the observed fields. Specific magnetic structures as found by neutron-diffraction studies[88-91,114] are used and sometimes necessarily modified. The dipolar fields are compared to internal fields measured in the ZF-μSR experiments.[16,21-23,115]

In this chapter, we report the candidate muon-stop sites in the Pr1237 and Pr1236 structures. We predict magnetic structures of
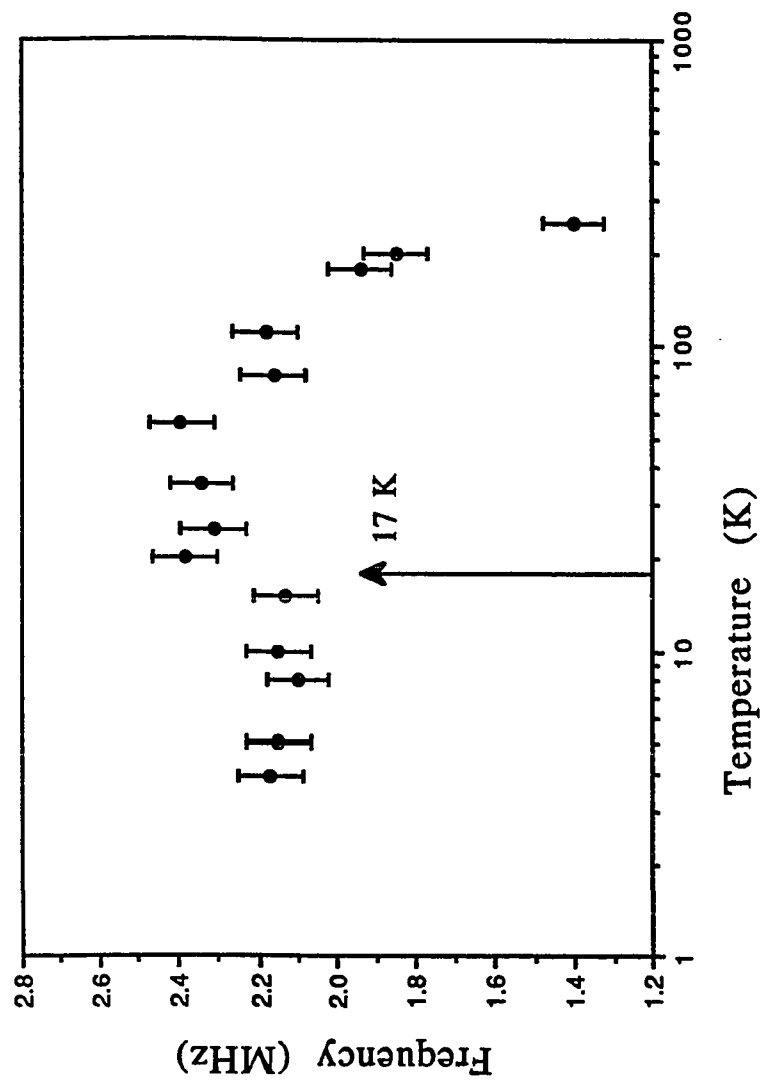
Figure 5.3. The frequency of the muon signal for $PrBa_2Cu_3O_7$. A large shift in the frequency is seen at 17 K an is attributed to the presence of a small magnetic moment on the Cu(1) ions. A similar shift is seen at 80 K for $YBa_2Cu_3O_{6+\delta}$. It is suspected that this shift will also be observed in $H_xYBa_2Cu_3O_7$.
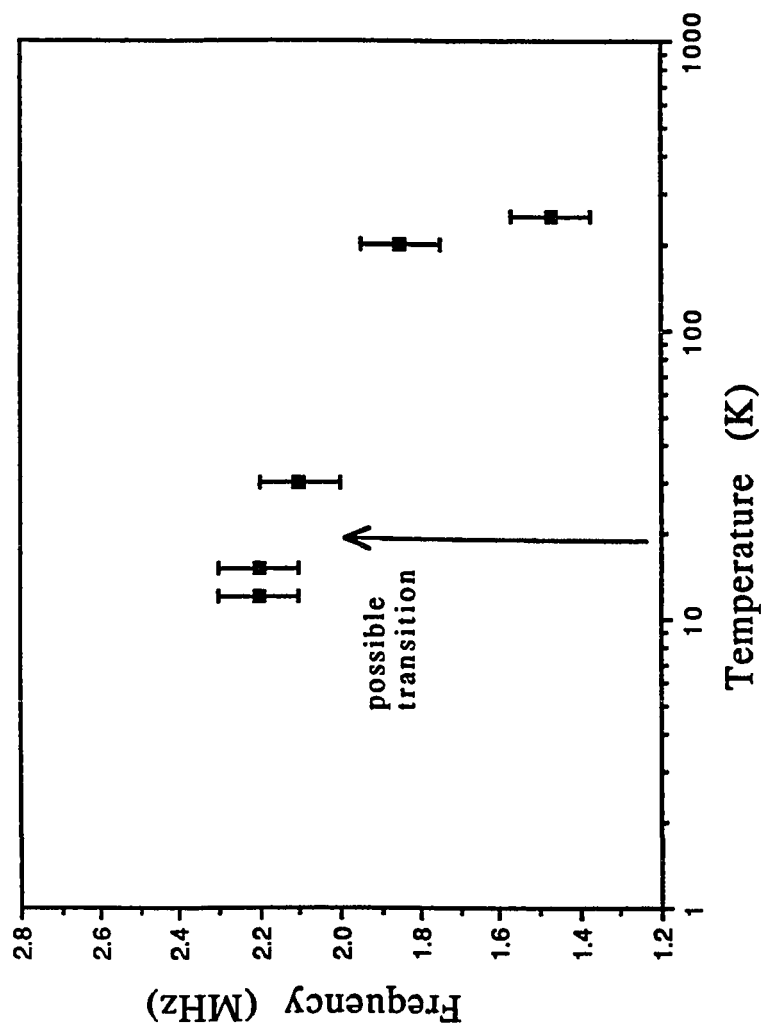
figure 5.4. The frequency of the muon signal for $PrBa_2Cu_3O_6$. A small hint of a shift in the frequency is seen around 10-20 K. In this structure and $PrBa_2(Al_xCu_{1-x})_3O_7$, it is not clear whether the shift is real or not based upon the accuracy of the experimental data.

the Pr123y (y = 6, 7) based upon structures determined by neutron diffraction on samples for $YBa_2Cu_3O_{6+\delta}$ ($\delta \sim 0$).

5.2. Physical properties of Pr1237 and Pr1236

Studies on $(Pr_xY_{1-x})Ba_2Cu_3O_7$ [$(Pr_xY_{1-x})1237$] provided a whole range of bulk magnetic properties, from antiferromagnetic insulator (0.6 < x < 1.0), to spin glass (0.55 < x < 0.60), to superconductor (0.00 < x < 0.55). The electrical properties of $(Pr_xY_{1-x})1237$ also exhibit a wide range of properties as a function of Pr concentration: from zero resistance, to semiconductor, to insulator[107-109,113] (Fig. 5.2). An examination of the magnetization curves between pure Pr1237 and Y1236 show similarities for T between T_{N1} and T_{N2} (T_{N2} = 80 K for Y1236, 65 K for Er1236, and 17 K for Pr1237 and Pr1236).[21-23]

When the magnetization for Pr1237 and Pr1236 (both non-superconducting) are examined, the phase transition is at the same temperature suggesting that the mechanism is similar.[21-22,113] The significant difference in physical properties of Pr doped samples is attributed to the 4+ valence state of the Pr.[117-119] Pr removes holes from the Cu-O planes via a 4f-3d overlap--the holes are attributed to the superconductivity of the Y1237. In our muon probe site determinations, we will focus our work on the pure Pr samples, since these samples eliminate any consideration about mixed (Pr:Y) contributions.

5.3. Summary of the Pertinant Background on μSR

The μSR technique is discussed in detail in chapter two. The results of ZF-μSR measurements for R1237 (R = Gd, Ho) and R1236 (R = Er, Ho, Nd, and Y) are discussed in detail in chapter four.

Briefly, three independent parameters are generated in zero field μSR: asymmetry, relaxation, and frequency. The relaxation rate provides information about the distribution of magnetic fields at the muon-stop site, the asymmetry--about the relative muon fraction occupying those sites, and the frequency--about the average magnetic field seen by the muon.

In order to make any specific interpretation of the results of the μSR data on the magnetic structure of Pr123y, we must know where the muon localizes. As discussed in chapter three, in well known oxide materials,[45-46,50-54] below 150 K, the muon bonds to the oxygens. We can approximate the muon location based upon potential-energy calculations and confirmed these sites using magnetic-dipole-field calculations and experimental ZF-μSR data. The result is two independent methods that locate the candidate muon probe sites.

Even at zero Kelvin, the muon has a zero-point (ZP) vibrational motion that has an amplitude of about 0.1 Å. As a result, the muon samples a distribution of magnetic fields in the local region surrounding the stopping site. Depending on the depth of the potential well and the temperature, the sample region can be much larger that the ZP region.

Since the relaxation rate is proportional to the width of the local field distribution, we can make a reasonable estimate of the relaxation rate from dipole calculations due to ZP motion. If the local magnetic field in the ZP region is uniform, then the μSR frequency signal will have a small relaxation rate (Figs. 5.5 and 5.6). If, on the other hand, the local magnetic field is non-uniform (a large distribution of fields and directions), the the muon spin will exhibit a high relaxation rate and rapidly loose its initial spin polarization (Fig. 5.7). For R1237, we find the ZP relaxation rate for the Balmer(2) (B2) site is about 0.6 μs^{-1} and for the other sites, these rates are higher by a factor of two or more.

5.4. Candidate Muon Stop Sites

In chapter four, we located the muon stop sites for R1237 and R1236. Two independent methods were used. Initially, the muon-stop sites were approximated using potential-energy (PE) calculations.[14,15] When a set of local minima were found, the magnetic dipole-field at the candidate sites were evaluated and compared with the values observed from ZF-μSR measurements.

In all of the previous calculations, we found similar results--the muon localizes at the Balmer(2) site (B2) and the Lin(12) sites (L12) (Fig. 5.8). The Gd, Ho and Er magnetic moments all order along the c axis while the Y1236 samples order along the a axis. In both cases, we determined that the muon bonds to the oxygen at the B2 site {O(4)}, suggesting significant covalent sp^3 hybridization between

Figure 5.5. Local magnetic field distribution surrounding the B2 muon-stop site in Pr1237. The region is roughly 0.2 Å--a size greater than the zero-point vibrational amplitude. The grid indicates the magnitude of the internal magnetic field, and the arrows provide the direction of the field. The field seen at the B2 site is relatively uniform in direction and is estimated to have a (Gaussian) relaxation rate of $\sigma = 0.8 \ \mu s^{-1}$.

Balmer 2 site (B2)--$PrBa_2Cu_3O_7$

temperature range: $T_{N2} < T < T_{N1}$

scanning region:

$x/a = 0.250 \pm .075$
$y/b = 0.000 \pm .075$
$z/c = 0.135$
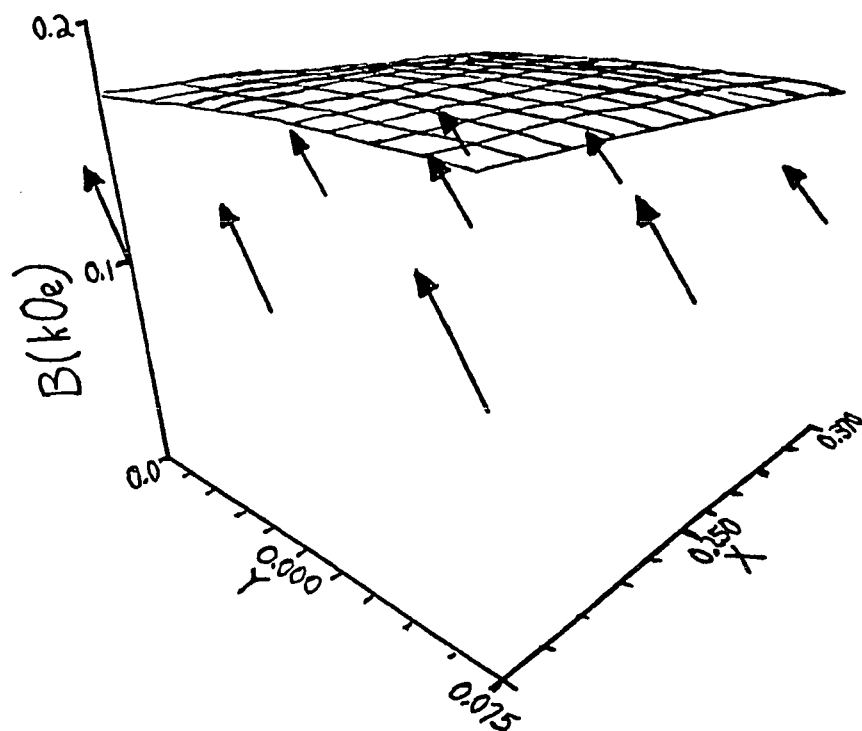
Figure 5.6. Local magnetic field distribution surrounding the B1 muon-stop site in Pr1237. The region is roughly 0.2 Å--a size greater than the zero-point vibrational amplitude. The grid indicates the magnitude of the internal magnetic field, and the arrows provide the direction of the field. The field seen at the B1 site is somewhat uniform in direction and is estimated to have a (Gaussian) relaxation rate of $\sigma = 2. \ \mu s^{-1}$.

Balmer 1 site (B1)--$PrBa_2Cu_3O_7$
temperature range: $T_{N2} < T < T_{N1}$
scanning region:
  x / a = 0.000 ± .075
  y / b = 0.250 ± .075
  z / c = 0.108
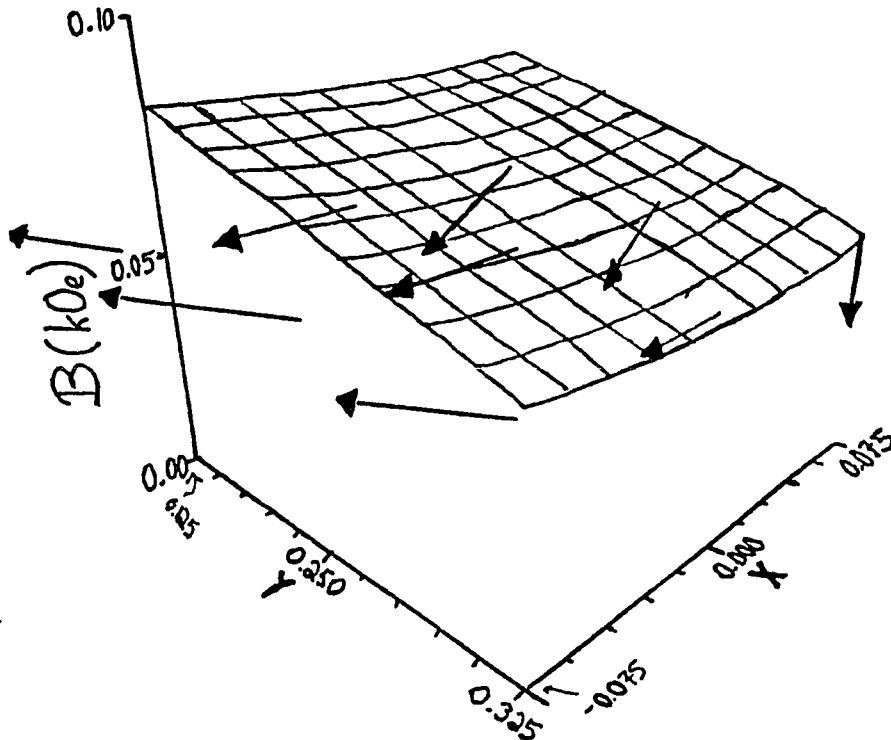
Figure 5.7. Local magnetic field distribution surrounding the L12 muon-stop site in Pr1237. The region is roughly 0.2 Å--a size greater than the zero-point vibrational amplitude. The grid indicates the magnitude of the internal magnetic field, and the arrows provide the direction of the field. The field seen at the L12 site is non-uniform in direction and as a result, the muon spin is rapidly depolarized by the local field distribution.

Lin 12 site (L12)--$PrBa_2Cu_3O_7$

temperature range: $T_{N2} < T < T_{N1}$

scanning region:

x/a = 0.000 ± .075
y/b = 0.400 ± .075
z/c = 0.084
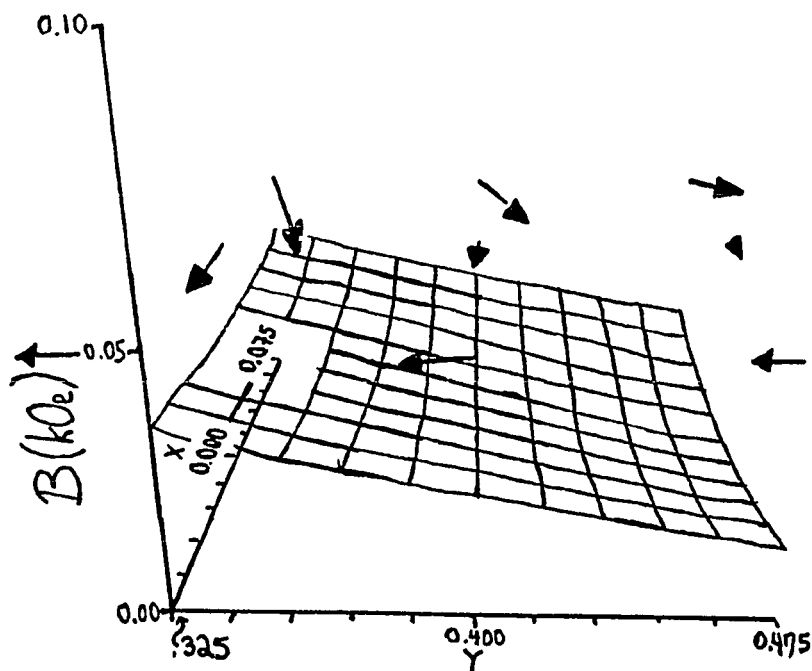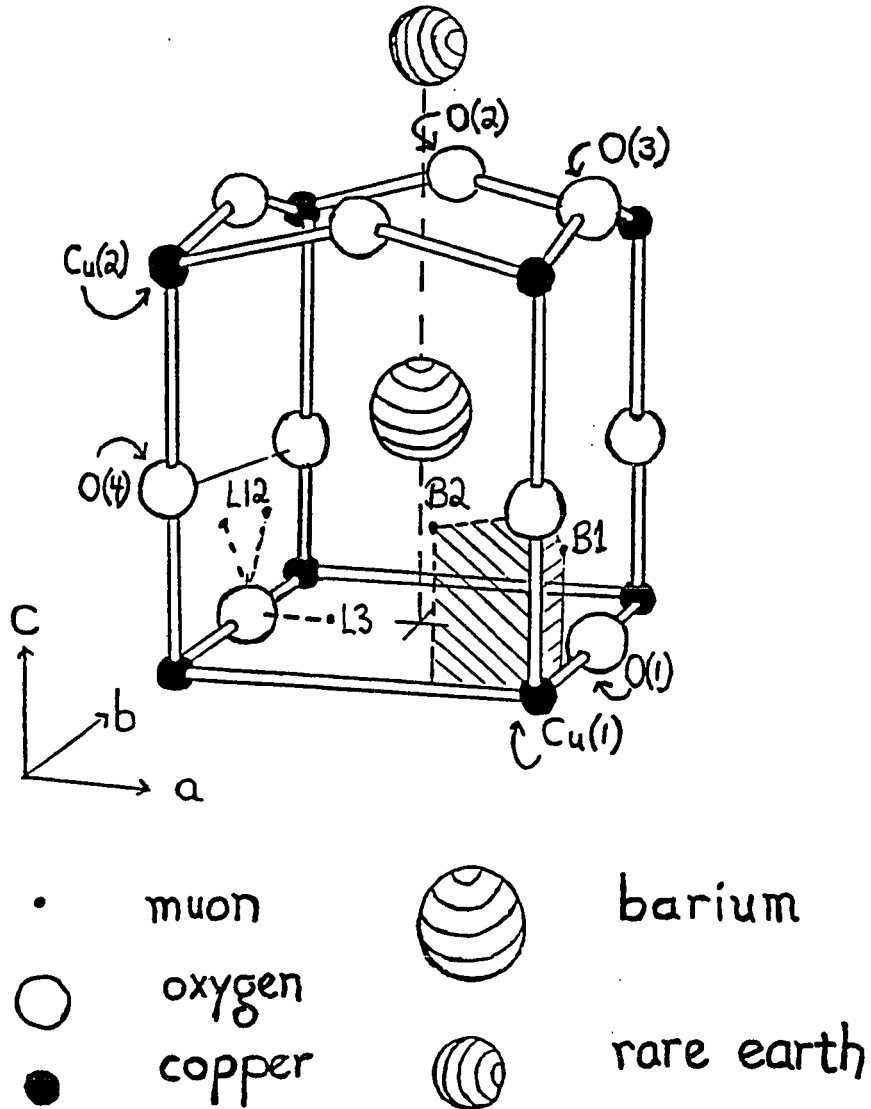
Figure 5.8. The location of the muon sites for $(Pr_xY_{1-x})Ba_2Cu_3O_{7.0}$ based upon the magnetic dipole calculations and potential energy calculations. The Balmer(2) site (B2) appears in all of the $RBa_2Cu_3O_y$ structures so far investigated.

the muon and the oxygen (OH⁻ like) and the d_{z2} orbital from the Cu ions located in the Cu-O planes. Similar sp³ bonding angles are determined at the L12 sites for R123y. The field at the L12 site is not observed in this sample (Cu ordering) because of large changes in the direction of the magnetic field in the zero-point (ZP) vibration region of the oxygen (Fig. 5.7). We note that, recently, these candidate sites were confirmed using restricted Hartree Fock calculations (RHF-SCF).[64-65]

Summarizing Pr1237 and Pr1236, according to the potential energy calculations, the muon stop sites are located in about the same positions as R1237 structure and the R1236 structure respectively (R = Gd, Nd, Y, *etc.*). Although there is a significant change in the valence of the Pr, there is an equal reduction in the number of holes occupying the Cu-O planes. The net result is that the potential energy does not change significantly from similar results in Pr1237. For the same reasons, we see a similar case for Pr1236.

5.5. μSR data for Pr1237 and Pr1236

ZF-μSR analysis on $(Pr_xY_{1-x})123y$ was performed at LAMPF (Figs. 5.1 5.3,and 5.4).[16,17,21-23] The ZF frequency ranges from 1.5 to 2.3 MHz (decreasing with decreasing x) when $(Pr_xY_{1-x})Ba_2Cu_3O_{6+\delta}$ ($0.6 \le x \le 1.0$), extrapolated to zero Kelvin from runs recorded above T_{N2} (see Fig. 5.1). The major μSR signal observed for Pr1237 has an extrapolated (to 0 K) frequency of 2.3 ± 0.1 MHz (see Fig. 5.3). This signal follows a magnetization curve, except for a transition near

$T_{N2}(x)$ below which for $x = 1.0$ and 0.8 a significant decrease in frequency is observed (see Figs. 5.1, and 5.3).

In Pr1236 (Fig. 5.4), two frequencies are observed between T_{N2} (12 K) and room temperature (RT): 2.2 and 4.7 MHz; the latter signal possessing the strongest intensity and showing signs of splitting at low temperature. Knowing the μ-probe sites, all signals are signatures of the magnetic μ^+ environment.

Owing to the similar discontinuity in the muon frequency spectrum of the Pr1236 and Pr1237 structures (17 K), and its similar temperature dependence $(T_{N2} < T < T_{N1})$,[21-23] we presume that the magnetic ordering is similar. At low temperatures (T < T_{N2}, $T_{N2} = 17$ K), there is a second phase transition (see Fig. 5.2). In the Y123y and Er123y ($6.0 \leq y < 6.4$), the phase transition corresponds to a change in Cu magnetism (Y: $T_{N2} = 80$ K, and Er: $T_{N2} = 65$ K). For Pr123y ($6 < y < 7$), this phase transition corresponds to $T_{N2} \approx 17$ K.

There is no evidence in the μSR LAMPF data to conclusively show that there is a shift in the Pr1236 system as is seen for the Pr1237 system. However, there is a hint in the Pr1236 data to suggest the presence of a shift in the frequency at roughly 14-17 K. The error in the frequency is greater than the shift; nevertheless, the shift in the data is in the same place for Pr1236 as Pr1237. Therefore, regardless of the actual mechanism which brings about this effect, the same kind of mechanism appears to be present in both the Pr123y samples ($6 < y < 7$), since both T_{N1} and T_{N2} are at about the same temperatures ($T_{N1} = 280$ K, $T_{N2} = 17$ K) and the magnitude of the fields seen by the muon are similar (0.16 kOe).

5.6. Interpretation of Data for Pr1236

To characterize the μ-probe sites in O-depleted Pr123(6+δ) we used the frequency and also the depolarization rate. As δ approaches zero, the crystal structure becomes more tetragonal and a B2 site can no longer be distinguished from its counter part (B2p) along the b axis. Although for $\delta = 0$ the two sites are chemically symmetric, they are *not* magnetically symmetric. Well below room temperature, two signals at 2.2 and 4.7 MHz are observed (Fig 5.4). We estimate from dipole calculations using 0.5 μ_B for the Cu magnetic moment in the Cu-O planes ($\mu_{Cu(pl)}$), the following ZP relaxation rates of 0.6 μs^{-1} for B2 and 1.8 μs^{-1} for the B2p. In our analysis of Pr1236-μSR results, we find 0.8 and 2.0 μs^{-1} for the relaxation rate of the 2.2 MHz and the 4.7 MHz signals, respectively. Thus, in addition to potential-energy calculations and the magnetic dipole calculations, a third independent method can be used to characterize the μ-stop site. Thus, we confirm[16] that $\mu_{Cu(pl)}$ is about 0.5 μ_B, about the size of the moment in Y1236.

We have not observed a frequency signal originating from the Denny site (D)[14,15] for Pr123y, as predicted by Y1236-μSR results,[14,16,115,116] because the Pr valency is nearly 4^+ and the positive muon will be repelled by this large positive charge.[14,15] The D site is therefore much less favored over sites near the BaO pianes.

5.7. Pr1237

In this section, we address the magnetic ordering in Pr1237 of the Cu(2) moment above T_{N2}, and the ordering of the Pr and/or Cu(1) moments below T_{N2}. If Pr orders, we start by assuming typical c axis ordering, which was seen in R1237 (R = Dy, Gd, Ho, Er), for the Pr moments, and a-b ordering, which was seen in R1236 (R = Y, Nd), for the CuO plane ordering ($\mu_{Cu(pl)}$). For the chain copper ordering ($\mu_{Cu(ch)}$) below T_{N2}, we have used different magnetic structures according to Lynn et al.,[88,114] Tranquada et al.,[89-91] and Weber et al.[120]

The B2 site is taken to be the μ-probe site on the basis of previous studies in other R1236 systems.[14-17] The charge from the Pr valence does not significantly change the muon location near the BaO planes, because the effective Cu valence is also reduced to compensate for the creation of Pr^{4+}.

As a first guess, magnetic ordering should follow a similar trend as in the Y1236 structure, i.e., the copper moments order along the ab directions (see Figs. 5.9 and 5.10). We choose the high temperature model in which the Cu moments order antiferromagnetically down to T_{N2}. Above T_{N2}, samples of Er1236 and Y1236 exhibit Cu magnetism with an ordered moment of approximately 0.66 μ_B.[95,121-124]

With these arguments in mind, we calibrated $\mu_{Cu(pl)}$ to a value that matched the observed μSR frequency of 2.3 MHz in Pr1237 (see Fig 5.3). This step also amounts to adjusting for possible covalency effects.[29-34] We find that the $\mu_{Cu(pl)}$ for Pr1237 is about 0.27 μ_B for
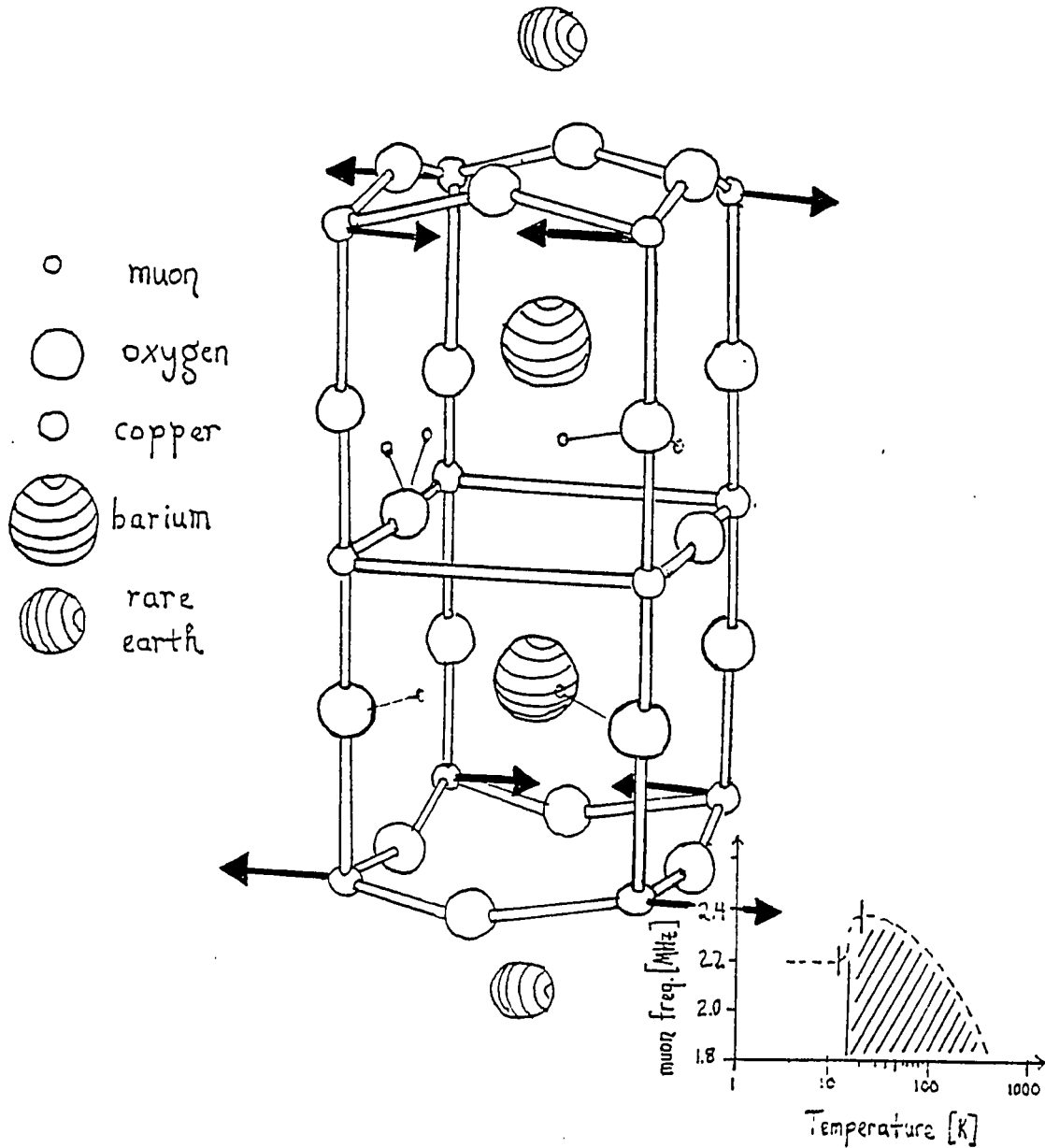
Figure 5.9. The proposed magnetic structure for $PrBa_2Cu_3O_7$ for 17 K
$\leq$ T $\leq$ 280 K. (T_{N1} = 280 K.) The structure exhibits an antiferromagnetic structure between the planes. The ab structure is antiferromagnetic. The structure is similar to what is observed for in $YBa_2Cu_3O_{6.0}$ (17 K < T), a structure proposed by both J. Tranquada *et al.* (references 89-90) and J. Lynn *et al.* (references 88, 114). The inset indicates the muon frequency within the specified temperature range.
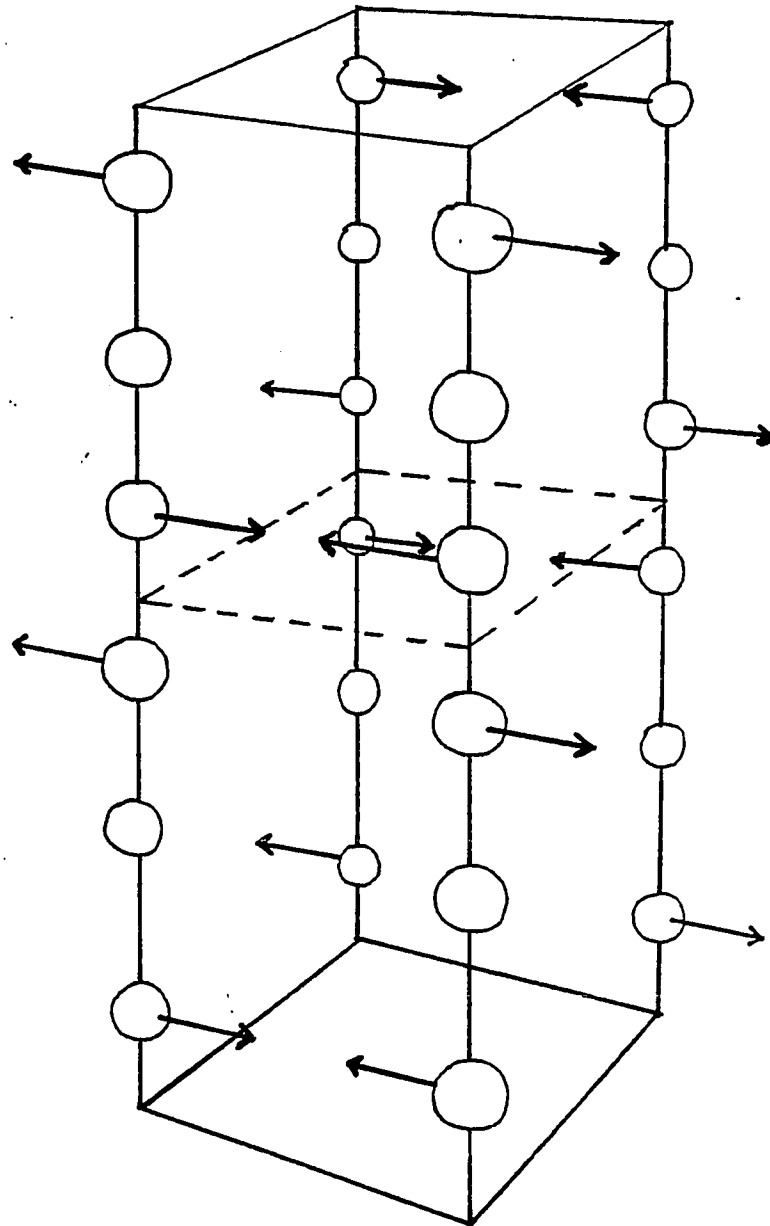
Figure 5.10. The magnetic sublattice structure for $PrBa_2Cu_3O_7$ for 17 K $\leq$ T $\leq$ 280 K. The structure is a three dimensional antiferromagnet between successive CuO-planes and no Cu(1) moment in the CuO-chains.

$T_{N2} < T < T_{N1}$, when extrapolated to 0 K. Band-structure calculations on Pr1237 predict a value of 0.25 μ_B at the Cu-plane sites.[125]

The reason for the reduction in the Cu moment is attributed to competition for holes between the hybridized dp Cu-O bands and the f bands from the Pr. The Pr is likely competing for the extra hole to form a 4^+ valence state while the Cu is competing for a $(2+\delta)^+$ valence state, where $0.0 < \delta < 0.5$. Such a situation would likely result in spin pairing and a reduction of itinerant exchange between electrons in successive Cu sites in the planes due to Pr hole trapping (hole filling mechanism).[126-127]

Below 17 K, the observed μSR signal drops to about 1.9 MHz (see Fig. 5.3). We have examined four possible explanations: (i) Pr ordering (c and a axis)[106-113] with no chain moment; (ii) copper chain ordering associated with the low-T model[89-91] proposed by Tranquada *et al.* (TQ); (iii) copper chain ordering with the low-T model[88,114] of Lynn *et al.* (LY); and (iv) Weber *et al.*[120] who suggest TQ or LY ordering along the 110 axis.

In the case of the Weber model, the $\mu_{Cu(pl)}$ moment has to be taken to be 0.34 μ_B in order to obtain the observed muon frequency above T_{N2} (extrapolated to 0 K). For the LY and TQ models, we kept $\mu_{Cu(pl)}$ at 0.27 μ_B above and below T_{N2}, because below T_{N2} Tranquada *et al.*[89-91] suggest a 20% decrease, whereas Lynn *et al.*[88,114] indicate a 20% increase in the low temperature magnetic moment $\mu_{Cu(pl)}$.

In Figure 5.11, we depict the model results which are qualitatively consistent with a decrease in frequency at T_{N2}. Pr ordering and/or the Weber approach predict an increase in
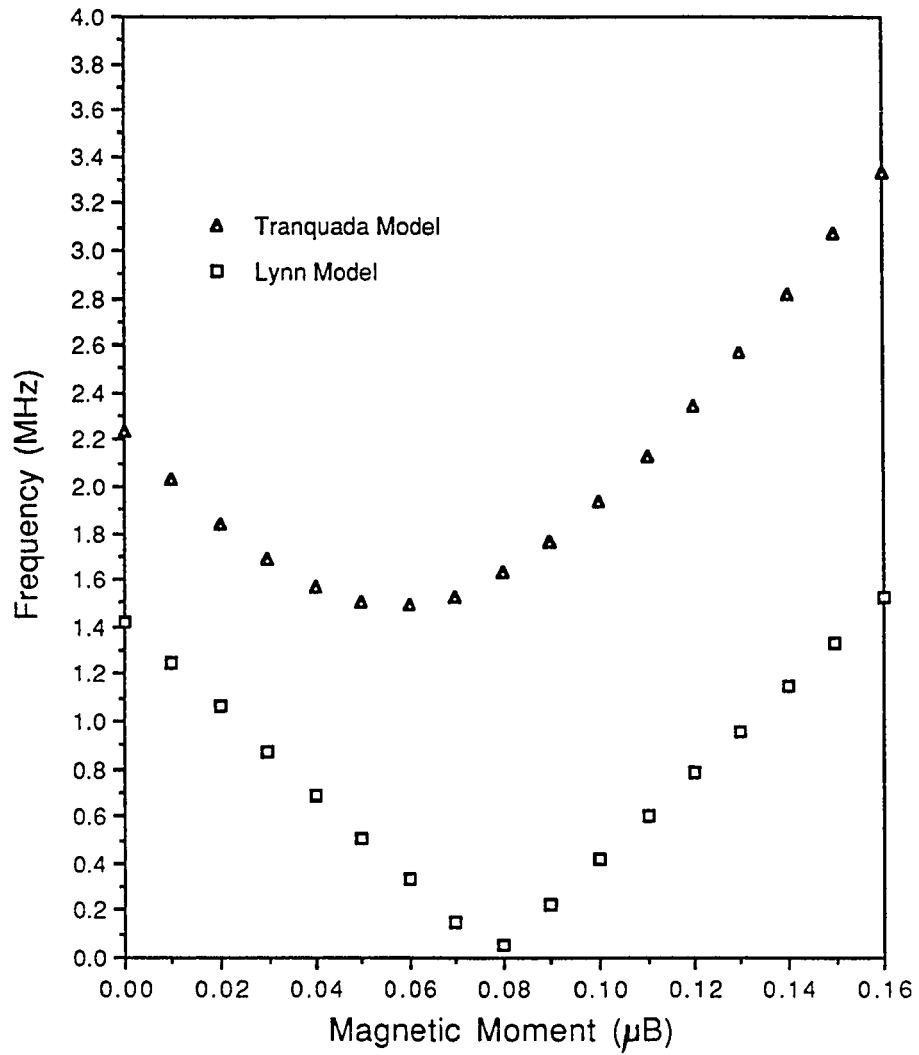
Figure 5.11. Predicted frequencies below T_{N2} with varying $\mu_{Cu(ch)}$ magnitude, according to LY (ref. 114) and TQ (ref. 89-91) models. At $\mu_{Cu(ch)} = 0.02$ and $0.1 \mu_B$, the TQ model predictions are in agreement with the observed μSR frequency below T_{N2}.
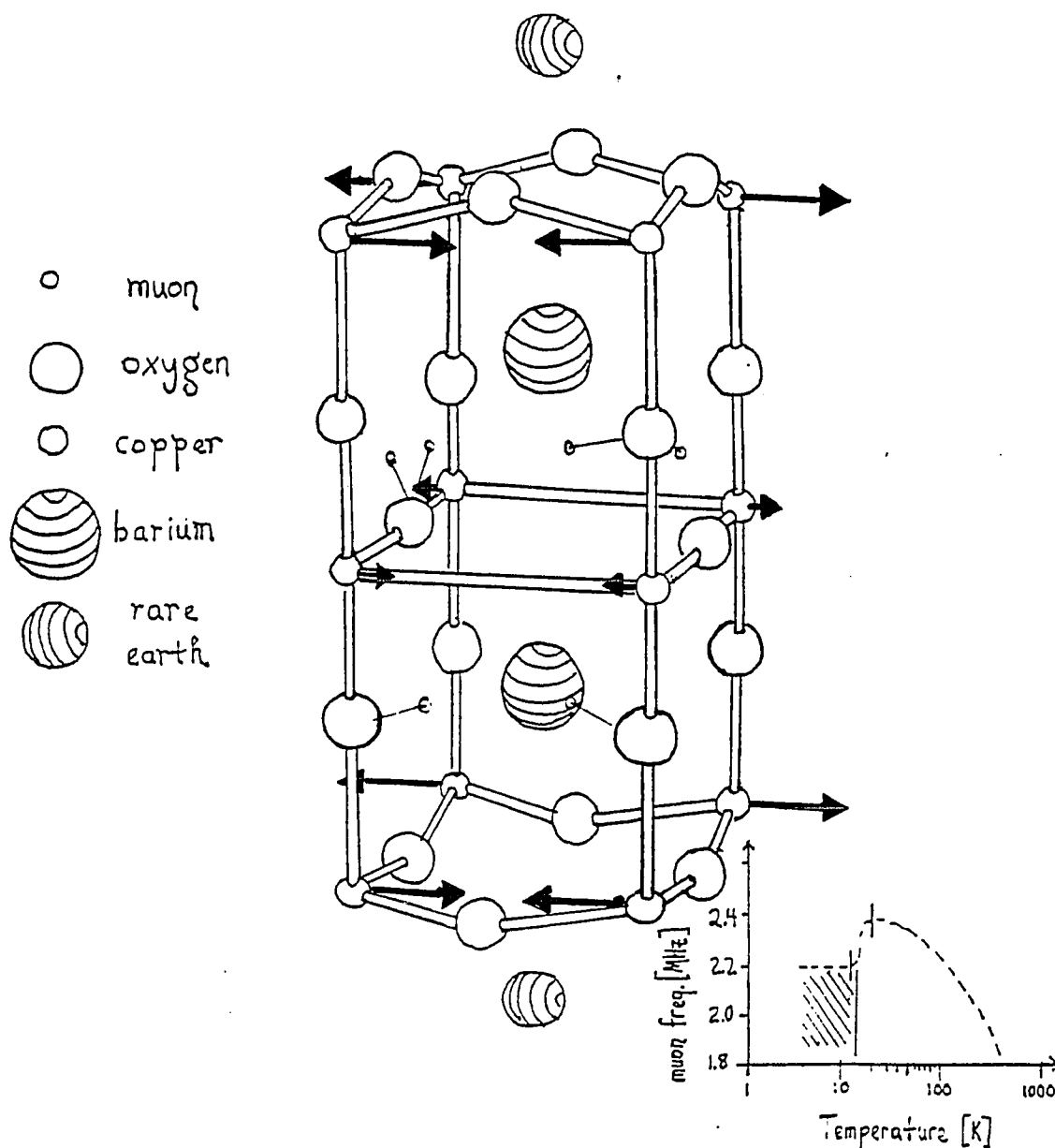
Figure 5.12. The proposed magnetic structure for $PrBa_2Cu_3O_7$ for 0 K ≤ T ≤ 17 K, (T_{N2} = 17 K). The structure exhibits a ferromagnetic structure between pairs of successive planes, and an antiferromagnetic structure between successive pairs of planes. The ab structure is antiferromagnetic like the higher temperature orientations. The structure is similar to what is observed in $YBa_2Cu_3O_{6.2}$ (0 K < T < 17 K), a structure proposed by J. Tranquada et al. (references 89-90). The inset indicates the muon frequency within the specified temperature range.
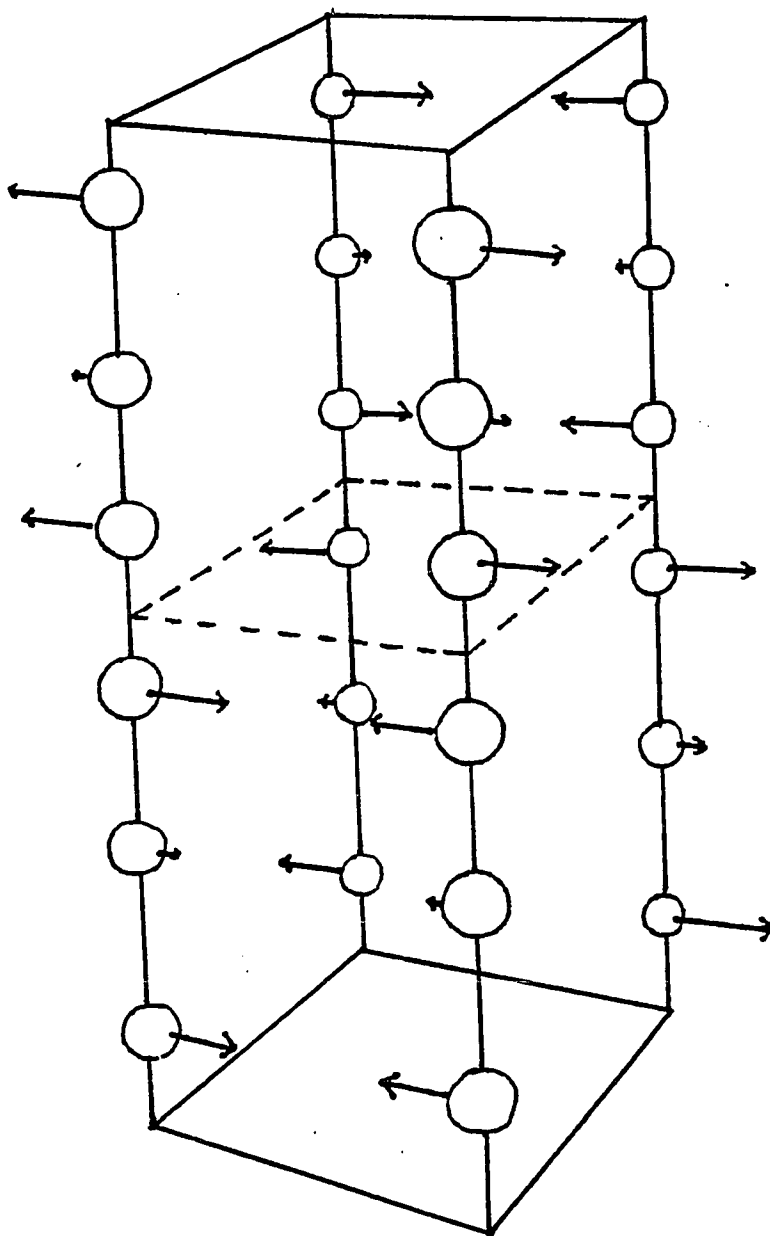
Figure 5.13. The magnetic sublattice structure for $PrBa_2Cu_3O_7$ for 0 K ≤ T ≤ 17 K, (T_{N2} = 17 K). The structure possesses a small magnetic moment in the CuO-chains, and has antiferromagnetic ordering between the rare-earth planes but ferromagnetic ordering within the planes.

frequency and/or a splitting of the signal, both of which are not observed in Pr1237.

We found that the TQ (a-axis ordering) model for $YBa_2Cu_3O_{6.35}$ and $YBa_2Cu_3O_{6.10}$ (Figs. 5.12 and 5.13)[89-91] is in full agreement with a downward shift in the frequency for the B2 site (see Fig. 5.3). An additional $\mu_{Cu(ch)}$ of 0.02 μ_B matches up the observed frequency below T_{N2}. This agrees well with the small value of $\mu_{Cu(ch)}$ proposed in the TQ model. This model exhibits ferromagnetic ordering within the Cu-O planes but has antiferromagnetic ordering between successive planes. A small moment appears in the Cu-Vacancy chains which we attribute to the small change in the magnetic field at the muon site. Because this site is closer, and dipole fields drop off by $\frac{1}{r^3}$, this small moment has a significant effect on the internal field at the muon site, with little change due to re-arrangement of spin direction for the Cu moments.

For the LY (b-axis ordering) model, this structure also causes a drop in the local field at the B2 μ^+-stop site. By applying b-axis ordering, the frequency drops an order of magnitude too large to account for the observed frequency below T_{N2}. Although we did see some evidence for the Lin structure in the Y123(6+δ) samples ($\delta \approx 0.2$), we did not observe any evidence for this structure in the Pr samples--the fields were much too large to match the magnetic field seen at the μ^+ site. Nevertheless, it would appear that the Y123(6+δ) system has a complex oxygen dependence (δ) in the magnetic ordering which occurs at low temperature.[129-130]

As mentioned above, we cannot account for the frequency at T_{N2} only by vectorially adding the magnetically ordered Pr moments, neither c nor a or b axis ordering, and neither in ferromagnetic nor in antiferromagnetic orientations Pr may order simultaneously with a change in the copper magnetic structure, as has been suggested by recent band-structure calculations.[125] If we have simultaneous ordering of the chains in the LY model and Pr ordering along the c axis, we predict for the B2 site two frequencies due to the symmetry of such a magnetic structure. On the other hand, the TQ structure with Pr ordering only yields one signal at the B2 site. Although the signals broaden somewhat below T_{N2}, we definitely do not observe two signals. Therefore, simultaneous ordering of Pr (c and a axis) and chain ordering in only possible in conjunction within the TQ model.

Presently, we argue that the Pr1237 exhibits a phase change in the Cu magnetism below T_{N2}, and that the Pr either orders at a lower temperature (possibly at T_{N3}), or Pr orders in conjunction with the Cu magnetism. Since the Pr doped Y123y can behave like the R1236 systems, a similar mechanism can be invoked, namely, the removal of holes from the Cu-O planes.[114,127] Furthermore, in rare-earth compounds, typical ordering temperatures[66-69] are around 2 K. Although the crystal field splitting could lead to band overlap and possible itinerant exchange, a Néel temperature of 15 - 20 K is still unlikely. Qualitatively, the change in muon frequency is small at this phase transition and the temperature range for the transition is relatively small (roughly 3 K). This suggests that there is only a minor change in the magnetic structure. A major change in the

direction of the field (due to Pr ordering) would be likely to bring about a major change in the observed muon frequency spectrum.

We conclude that, unless the Cu-Pr magnetic structure is anomalous for Pr1237, the only source of the downward frequency shift is from copper chain ordering in either the LY or the TQ modeling, or the shift is due to simultaneous ordering of Pr and Cu chain in the TQ model. Although NMR/NQR measurements[126-127] do not show any indications for Cu chain ordering down to 1.4 K, we cannot explain our μSR data without such Cu chain magnetism. Our study indicates a $\mu_{Cu(ch)}$ of 0.02 μ_B, which is below the detection limit[128] of 0.03 μ_B. A moment of 0.02 μ_B in the chains is enough to shift the muon frequency from 2.3 to 1.9 MHz for $\mu_{Cu(pl)}$ of 0.272 μ_B. This result indicates again a great sensitivity of μSR to detect minute changes in the magnetic structure of these R123y materials.

5.8. $PrBa_2(Cu_{1-z}Al_z)_3O_7$ (z = 0.08)

The presence of the site-preferential impurities is often helpful in elucidating the physical origin of a phase transition. Aluminum has been known to preferentially (about 85%) occupy the Cu chain site in Y1237.[131-134] In Pr1237, the Al dopant would have the propensity to dilute any long-range chain ordering. Therefore, if chain ordering is the source of T_{N2} in pure Pr1237, then doping the chains with a magnetic vacancy will suppress T_{N2} and should dilute the long-range order at the Cu chain sites. Then, the muon frequency should not shift significantly from the extrapolated magnetization curve above T_{N2}. If, on the other hand, the Pr orders at T_{N2}, we

should see a similar muon frequency shift observed for Pr1237. In this case, the dominant source of the relatively high T_{N2} is assumed to be due to the large crystal-field splitting of Pr. Magnetic susceptibility and heat-capacity measurements show magnetic ordering of $(PrAl_{.24})1237$ beginning at T_{N1} (~ 280 K) and an anomaly at T_{N2} of 14.5 K suggesting a phase transition similar to that of Pr1237.

In the μSR data, we have observed two frequencies (extrapolated to 0 K) above and below T_{N2}: 2.1 and about 0.3 MHz. We attribute the 2.1 MHz signal to the B2 site and the 0.3 MHz signal to the B2 μ-stop sites having an Al ion replace the nearest Cu-plane site. At the B2 site, magnetic dipole calculations predict a value of 0.3 MHz for a Cu(2) magnetic vacancy. Both signals show large broadening in the Fourier transform. The source of broadening is likely the disorder in the chain moments which broadens the field distribution at the B2 sites. Typical relaxation rates for $(PrAl_{.24})1237$ are on the order of 2.0 μs^{-1} for the 2.1 MHz signal. In pure Pr1237, this signal has a typical Gaussian relaxation rate of 1.0 μs^{-1}. Again, this indicates a larger distribution of fields for $(PrAl_{.24})1237$ than for Pr1237. These Al-doped Pr1237 μSR data also suggest the Cu chain ordering is likely the source of the μ^{+} frequency shift below T_{N2} and that Pr ordering may only occur in combination with Cu chain ordering.

5.9. Summary

The candidate muon-stop sites for $Pr_xY_{1-x}Ba_2Cu_3O_{6+\delta}$ ($0.6 < x < 1.0$, $0 < \delta < 1$) are located in about the same regions as the other $RBa_2Cu_3O_{6+\delta}$ ($0 < \delta < 1$) sites. Antiferromagnetic ordering of the Cu moments occurs below 280 K. We predict that for Pr1237, the magnetic moments of the Cu for $T_{N2} < T < T_{N1}$ is 0.27 μ_B and directed along the a axis. For Pr1236, the magnetic moment of the Cu is 0.5 μ_B with the same kind of ordering as Pr1237.

The Tranquada model for $RBa_2Cu_3O_{6+\delta}$ ($0.0 < \delta < 0.4$) is the most suitable for describing the frequency shift in the μSR spectrum at $T < T_{N2}$. Additional reduced Pr magnetism may only be considered in conjunction with $\mu_{Cu(ch)}$ magnetism; Pr magnetism alone predicts an increase, not a decrease, at T_{N2} in the observed muon frequency for Pr1237. No definite frequency anomaly at T_{N2} has been observed in Pr1236 and Al-doped Pr1237.

Chapter 6

Zero-Field μSR on Hydrogen Doped $YBa_2Cu_3O_7$

6.1. Introduction

The primary focus of doping studies in high-T_c superconductors has been on the effects that result from lattice-site substitutions. Another equally informative doping involves adding new sites to the interstitial regions of the lattice by inserting small dopant ions such as the hydrogen ion or the muon. As long as the fundamental crystal structure is maintained, one observes how interstitial doping affects the overall physical properties of the material leaving the original spatial orientation of the atoms virtually undisturbed. While doping the lattice sites yields valuable information about the origin of various physical properties in the crystal, the doping can introduce chemical bonding effects not associated with the original material. On the other hand, interstitial doping leaves the structural orientations nearly intact. The resulting effects are found in the type of bonding which forms as a result of the broken bonds in the undoped material.

Interstitial doping helps elucidate the physical origin of important conduction properties in novel metals and semimetals, and can contribute information about major electronic properties such as magnetism and superconductivity. Hydrogen doping often poisons the superconducting properties of semimetals such as graphite

intercolated compounds,[135] and most recently--the $RBa_2Cu_3O_{6+\delta}$ ($0 \leq \delta \leq 1$) system. If the position of the hydrogen substituents can be determined, then interpretations can be made about the origin of the conduction properties of the material, based upon the observed physical properties.

For example, in graphite, the conduction properties are attributed to the large sheets of hexagonally arranged carbon atoms. When hydrogen is added to graphite, the hydrogen will tend to bond to the carbon between the hexagonal sheets. The bond that forms destroys the conduction properties of the graphite.[136-137] The conduction properties of graphite are qualitatively similar to aromaticity in the smaller analogues such as benzene. The hydrogenation of the benzene ring is unfavorable because of the loss of aromaticity in the bond. The original sp^2 bond is converted to an sp^3 bond destroying the delocalized nature of the electrons in the aromatic ring structure. However, when the benzene like structure is extended out to larger structures (i.e., graphite), then the number of possible microstates extends into a band and so the H^+ is able to capture electrons: thus destroying the conduction properties of the material.

If the oxide superconductors lose their conductivity due to the doping in the lattice with hydrogen, then the way in which the hydrogen localizes in the R123y lattice will strongly influence the resulting physical properties.

6.2. The Physical Properties of Y1237
as a Function of H Concentration.

In this chapter we introduce the variable x to denote the concentration of dopant per formula unit of $RBa_2Cu_3O_y$. Therefore, $H_xYBa_2Cu_3O_y$ (x = 1, y = 7) is $H_1YBa_2Cu_3O_7$, which will be denote in the short form H_1Y1237. Similarly, $H_xYBa_2Cu_3O_y$ (x = .2, y = 6.9) is $H_{.2}YBa_2Cu_3O_{6.9}$, which will be denoted in the short form $H_{.2}Y123(6.9)$.

The experimental results for the physical properties of H_xY1237 (0 ≤ x ≤ 5) tend to have some notable variations in the literature sources. Since the discovery of the high-T_c superconductors, the fabrication of Y1237 has been studied in detail and standardized manufacturing procedures have been established. With these considerations in mind, the more reliable experimental results should be attributed to the more recent publications. Indeed, publications between late 1988 and 1991 show increasingly more consistent physical results.[18-20,141,142] We present a sampling of a number of experimental results from several authors in major journals, including the early data from Reilly et al. (ref. 138) and Fujii et al. (ref. 140) (circa, late 1987).*

---

* The following journal articles and their respective publication dates are used in this section:

138)	(1987 Oct.) J. Reilly, et al.
139)	(1988 Feb.) M. Nicolas, et al.
140)	(1988 April) H. Fujii, et al.
141)	(1989) I. Natkaniec, et al.
142)	(1989) S. Goren, et al.
18-20)	(1989 Dec.) Ch. Niedermayer, et al. and H. Glückler, et al.

All of the authors[18-20,138-145] in this survey agree that the samples remain superconducting for small concentrations of H in $H_xYBa_2Cu_3O_7$ (x < 0.5).

The transition between superconducting and non-superconducting is rather unclear in these samples. Early reports (Reilly *et al.*)[138] claimed to have superconductivity up to x = 4, whereas others[140] claimed that the sample lost the $YBa_2Cu_3O_7$ crystal structure when x > 2. More recent papers indicate that the materials are semiconductors above x = 0.5 and can be doped up to x = 2.5.[18-20]

The measured lattice constant for the c axis (with respect to x, the H dopant) is also disputed. Reilly *et al.*[138] claims that the c lattice parameter increase where Fujii *et al.*[140] claims the opposite. Both authors do agree that the b lattice constant remains relatively constant and the a lattice constant increases slightly as a function of x.

Many reports claim an increase in T_c for small quantities of x.[18-20,138,140] On the other hand, others[139,143] claim no connection. Nicholas *et al.* note that this change in T_c is "correlated with an increase in the contact resistance," there is a substantial reduction in the Meissner fraction for increasing quantities of H, and Nicholas *et al.* observe no connection between the resistivity $\rho(T,x)$ and the transition temperature $T_c(x)$ (where x is the concentration of H dopant).[139]

At low concentrations of H (0.00 < x < 0.13) the samples of H_xY1237 remain superconducting with only a small observable change in the superconducting transition temperature (T_c) and the superconducting volume fraction. At higher concentrations of H,

(x > 0.13), the sample begins to lose its superconducting properties and takes on properties of an insulator with some local magnetic ordering. The superconducting volume fraction decreases with increasing concentration of H (0.0 < x < 0.5).

The hydrogen dopant appears to induce magnetic ordering in the Y123y system (x > 0.5). The behavior is similar to what is observed for $RBa_2Cu_3O_{7-x}$--R123(7-x)--when oxygen is removed from the sample forming R1236, and also $(Pr_xY_{1-x})Ba_2Cu_3O_{7-\delta}$ (0 < x < 1, δ = 1).[21-23,107-109,113] In effect, the hydrogen is behaving like an electron trap. A phase diagram of the H_xY1237 of x versus T_c, or T_N is nearly identical to the phase diagrams for the Y1236 structures, and the doped $(Pr_xY_{1-x})Ba_2Cu_3O_{7-\delta}$ structures. Only the value for T_c and T_N are seen to shift between these materials. A picture of the phase diagram of $(Pr_xY_{1-x})Ba_2Cu_3O_{7-\delta}$ (0.0 < x < 1.0: $\delta \approx 0$) is given in Figure 5.1; similar phase diagrams can be found in the literature for $YBa_2Cu_3O_{7-x}$ (0.0 < x < 1.0).[137]

6.3. The Behavior of the Muon in R123y

From numerous experiments performed on R1236 structures (R = Gd, Ho, Er, *etc.*), we have concluded that the muon most likely oc-cupies the Balmer(2) site (B2) (refer to Fig. 6.1 for the site locations). We cite the following evidence to support this.

First, for Gd1237, discussed in chapter three, a 7.0 MHz signal and a 5 MHz signal are seen and were assigned as the B2 and the B1 sites, respectively--Gd has antiferromagnetic c axis ordering.[14]
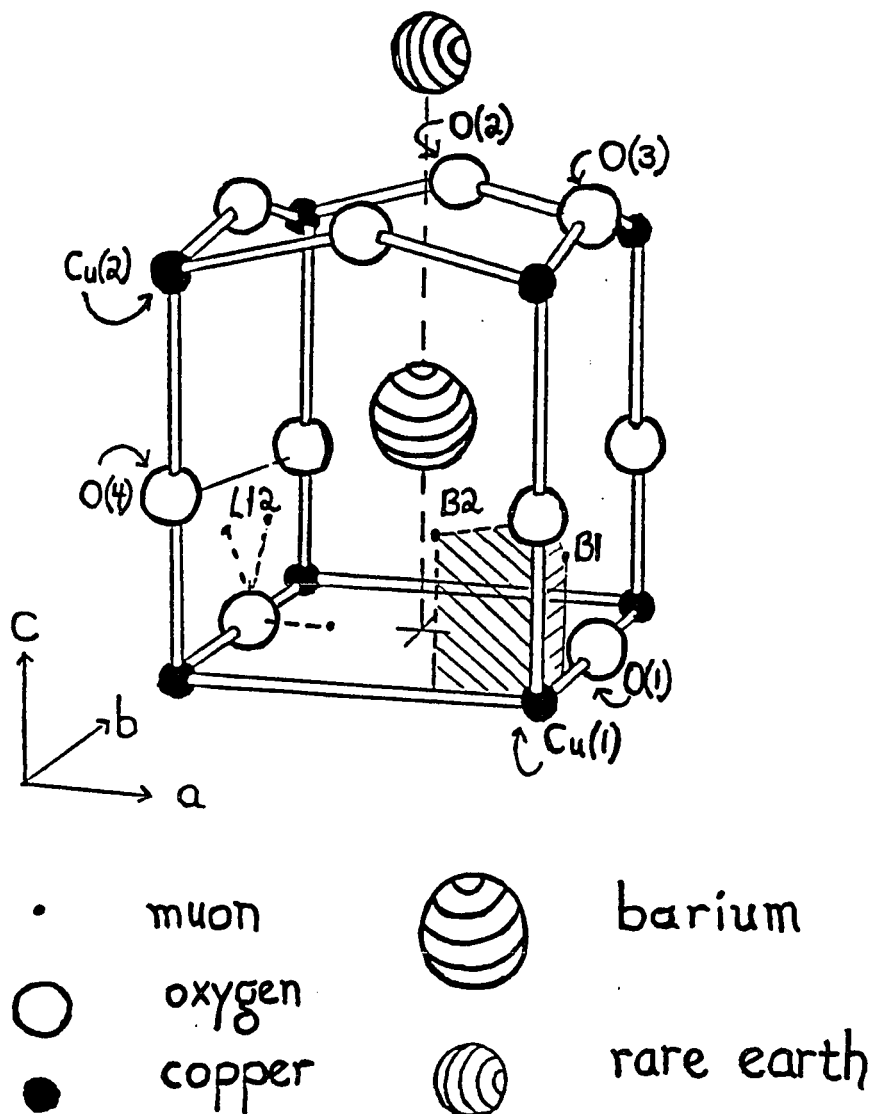
Figure 6.1. The location of the muon sites for $RBa_2Cu_3O_7$ (R = Dy, Eu, Er, Gd, Ho, Pr, Y, Y_xPr_{1-x}) based upon the magnetic-dipole-field calculations and potential-energy calculations. The Balmer(2) site (B2) appears in all of the $RBa_2Cu_3O_y$ structures so far investigated. These muon sites are also found to be the proton sites in this chapter.

Second, for Y1236, a 4.2 MHz signal is observed which is most likely the Balmer(2) site--Cu has an antiferromagnetic a axis ordering.[15]

Third, for Er1236 and Pr1236, discussed in chapters three and four, respectively, symmetry considerations must be taken into account for the B2 site. Because of the tetragonal symmetry of the R1236 structure, evidence of electronically equivalent sites for the B2 location must be seen. However, even though the sites are electronically equivalent, they are not magnetically equivalent. Therefore, there are two μSR signals of roughly equal occupation but with differing frequencies and relaxation rates--a 4 MHz signal (corresponding to the B2 site) and a 2 MHz signal (corresponding to the B2p site).[16,17]

Fourth, for $PrBa_2(Cu_{3-z}Al_z)O_7$ (z = 0.08), two signals (0.3 and 4.2 MHz) are observed. The 4.2 MHz signal corresponds to the Cu(2) moment (0.5 μ_B) in the CuO planes. The 0.3 MHz signal corresponds to the absence of that same moment in the CuO planes due to substitution from the Al.[17,131-134]

The evidence strongly indicates that our proposed B2 site is indeed the most probable site where the muon localizes in this R123y oxides. Therefore, it seems likely that the μ^+-stop site in H_xY1237 should also be the B2 site for small concentrations of H dopant (x < 1.0).

6.4. Hydrogen localization in $H_xYBa_2Cu_3O_7$

Based upon the location of the μ^+-stop sites in R123y, we are in a position to state the following: the muon occupies the B1 and B2 sites in $H_xYBa_2Cu_3O_7$.

The μSR data for H_xY1237 was obtained at the Paul Scherrer Institute (PSI). Two μSR signals are seen in H_xY1237 ($x \geq 0.5$) with saturation frequencies 4.2 MHz and 1.9 MHz (extrapolated to zero Kelvin--Figs. 6.2 and 6.3) . The 4.2 MHz signal in H_xY1237 is close to the 4.5 MHz signal seen in Y1236. As the concentration of H increases ($x > 0.5$), the 4.2 MHz signal disappears and the 1.9 MHz signal increases in intensity. This suggests that the muon is localizing at the same place as in Y1236 and that the magnetic structure is very similar.[18-20]

The origin of the 4.2 MHz signal is the B2 site. We deduce this because the μSR signal seen in Y1236 (4.5 MHz) is also seen in H_xY1237.[18-20] The intensity of the 4 MHz signal drops off rapidly as a function of the H concentration. In the place of the 4.2 MHz signal, the 1.9 MHz signal grows in intensity. The data suggests that the H^+ is occupying the sites where the μ^+ goes (B2) and, as the concentration of H^+ increases in the Y1237, the μ^+ is forced to occupy a different site.

The origin of the 1.9 MHz signal is the B1 site according to the frequency of the signal. The B1 site was first observed in Gd1237 with a low asymmetry (A_s).[14] The site is similar to the B2p site in the R1236 system--the symmetrical site with B2.[14] The site appears to become favorable only after a large fraction of B2 sites are occu-
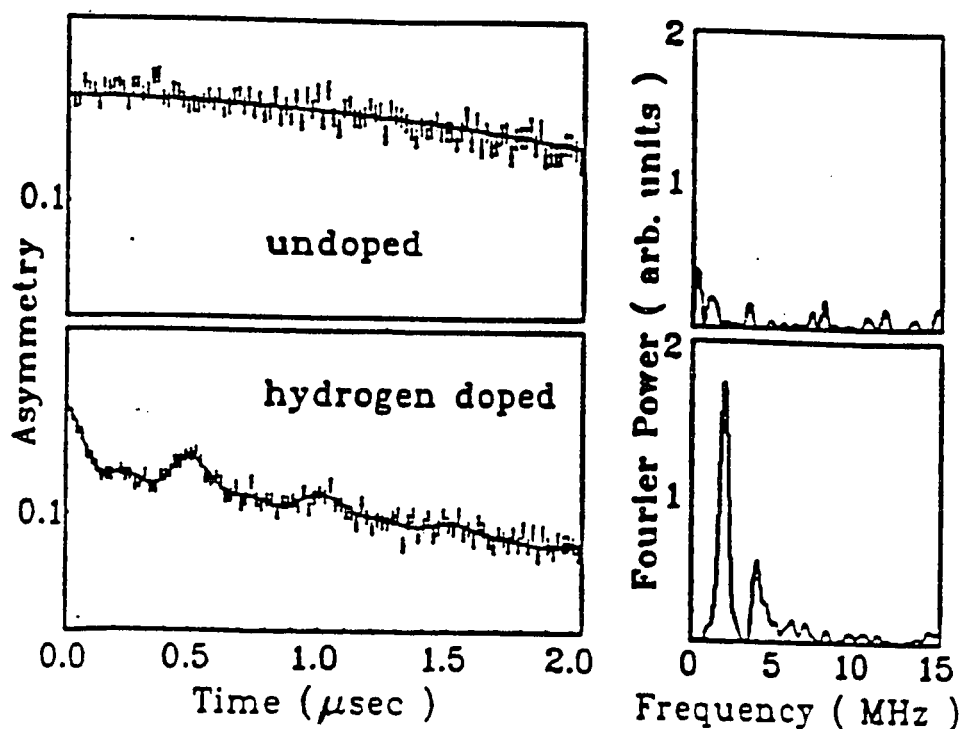
Figure 6.2. The μSR spectra and the corresponding Fourier transforms for two samples of $H_x YBa_2Cu_3O_7$. The top data corresponds to the undoped $YBa_2Cu_3O_7$ (¡superconducting!). No distinct frequency is seen in the μSR spectrum (as one would expect for a superconductor). The bottom data corresponds to $H_1YBa_2Cu_3O_7$ (¡non-superconducting!). The clear indications of a distinct frequency is seen in the μSR spectrum--clear indications of magnetic ordering. The data and graph are taken from Ch. Niedermeyer et al., Phys. Rev. B 40(16), 11386 (1989)--references 18 - 20.
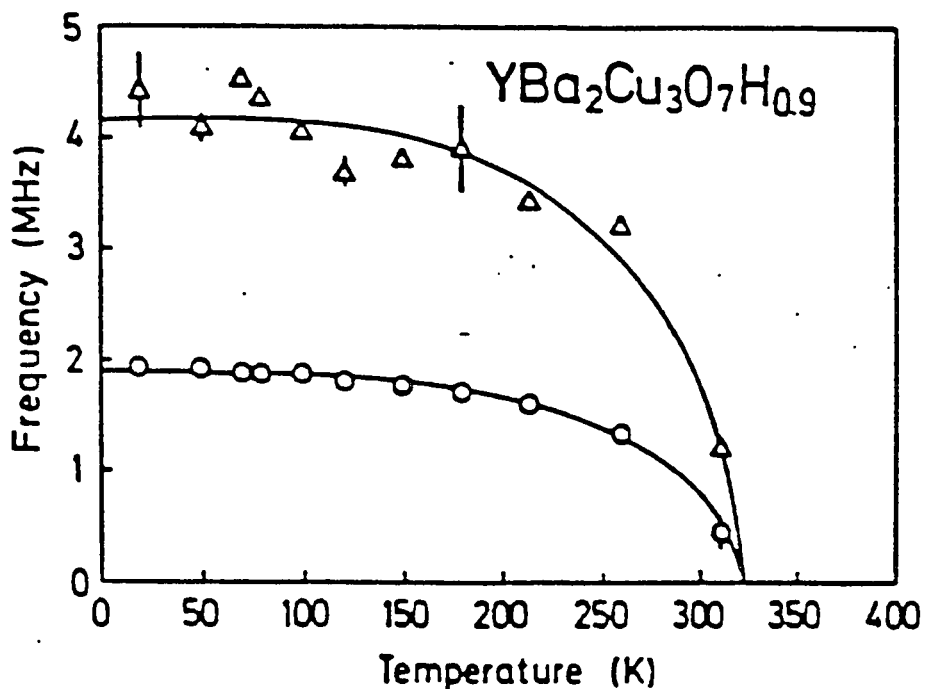
Figure 6.3. The Temperature dependence of the μSR frequencies in $H_xYBa_2Cu_3O_7$ (x > 0.5). The Néel temperature of the sample is approximately 320 K. Since the μSR frequency is proportional to the magnitude of the local magnetic field, the data represents the magnetization curve for a sample. Two distinct frequencies are visible in the spectrum: a 1.9 MHz signal (attributed to the B1 site), and a 4.2 MHz signal (attributed to the B2 site). The data and graph are taken from Ch. Niedermeyer et al., Phys. Rev. B **40**(16), 11386 (1989)--references 18 - 20.

pied by H ions in H_xY1237. We can only surmise that the H dependence on the origin of the shift in intensity of the μSR signal from 4.2 MHz (B2 site) to the 1.9 MHz (B1 site) is due to hydrogen occupation of the B2 site.[18-20]

One alternative site location for the H was discussed by Yang *et al.*[143] In this model, the H bonds to the Cu forming a CuH bond. The supporting evidence in the paper is based upon IR absorption measurements which were made on H_xY1237. The IR absorption peaks, which were attributed to H, were reported to be 1467 cm^{-1} (bond stretching) and 841 cm^{-1} (bond bending). The evidence from this paper would suggest CuH bonding. However, in the μSR experiments,[18-20] CuH bonding is not a likely explanation for the behavior of the μSR signals seen for concentrations of H in the range of 0 < x < 1. We should not see any H dependence on the asymmetry of the μSR signal for the 4.2 and 1.9 MHz signals if the H is bonding to the Cu. Instead, there appears to be competition for the same sites. Owing to the current evidence, it would appear that the hydrogen does not form a CuH bond. Although there is no observed 3200 cm^{-1} OH$^-$ signal from the IR spectroscopy (Yang *et al.*), we cannot explain the observed μ^+ behavior on the basis of Cu-site bonding.

A third location for the H was discussed by Fujii *et al.*[140] (Fig. 6.4). In this model, the hydrogen occupies the symmetrical site of the R1237 structure. This proposed site is rather improbable based upon the proposed CuH bonding[143] because the bond is too long (greater than 1.7 Å) for a normal hydride bond (~ 1.5 Å). Furthermore, there is no reasonable explanation for the shift in the 4.2 MHz
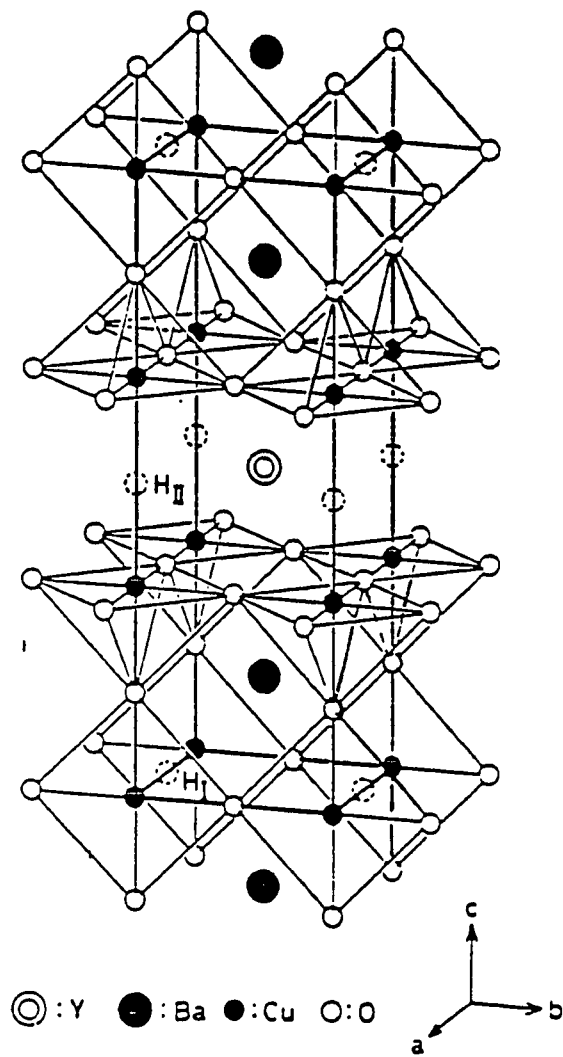
Figure 6.4. Proposed location of the hydrogen sites for $H_x YBa_2Cu_3O_7$ according to H. Fujii *et al.* Although this structure is a possible alternative, it does not explain the cause of the asymmetry shift in the muon spectrum. From H. Fujii *et al.*, Japanese Journal of Applied Physics **27**(4) (1988) L525. (Reference 140.)

and the 1.9 MHz signal using the symmetrical sites and CuO bonding as proposed by Fujii *et al.*[140]

6.5. Discussion

We can now make certain interpretations about the properties of $H_x Y1237$ based upon our knowledge of the μ^+ in R123y samples: (i) the H^+ occupies the same sites as the μ^+; (ii) the magnetic structure of $H_x Y1237$ is similar to that seen in Y1236 structures; (iii) the behavior of muons in H-doped Y1237 is similar to the behavior of muons in typical R1237 structures.

Both Reilly *et al.*[138] and Fujii *et al.*[140] agree that the b lattice parameter does not change. Reilly *et al.* suggest that the "hydrogen occupies sites which leave the Cu-O chains intact along the b axis which [has been presumed necessary] for the superconducting transition to occur." This evidence indicates that the H does not insert itself in the lattice with a bond forming along the y axis (otherwise the b lattice spacing should change). This limits the bond axis to the x and z axes since these axes exhibit the change in lattice parameters. The evidence is in strong support of the B2 site because this site exhibits x and z components.

The shift in the c axis is suggestive of the formation of an sp^3 bond by the H. The change in cell volume along the c axis is likely an indication of a bond breaking

$$Cu(1) -- O -- Cu(2) \quad + \quad H^+ \quad \text{------->}$$
$$Cu(1)^+ \quad + \quad HO -- Cu(2).$$
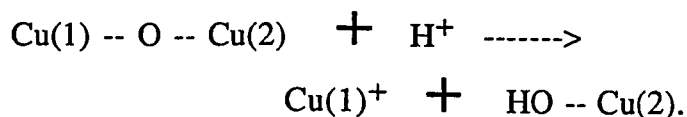
The H forms an OH^- complex. Depending on the nature of the resulting bond, there is the possibility of shrinkage along the c axis (due to the O--Cu(2) bond shrinkage, as a result of the stronger overlap of wave functions) or there is the possibility of expansion (due to the breakage of the Cu(1)--O bond and subsequent ionic repulsion of the respective ions). Therefore, the mere presence of a shift in the c axis hints toward the presence of the B2 site as a result of the suggested tetrahedral bond formation.

In a recent paper on proton NMR absorption in $H_{.11}Y1237$ (superconducting),[142] Goren et al. found a doublet in the signal using a 300 MHz field NMR spectrometer (Fig. 5.5). Goren et al.[142] also found a negative shift of 14 ppm relative to benzene. In organic NMR analysis, the value of δ (in ppm) is defined as

$$\delta = (H_{ref} - H_{sample})/H_{standard} \times 10^6 \text{ (ppm)}.$$

where δ is a frequency independent value, H_{ref} is the resonant frequency of a *reference* material (in this case benzene), and H_{sample} is the resonant frequency of the sample in question. (See Appendix A for more details.) Here, δ is used to indicate the relative shift independent of the applied magnetic field. More will be discussed on the latter remark in chapter seven.
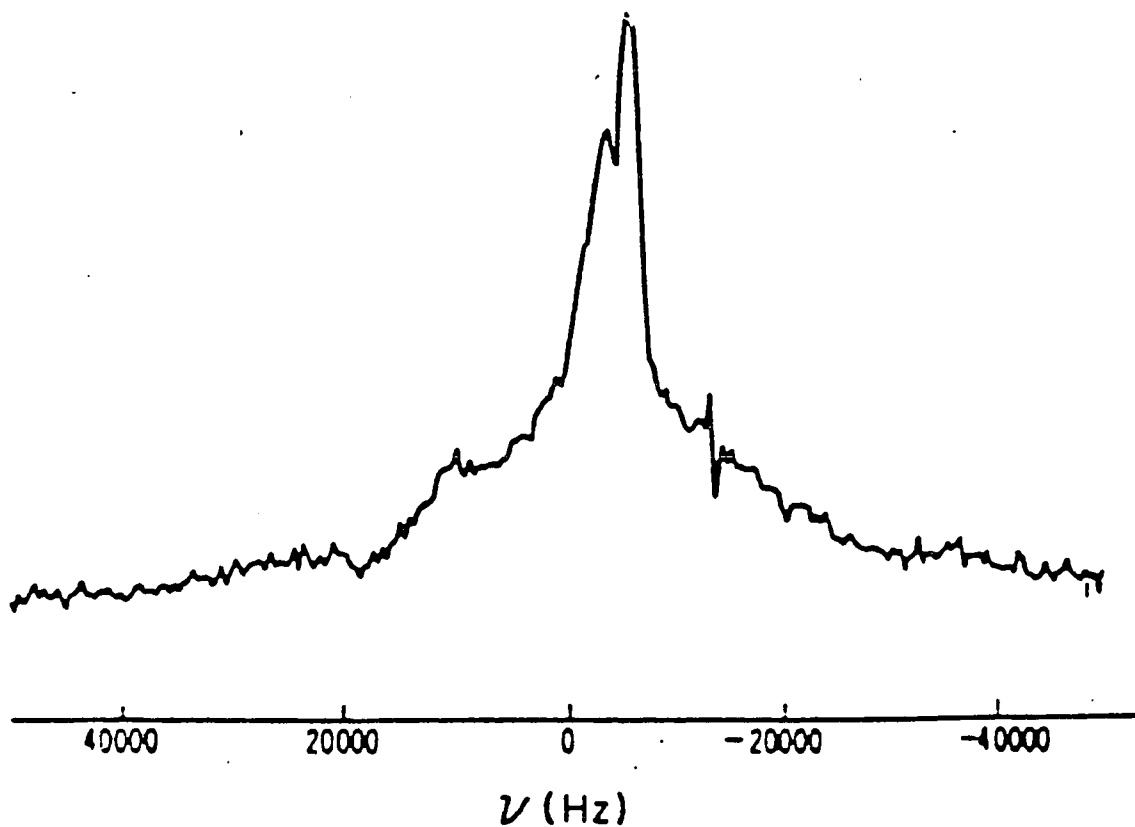
Figure 6.5. Absorption lines for and NMR spectrum of H in
$H_{.11}YBa_2Cu_3O_7$ using a 300 MHz NMR spectrometer. There is clear
evidence of a doublet in the spectrum indicating the presence of two
different fields at the proton site. The data is from S. D. Goren *et al.*,
Solid State Communications **70** (1989) 279. (Reference 142.)

The doublet in the NMR spectrum suggests the presence of two different fields at equivalent proton sites.

One suggested source of the doublet is the result of protons located in both the normal and the superconducting regions. The superconducting regions would see a reduced field due to shielding from the planes and the normal regions would see an enhanced field due to deshielding (see Appendix A). If this is so, then the corresponding expelled flux is less than 1% for samples of $H_{.11}Y1237$ measured by Goren *et al.*[142] (The line width was found to be 30 kHz in a 43.6 MHz spectrometer.) The nature of the local field in $H_{.11}Y1237$ would also suggest an estimated current density on the order of 10^9 A/cm^2, a factor of ten smaller than the current density estimated on the basis of spin fluctuations of the rare-earth moments in Gd1237.[81,82,147] The extremely low value of the expelled flux may suggest strong flux pinning in the hydrogen doped samples, similar to the behavior of the Eu1237 samples measured at LAMPF.[82] The expelled flux is a factor of ten smaller than what is seen for samples of Gd1237 suggesting a correlation between the current density and the expelled field. In any case, the splitting can be correlated with the expected local behavior at the B2 site and is consistent with the μ^+ behavior as seen at the muon-stop site.

Another possible source of the doublet is the presence of weak antiferromagnetism in the Cu moments, as seen at equivalent proton sites in the sample. The presence of magnetism and superconductivity in the high-T_c materials is a perplexing and curious phenomenon. The presence of antiferromagnetism would generate a doublet in the spectrum at the B2 site as a result of the orientation of the
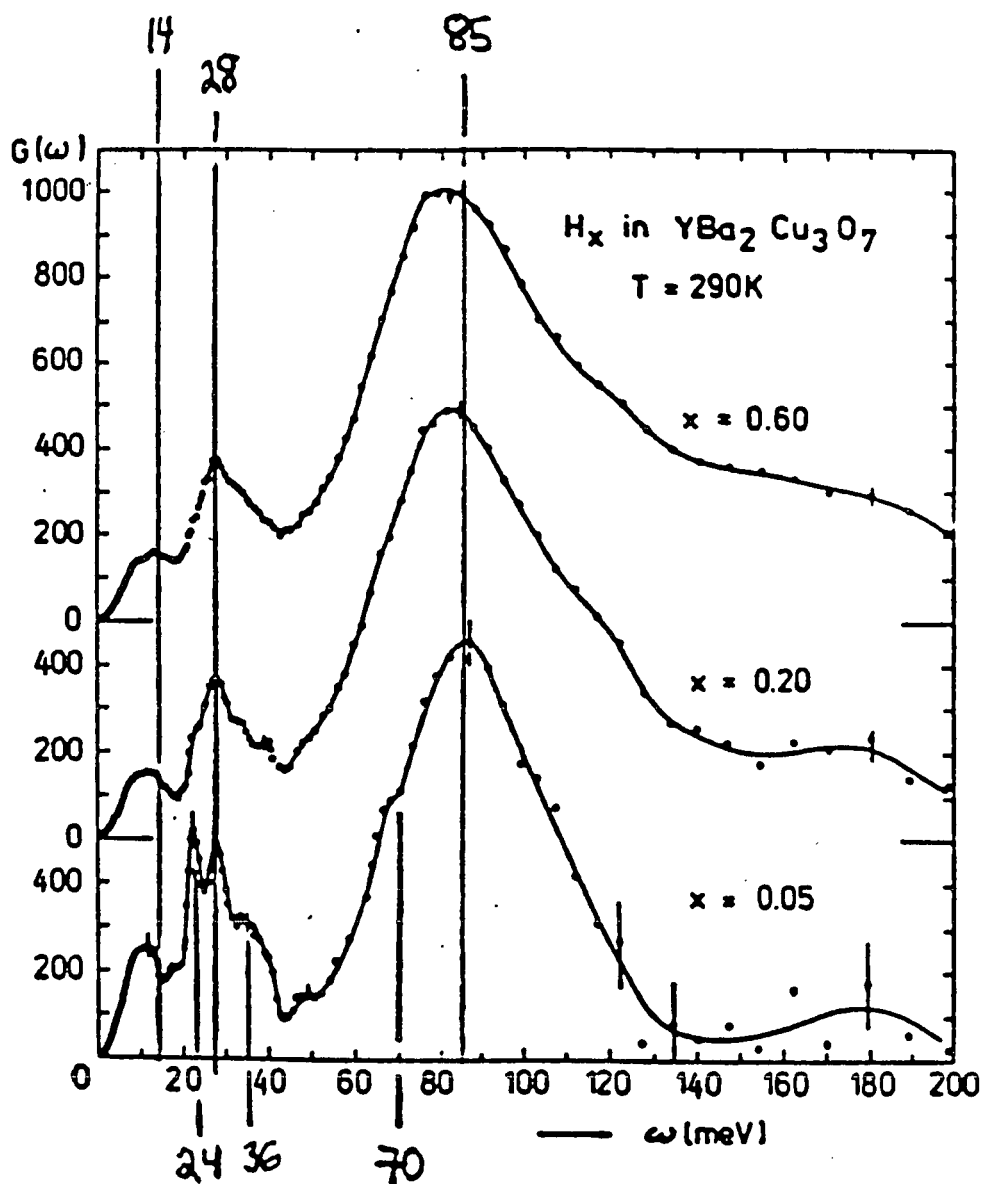
Figure 6.6. Density of states for the amplitude of hydrogen vibration in $H_xYBa_2Cu_3O_{6.95}$ when x = 0.05, 0.20, and 0.60. The magnitude of the energy distribution was normalized to 1000 for comparison purposes. The 24, 36, and 70 meV signals correspond to Y and Cu-O vibrations. As the concentration of H increases, these vibrations broaden and disappear. Data taken from I. Natkaniec *et al.*, Physica C 162-164 (1989) 1369. (Reference 141.)

local field relative to the external field. Although the idea is intriguing, the principal region where magnetism and superconductivity are observed (using μSR) is in the phase diagrams for samples which have a hole concentration associated with $x = 0.5$. (The value of x can be applied to H_xY1237, (Pr_xY_{1-x})1237, and Y123(7-x), as noted earlier.) Furthermore, within this region, the properties appear to be spin-glass-like rather than antiferromagnetic-like. However, the possibility should not be discounted since some of the suggested mechanisms driving superconductivity are based upon magnetic frustration.[148-152] The small field would be attributed to precursor effects. The corresponding local field for the muon would be ~ 0.1 MHz (7 Oe), a value which is too small to measure against the background decay events on the LAMPF-μSR spectrometer without extremely large statistics (say 1 billion counts--about 8 months of data!).

The shift (~ 15 kHz--in a 300 MHz applied field) is much smaller than that usually encountered at the hydrogen site in an AF material (~10 MHz). For a proton site in a sample of $YBa_2Cu_3O_{6.2}$ which had absorbed water, the internal field was measured to be about 600 kHz (extrapolated to 0 K), corresponding to about 0.15 kOe.[146] This local field would correspond to a μ^+ signal of 2 MHz--the value seen in (Pr_xY_{1-x})1237 as discussed in chapter five. For this signal, we suggest that the B2 site is still the proton-stop site. However, the nature of the bonding is such that we see the effects of AF ordering of the Cu moments, and hole filling behavior similar to (Pr_xY_{1-x})1237.

Inelastic neutron scattering (INS) measurements[141] indicate a loss of structural features when R123y is doped with H (24, 36, and 70 meV peaks--Fig. 6.6). Essentially, the modes broaden as the concentration of H increases. The effect was attributed to the occupation of the H_{II} sites (Fujii et $al.$[140]--Fig. 6.4). However, since we know that the nature of the HO⁻ bond is tetrahedral, the mode broadening could also be attributed to the disruption of the bonds between the Cu(2)-O-Cu(1) complex as a consequence of the formation of the tetrahedral $Cu(2)-OH^+$ bond, analogous to the $Cu(2)-O\mu^+$ bond discussed in the previous two chapters.

The INS data[141] indicates a possible reduction in Cu valence but the source of the valence change is not necessarily due to the presence of a hydride ion, the valence change could also be an electron donated from the oxygen, due to the subtle changes in the electronic structure of the R1237 lattice. In addition, small changes in the a and c lattice constants can also induce small changes in the electronic structure.

In this discussion, the most difficult question to resolve is the interpretation of the IR data from Yang et $al.$[143] The 1470 cm⁻¹ signal is acceptable for OH⁻ bending mode--$\delta(OH)$; however, there should also be evidence of 3600 cm⁻¹ stretching mode--$v(OH)$. Although the evidence presented in the paper would strongly indicate the presence of a CuH bond, we suspect that there may be other explanations which could be invoked. First, it may be possible that the H forms a CuH bond for large concentrations of H--as was suggested in the results of recent SCF-HF calculations.[64,65] The new IR mode may be the result of a change in the electronic structure
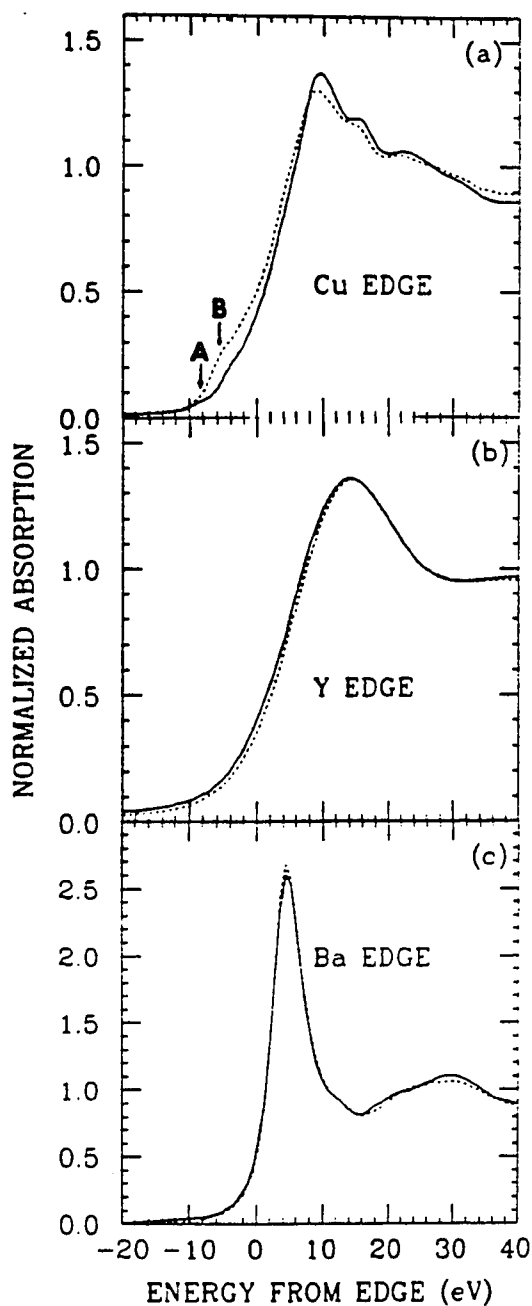
Figure 6.7. X-ray absorption spectra of samples of $YBa_2Cu_3O_7$ (solid line) and $H_{1.0}YBa_2Cu_3O_7$ (dashed line) at the Cu K edge (Fig. 7a), at the Y K edge (Fig. 7b), and the Ba L_{III} edge (Fig. 7c). The zero value of the energy has been arbitrarily selected to be half the height of the main peak. The data and graph are taken from Yang et al., Phys. Rev. B **36**(16), 8798 (1987)--reference 143.
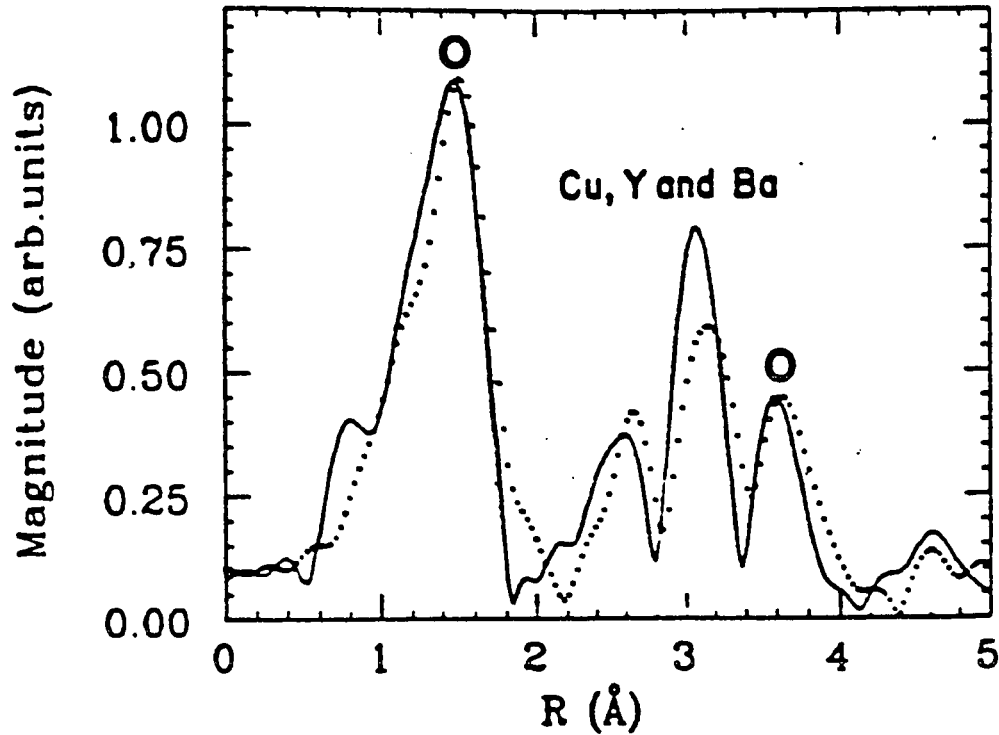
Figure 6.8. The Fourier transforms of the magnitudes at the Cu K edge. The FT for the $YYBa_2Cu_3O_y$ is the solid line, and the FT for the H is the dashed line. The transforms of k^2-EXAFS are taken over a range 2.6 - 14.6 $Å^{-1}$. The assignment of each peak is based on the neutron-scattering-derived structure. The data and graph are taken from Yang et al., Phys. Rev. B 36(16), 8798 (1987)--reference 143.

from a metal to an insulator--changing the bonding nature of the atoms. Second, in significant concentrations of H, the electronic structure of R123y may be altered enough so that R123y may not remain the same chemical structure. Third, it should be noted that this paper appeared early in the history of high-T_c material (the research work precedes 1988). Therefore, the quality of the sample is somewhat in question.

In the x-ray data on H_xY1237 (Yang et al., Fig. 6.7),[143] the largest effects of hydrogen doping are seen on the CuK edge for the Cu(2) atom. The major features of this spectrum (Fig. 6.7) are the 1s-3d transition and the 1s-4p transition which are at the lowest energy of the band (-9 eV and -5 eV, respectively). In the Fourier transform of the CuK edge (Fig. 6.8), there are a number of changes in the structure between the Y123y and the H_xY123y. Although Yang et al. claim that there is no significant change between the CuO shells in the two systems, the structures surrounding those Cu shells appear to change in intensity and degree of complexity (Fig. 6.8).[143] The results of this data may indicate the presence of a hydride phase in the sample.

Niedermeyer et al.[18-20] mentioned that the integrated intensities (μ^+ asymmetry) for different concentrations of H are not linear with respect to x. For concentrations of H exceeding one formula unit of Y1237 ($1 < x < 5$), the intensity of the 1.9 MHz signal is relatively constant, indicating that much of the excess H is selecting a different site at which to localize for these higher concentrations. Yang et al. suggested that H_xY123y may undergo a phase precipitation into a hydride phase between $x = 0.48$ and

x = 1.00, the supporting x-ray data would tend to indicate a hydride phase. The sample that Yang *et al.* used may have formed a separate phase, a result of damage which occurred to the sample during processing. The H addition was much faster than comparable addition rates from other sources (*cf.* Refs. 18-20, 139 and 140).

Based upon the evidence which has been provided on the μSR measurements, the shift in the lattice constant, the NMR doublet, and the neutron diffraction band broadening, we conclude that the most likely location of the H^+-stop site is at the B2 site (the same same location as the μ^+). Furthermore, examining the IR data and x-ray data from Yang *et al.*, we suggest that the Y1237 structure was somehow altered during the fabrication process and so the resulting data is for the hydride phase of the sample. Therefore, we conclude that the muon exhibits similar behavior to the proton in the R1236 system. Such a result confirms our original assertion in chapter three, *vis.* the muon and the proton behave in a similar fashion in the transition metal oxides (the muon and the proton both bond to the oxygens). The consistency of these two results greatly enhances our chemical intuition about the fundamental behavior of charge light particles such as the muon (μ^+), the proton (H^+, or sometimes p^+), and the positron (e^+, or sometimes β^+) to name a few.

6.6. Summary

The hydrogen appears to behave in a similar fashion to the muon in the R123y system. Major evidence is that the muon competes for the same site as the H in the $H_x Y1237$ structure, and, as a result, the intensity of the muon signal (asymmetry) changes as a result of occupation of the B1 site. The NMR spectrum suggest that the H is seeing two different magnetic fields at the B2 site. The change in the lattice constant also suggest that the H^+ is occupying a site in the xz plane which would most easily be explained as the B2 site. Neutron diffraction data for $H_x Y1237$ can also be interpreted in terms of the B2 site. The IR data by Yang *et al.* appears to be the result of the formation of a hydride phase in the sample of Y1237. We conclude, therefore, that the H^+ occupies the same sites as the muon.

Chapter 7

Predictions on the Oxide Superconductors Based Upon the μSR Studies of $RBa_2Cu_3O_y$

7.1. Introduction

No thesis would be complete without an attempt to predict future results based upon the research performed. In this last chapter, before the conclusion, the more speculative interpretations of the research are presented. One should keep in mind that these are merely predictions, postulates which are stated with only a small amount of experimental evidence to support them. The ultimate outcome of future experimental work, which may be obtained many years after the completion of this work, will reflect the strengths (and/or the weaknesses) of this thesis.

The aim of this chapter is to point toward a likely mechanism to the high-temperature superconductivity. The mechanism is discussed from the viewpoint of μSR in the vortex state, and the characteristics of muon bonding itself. Although the μSR data does not *a priori* provide evidence for a mechanism, the effects of a particular mechanism should be observed in the μSR data.

For the sake of brevity, most of this chapter assumes a knowledgeable reader in solid state physics. The contents of this chapter would likely become the material for a Ph.D thesis if otherwise expanded upon to include the majority of readers who do not have the background for the diversity of mechanisms which have flooded the literature on high-T_c superconductivity. We therefore present

our interpretations of the μSR data in terms of a single proposed mechanism. Other possible mechanisms discussed in the literature will not be considered.

In the next section, we discuss the vortex structure in the superconducting state. Based upon the μSR data obtained at PSI and LAMPF, there are indications that the vortex structure of the super-conducting phase R123(6+δ) ($0.5 < δ < 1.0$) may not be characteristic of a typical type II superconductor.[81-83]

In the final section, we predict that the electronic structure of CuO superconductors possesses a mixed ionic-covalent electronic structure. The array of CuO planes functions as a covalently bonded structure and the Ba^{2+} and R^{3+} (R = rare earth) exist as ions which balance the net excess charge in the planes. This charge balancing of the CuO planes can therefore accommodate either an electron doping or a hole doping, depending on how the conduction band is filled. The resulting picture suggests a possible excitonic mechanism which is governed by forces of physical constraint. A simple analogy of this mechanism can be seen in the aromatic compounds like benzene.

7.2.   The Vortex State of High-T_c Superconductors

The Vortex state of the high-T_c superconducting oxides exhibits unusual properties for a typical class of type II superconductors. None of the samples measured at LAMPF expelled more than 7% of the external field. These samples include R1237 [R = Gd, Eu, Er, and Pr_xY_{1-x} (x < 0.55)] and samples of $Bi_2CaSr_2Cu_2O_8$ and $Tl_2Ca_2Ba_3Cu_3O_{10}$. In the R1237 samples,[21-23,81-83] for $T < T_c$, two distinct signals are

observed, one from the superconducting grains and one from the non-superconducting grain boundaries. The latter fraction is about 15%.

The muon frequency data provides information about the distribution of magnetic fields and the expelled flux within the superconducting material. The field in the normal regions is equal to the applied field (13.55 MHz in a 1 kOe applied field). The field in the superconducting regions should follow a distribution which is associated with the penetration depth of the sample.

For a typical type-II superconductor, the expelled flux should be on the order of 33%. As a result, a broad band of muon frequencies should extend out from roughly 8 MHz to 13.5 MHz in a 1 kOe applied field for a canonical type-II superconductor. A shift associated with the Meissner effect. Instead, what is seen is a field which shifts only a small amount. In Figure 2.5 (p. 15), there is a small shoulder next to the 13.4 MHz signal at roughly 13.2 MHz (1 kOe transverse applied field), which represents the field in the super-conducting regions of the sample of $(Pr_xY_{1-x})1237$. In samples of Gd1237, the shift is closer to 12.6 MHz for the same conditions.

Caution should be used in applying the two fluid model to these high temperature superconductors because the expelled flux, from the sample regions probed by the muon, is such a small fraction (~ 3-7%) when compared with values for canonical type-II superconductors (~30%).[24-28]

Because the B2 site is in the BaO planes, the rare-earth spins should be significantly reduced as a result of the response of the CuO-plane super currents. The results of this effect can be seen in

the relaxation rate of the muon at various temperatures. In samples of Gd1237, a 1/T dependence (in addition to the $(1-(\frac{T}{T_c})^4)$ dependence) is seen in the relaxation data *below* T_c, and a 1/T magnetic field dependence (paramagnetism) is seen *above* T_c. Because of the reduced dependence of the rare-earth moments in the 1/T component on the relaxation rate below T_c, there are strong indications of highly localized supercurrents which are shielding the effects of the rare-earth moments from the muon probe.[147]

Present evidence would lead us to conclude that the mixed state is more of a glassy vortex state[148-152] and we attribute an additional non-linear part (approximate T^{-1} dependence) to a localized response to spin fluctuations of the rare-earth magnetic moments by the local shielding currents in the superconducting planes.[147] The muon, which typically localizes in the BaO planes, see the effect of these spin fluctuations in terms of a broadening of the distribution of local magnetic fields and, consequently, an increase in the relaxation rate which is proportional to $\frac{1}{T}$.

7.3   Interpretation of μ^+ bonding in R123y

In all of the samples of R123y, one site predominates regardless of the oxygen content, the so-called Balmer(2) site (B2). According to the ionic model, the site should shift toward the CuO-planes in the R1236 structures. Therefore, there is a certain necessity to explain this somewhat anomalous behavior.

We propose that the B2 site may be favored because the μ^+ forms a tetrahedral sp^3 bond with the oxygen orbitals, and the dsp^3 orbitals of the Cu in the CuO planes. The bond angle of the CuOμ structure is about $104°$ which is similar to the tetrahedral sp^3 hybridizations.

The implied sp^3 hybridization also places some interpretation on the nature of the Y123y material. By the evidence so far, the Y123y behaves as though the oxide superconductors possess a mixture of covalent and ionic bonding. Similar mixed covalent-Van der Waals bonding properties are observed for such material as mica, muscovite, and graphite. Many organic acids such as acetic acid (CH_3COOH) form a salts which are a mixture of a covalently bonded CH_3COO^- and an alkali metal ion such as Na^+, forming a mixture of ionic and covalent bonding between the CH_3COO^- and the Na^+, and Van der Waals bonding between individual units of CH_3COONa.

The R123y structures may possess similar properties to the porphyrins, a class of many biochemical compounds in which hemoglobin and chlorophyll are members.[153] The characteristic feature of the porphyrins is the heme group, another example of a mixture aromatic bonds, and ionic bonds. The heme electronic structure is essentially aromatic (metallic-like) on the pyrrole groups which surround the central Fe^{2+} or Fe^{3+}, yet ionic between the Fe and the N. The mixed ionic-covalent electronic behavior can be easily seen in the NMR spectrum of the porphyrins due to chemical shifts, and also hopping of the protons between the group of pyrrole substructures which form the core heme group.

It is notable that the proton NMR chemical shift for the H_xY1237 was about $\delta \approx -14$ relative to benzene at 316 K (see Appendix A for the definition of δ).[142] Because $\delta \approx 7$ for benzene (relative to TMS), we can conclude that the signal of the CuO planes will be shifted to $\delta \approx -7$ (relative to TMS). It would appear from the data presented that the chemical shift remains relatively constant with respect to the temperature. The orientation of the protons on the benzene ring is such that the field is enhanced (deshielded) at the proton sites, yielding a positive chemical shift ($\delta \sim 7$). The protons are located *outside* the hexagonal ring. If a proton probe were to be placed *inside* the ring structure (enclosed within the hexagonal ring), the proton on the inside ring would exhibit a negative chemical shift ($\delta \sim -7$). This type of negative chemical shift is commonly observed in conjugated hydrocarbons such as [18]Annulene ($\delta \sim -1.9$), which has protons located *inside* of the conjugated ring structure.[143] Another structure which has two methyl groups located *inside* of an aromatic pyrene-like structure is 15,16-dimethyldihydropyrene ($\delta \sim -4.2$). Finally, in an acidic environment, shielding ($\delta \sim -2$) has been observed for protons that hop between the nitrogens on the pyrrole rings *inside* the heme structure of porphyrins. It is therefore reasonable to postulate that the macroscopic behavior of these R123y structures may be locally analogous to the microscopic behavior of aromatic compounds like benzene especially at higher temperatures.

We already know that the majority of the conduction occurs in the CuO planes in the 1237 system.[154] The $CuO\mu$ bonding dsp^3 configuration suggests a strong covalently bonded CuO sheet, with

more ionic-like behavior in the BaO planes. We also see that muon-stop sites are basically independent of the concentration of oxygen in the sample. We see the same B2 like sites in Y1236 as we do in R1237. Finally, we see a chemical shift which is characteristic of aromatic compounds. The evidence would suggest the presence of a combination of covalent and ionic effects.[14-17] Therefore, it is reasonable to postulate that the bonding of the CuO superconductors is similar to the organic superconductors. Indeed, organic superconductors may achieve similar fame as their CuO predecessors in the coming years and may exhibit similar or possibly even higher values for T_c.

Finally, to conclude this chapter, we comment that this CuO organic-like structure strongly suggests that we may wish to consider these CuO superconductors in a different category from typical type-II superconductors. From the postulates set forth in this chapter, it follows that the nature of the CuO plane structures possess a bonding which is closely analogous to that seen for aromatic organic molecules.

We speculate that a likely driving mechanism for superconductivity is constraint of the conduction electrons to localized wave functions and therefore highly constrained paths--essentially an excitonic mechanism.[155-157] The presence of localized tetrahedral muon bonding suggests that the wave functions are still quite localized in their overlaps. In a metal, there would be an exponential relaxation rate. What we observe is Gaussian relaxation rates characteristic of localization. The high localization of the wave

functions would mean that the superconducting electrons are confined to very narrow channels in the CuO planes.

The bonding in aromatic compounds typically restricts the path of electrons to highly confined directions. The constrained electron paths suggest that a standard application of k-space transformations is not appropriate because the periodicity of the lattice is not exactly commensurate with the periodicity of the Bloch wave functions, which define the pathways which the electrons will take. In a normal metal, the energy levels associated with a particular Bloch wave function form a band due to the presence of a large number of electrons. The wave functions which are formed spread over large regions of the metal lattice, sometimes encompassing distances over a cm in length. On the other hand, in aromatic compounds, discrete energy levels are found which are the result of a smaller number of electrons: *i.e.*, the electrons are confined to highly localized orbitals, with paths on the order of 10 Å. Arbitrary application of k-space transformations may not be valid under these types of spatial restrictions.

The effects of rare-earth ions in μSR studies of R1237 suggest that there is the presence of highly localized electron currents in the high-T_c materials.[153] The strong localization would concur with the behavior of aromatic compounds. It therefore may suggest that an excitonic mechanism would most closely correspond to this system of superconducting materials.[155-157]

In the next chapter, we present the conclusions that we have obtained during the course of this thesis.

Chapter 8

Conclusions

In this chapter, we present our conclusions in the order on the chapters in which the material was first introduced.

Muon spin relaxation is a powerful magnetic resonance (MR) technique for elucidating the magnetic structures of magnetic materials, and the vortex structure of superconducting materials. This spectroscopy method leaves the sample relatively undisturbed during the process aside from the single probe that enters the sample during a given event. The result is a spectrum of a material which is not extensively altered from its original state. Typical MR probes are introduced by substitution of a non-MR probe for a MR probe. As a result, the chemical structure is invariable altered, introducing complications to the interpretation of the spectrum involve. Since muon probes are introduced one muon at a time, alterations to the chemical structure of the sample are reduced to the surface regions of the crystal where the muon is thermalized (~1000 Å).

Our computational model has successfully predicted the likely regions of muon localization, and the agreement with observation is surprisingly excellent. We interpret this success to mean that our original assumption--these transition metal oxides have a considerable degree of ionic behavior--may indeed be correct. The presence of observable μSR frequencies is another hint, since the

muon would not bond to oxygens actively involved with the conduction process. These results also suggest that a tight-binding approximation of the bandstructure of these cuprates may yield reasonable results in qualitative agreement with the observed experimental data. The bandstructure calculations, which have been completed, concur with the assumed average valence of the oxygens and coppers in the potential energy calculations, and agree with the experimental values for the effective mass of the electrons.

The candidate muon-stop sites for $(Pr_xY_{1-x})Ba_2Cu_3O_7$ $(0 < x < 1)$ are located in about the same regions as the other $RBa_2Cu_3O_{6+\delta}$ $(\delta = 1)$ sites. Antiferromagnetic ordering of the Cu moments occurs below 280 K (for $0.6 < x < 1.0$). Based upon neutron diffraction, μSR, and other experiments on $YBa_2Cu_3O_{6+\delta}$ $(0.0 < \delta < 0.4)$, we predict (for $T_{N2} < T < T_{N1}$) that the magnetic moments are the result of copper magnetism from the copper ions located in the CuO planes, that the magnitude of the magnetic moment is 0.27 μ_B, and that the direction of the Cu magnetic moment is along the a axis.

In order to explain the muon frequency shift at T_{N2} as a function of the Pr concentration of $(Pr_xY_{1-x})1237$ $(0.55 \leq x \leq 1.00)$, we have considered several magnetic structure models. The anomalous shift is likely due to additional Cu chain antiferromagnetism; the Tranquada model--$T < T_{N2}$ in $YBa_2Cu_3O_{6+\delta}$ $(\delta = .10, .35)$--is the most suitable for describing this unusual magnetic effect.[89-90] Additional reduced Pr magnetism may only be considered in conjunction with copper chain magnetism; Pr magnetism alone predicts an increase, not a decrease, at T_{N2} in the observed muon frequency for Pr1237.

One possible source of the unusual effects, which have often been attributed to Pr, may be the result of induced magnetism as suggested by M. Weber for Er1237.

The candidate sites in Pr1236 are similar to those seen in R1236 with the notable absense of the Denny site (see chapter four for a complete list of site locations and potentials). The probable reason for this is the presence of Pr^{4+}, a valence which is larger that other R^{3+} ions. We predict Cu magnetism in the planes in this material with a magnetic moment, $\mu_{Cu(pl)} = 0.5\ \mu_B$--a factor of two larger than Pr1237 and in close proximity of the magnitude seen in Y1236 and $H_x Y1237$.

Studies on $PrBa_2(Al_x Cu_{1-x})_3 O_7$ show two signals above 14 K. One signal similar to that seen in Pr1237 is from the Cu(2) moments $\mu_{Cu(pl)} = 0.27\ \mu_B$, and the other signal is due to the substitution of Cu(2) for Al yielding a magnetic vacancy.

There is no observed frequency anomaly at T_{N2} in Pr1236 and Al-doped Pr1237. However, there is a possible hint of a frequency shift for Pr1236 at roughly the same temperature as Pr1237 (T ~ 17 K). The origin of this shift may also be the result of induced paramagnetism.[158]

The hydrogen appears to behave in a similar fashion to the muon in the R123y system. Major evidence is that the muon competes for the same site as the H in the $H_x Y1237$ structure, and, as a result, the intensity of the muon signal (asymmetry) changes as a consequence of occupation of the B1 site. The proton NMR spectrum of $H_x Y1237$ suggests that the H is seeing two different magnetic

fields at the B2 site. The change in the a and c lattice constants (and no change in b) also suggest that the H^+ is occupying a site in the xz plane which would most easily be explained as the B2 site. Neutron diffraction data for $H_x Y1237$ can also be interpreted in terms of the B2 site. The IR data by Yang *et al.* suggesting CuH bonding[143] appears to be the result of the formation of a hydride phase in the sample of Y1237. We conclude, therefore, that the H^+ occupies the same sites as the muon.

In the mixed state of superconducting R123y, we interpret the μSR data to indicated a vortex state which is not characteristic of a canonical type II superconductor. We anticipate a glassy superconductor based upon μSR vortex data.

The predicted electronic structure which we see from this R1237 compound is one of mixed covalent and ionic character. We predict a covalently bonded CuO structure with a virtually ionic contribution from the barium ions and the rare-earth ions which balances the charge distribution. The structure shares a close relationship with the organic superconductors, showing similar highly localized wave function overlaps roughly analogous to the aromatic compounds. In light of recent discoveries of an 18 K (and higher T_c) organic superconductor (the K-fullerene[159] and the CsRb-fullerene[160]), it would seem to be of little surprise to see the organic superconductors eventially achieve similar or higher T_c values than the CuO superconductors which were studied in the body of this thesis.

Appendix

Definition of δ in NMR spectroscopy

In organic chemistry, chemical shifts (often called Knight shifts in physics) are measured in parts per million (ppm) relative to a standard reagent trimethylsilane (TMS). Usually a magnetic field is defined in units of Tesla or Gauss. In chapter two, it was shown that the magnitude of the magnetic field seen at the NMR probe site is proportional to the frequency

$$f = (\gamma/2\pi) \, |H|,$$

where γ is the gyromagnetic ratio or the NMR probe.[35,36] Therefore, it is also possible to define the magnitude of the field in terms of frequency, an approach which is more convenient in NMR. In organic NMR analysis, magnetic field and hyperfine coupling constants are usually described in units of frequency (typically MHz). The value of δ (in ppm) is defined as

$$\delta = (H_{TMS} - H_{sample})/H_{TMS},$$

where δ is a frequency independent value, H_{TMS} is the resonant frequency of a sample of TMS, and H_{sample} is the resonant frequency of the sample in question. The protons in a material are sensitive to the surrounding local electronic environment. The response of the

electrons to the external magnetic field is recorded in an NMR spectrum. Protons which are exposed to a local field which is parallel to the external field will exhibit a positive chemical shift ($\delta > 0$), a phenomenon referred to as deshielding. On the other hand, protons, which are in a local environment where the local field is opposite to the externally applied field, will see a negative chemical shift ($\delta < 0$), a phenomenon known as shielding.

References

Format according to Physical Review B.

1. J.G. Bednorz and K.A. Müller. Z. Phys. B **64**, 189 (1986).

2. M.K. Wu, J.R. Ashburn, C.J. Torng, P.H. Hor, R.L. Meng, L. Gao, Z.J. Huang, Y.Q. Wang, and C.W. Chu. Phys. Rev. Lett. **58**(9), 908 (1987).

3. P. Hor, L. Gao, R.L. Meng, Z.J. Huang, Y.Z. Wang, K. Forster, J. Vassilious, and C.W. Chu. Phys. Rev. Lett. **58**(9), 911 (1987).

4. K. Yvon and M. François. Z. Phys. B -- condensed matter **76**, 413 (1989).

5. C. Boekema , A.B. Denison, D.W. Cooke, R.H. Heffner, R.L. Hutson, M. Leon, and M.E. Schillaci. Hyperfine Int. **15-16**, 529 (1983).

6. C. Boekema. Hyperfine Int. **17-19**, 305 (1983); and references therein.

7. C. Boekema, R.L. Lichti, K.C.B. Chan, V.A.M. Brabers, A.B. Denison, D.W. Cooke, R.H. Heffner, R.L. Hutson, and M.E. Schillaci. Phys. Rev. B **33**(1), 210 (1986).

8. C. Boekema, R.L. Lichti, V.A.M. Brabers, A.B. Denison, D.W. Cooke, R.H. Heffner, R.L. Hutson, M. Leon, and M.E. Schillaci. Phys. Rev. B **31**(3), 1233 (1985).

9. K.-C. Chan, Doctoral Thesis, Texas Tech University (1987).

10. D. P. Spencer, D.G. Fleming, and J.H. Brewer. Hyperfine Int. **17-19**, 576 (1984).

11. C. Boekema, A.B. Denison, and K.J. Rüegg. J. Mag. Mag. Mat. **36**, 111 (1983).

12. K. Rüegg, C. Boekema, A. Denison, W. Hofmann, and W. Kündig. J. Mag. Mag. Mat. **15-18**, 669 (1980);

13. K.J. Rüegg, C. Boekema, W. Kündig, P.F. Meier, and B.D. Patterson. Hyperfine Int. **8**, 574 (1981).

14. W. K. Dawson, K. Tibbs, S.P. Weathersby, C. Boekema, and K.C.B. Chan. J. Appl. Phys. **64**, 5809 (1988).

15. C. H. Halim, W.K. Dawson, W.A. Baldwin, and C. Boekema. Physica B.**163**, 453 (1990).

16. W. K. Dawson, C.H. Halim, S.P. Weathersby, J.A. Flint, J.C. Lam, T.J. Hoffman, C. Boekema, KC.B. Chan, R.L. Lichti, D.W. Cooke, M.S. Jahan, and J.E. Crow. Hyperfine Int. **63**, 219 (1990).

17. W. K. Dawson, J.C. Lam, C. Boekema, R.L. Lichti, D.W. Cooke, J.E. Crow. J. Appl. Phys. **69**(8), 5385 (1991).

18. H. Glückler, A. Weidinger, A. Golnik, Ch. Niedermayer, M. Rauer, R. Simon, E. Recknagel, J.I. Budnick, W. Paulus, and R. Schöllhorn. Physica C **162-164**, 149 (1989).

19. H. Glückler, Ch. Niedermeyer, G. Nowitzke, A. Golnik, R. Simon, E. Recknagel, A. Weidinger, J. Erxmeyer, J.I. Budnick. Hyperfine Int. **63**, 155 (1990).

20. Ch. Niedermayer, H. Glückler, R. Simon, A. Golnik, M. Rauer, E. Recknagel, A. Weidinger, J.I. Budnick, W. Paulus, and R. Schöllhorn. Phys. Rev. B **40**(16), 11386 (1989).

21. D.W. Cooke, R. S. Kwok, M.S. Jahan, R.L. Lichti, T.R. Adams, C. Boekema, W.K. Dawson, A. Kebede, J. Schwegler, J.E. Crow, T. Mihalisin, Phys. Rev. B **41**(7), 4801 (1990).

22. D.W. Cooke, R.S. Kwok, and M.S. Jahan, R.L. Lichti, T.R. Adams, C. Boekema, W.K. Dawson, A. Kebede, J. Schwegler, J.E. Crow, and T. Mihalisin, J. Appl. Phys. **67**(9), 5061 (1990).

23. D.W. Cooke, M.S. Jahan, and R.S. Kwok, R.L. Lichti, T.R. Adams, C. Boekema, W.K. Dawson, A. Kebede, J. Schwegler, J.E. Crow, and T. Mihalisin, μSR90 Conference Proceedings Hyperfine Interactions **63**, 213 (1990).

24. P. D. De Gennes. Superconductivity of metals & alloys, (Benjamin, New York, 1966) p. 26.

25. P. Pincus, A.C. Gossard, V. Jaccarino, and J. Wernick. Phys. Lett. **13**, 21 (1964).

26. M. Tinkham. Introduction to Superconductivity, (McGraw-Hill, New York, 1975).

27. A. A. Abrikosov. Zh. Eksp. Teor. Fiz. **32**, 1442 (1957).

28. Y. J. Uemura, G.M. Luke, B.J. Sternlieb, J.H. Brewer, J.F. Carolan, W.N. Hardy, R. Kadono, J.R. Kempton, R.F. Kiefl, S.R. Kreitzman, P. Mulhern, T.M. Riseman, D.Ll. Williams, B.X. Yang, S. Uchida, H. Takagi, J. Gopalakrishnan, A.W. Sleight, M.A. Subramanian, C.L. Chien, M.Z. Cieplak, Gang Xiao, V.Y. Lee, B.W. Statt, C.E. Stronach, W.J. Kossler, and X.H. Yu. Phys. Rev. Lett. **62**(19), 2317 (1989).

29. A. Schenk. Muon Spin Rotation Spectroscopy. (Hilger, Bristol (UK) 1985).

30. S.F. Cox. J. Phys. C **20**, 3187 (1987).

31. C. Boekema, Chapters and Lecture Notes on "Muon Spin Research in Oxide Materials" in The Time Domain in Dynamics eds. G. Long and F. Grandjean (Kluwer Academic: Dordrecht (NL) 1988) pp. 377-438, and references therein.

32. C. Boekema, R.L. Lichti, A.B. Denison, A.M. Brabers, D.W. Cooke, R.H. Heffner, R.L. Hutson, and M.E. Schallaci. Hyperfine Int. **31**, 487 (1986).

33. K.-C.B. Chan, R.L. Lichti, C. Boekema, A.B. Denison, D.W. Cooke, and M.E. Schallaci. Hyperfine Int. **31**, 481 (1986).

34. C. Boekema K.C.B. Chan, R.L. Lichti, A.B. Denison, D.W. Cooke, R.H. Heffner, R.L. Hutson, and M.E. Schillaci. Hyperfine Int. **32**, 667 (1986).

35. Atta-ur-Rahman. Nuclaer Magnetic Resonance, Basic Principles (Springer-Verlag, New York Inc.: New York, 1986).

36. Robin K. Harris. Nuclaer Magnetic Resonance Spectroscopy, A Physiochemical View (Longman Scientific & Technical: Burnt Hill, Harlow, Essex, 1986).

138

37. I. Svare.   Phys. Rev. B **40**(13), 8641 (1989).

38. R. Jones. Ab Initio Methods in Quantum Chemistry, K. P. Lawley eds. (John Wiley & Sons, Inc. New York: 1987) pp 413-437; and references therein.

39. A.N. Cormack, P. Saul, and C.R.A. Catlow. Physica B **131**, 139 (1985).

40. K. Rüegg, private communication.

41. P. Morse. Physical Review **29**, 57-64 (1929).

42. E. Lippincott and R. Schroeder. J. Chem. Phys. **23**, 1131 (1955).

43. E. Lippincott and R. Schroeder. J. Amer. Chem. Soc. **78**, 5171 (1956).

44. E. Lippincott. J. Chem. Phys. **26**, 678 (1957).

45. J.B. Bates, J.C. Wang, and R.A. Perkins. Phys. Rev. B **19**(8), 4130 (1979).

46. J.B. Bates, and R.A. Perkins. Phys. Rev. B **16**(8), 3713 (1977);

47. P.E. Cade. J. of Chem. Phys. **47**(7), 2390 (1967).

48. K.-C. Chan, private communications.

49. C. Kittel. Introduction to Solid State Physics, 6th ed. (John Wiley & Sons, Inc. New York: 1986) pp. 303-304.

50. G.C. Pimentel and A.L. Mc.Clellan. The Hydrogen Bond. (W.A. Freemam and Co., 1960).

51. S.H. Vinogrodov and R.H. Linnell. Hydrogen Bonding. (Van Nostrand, Reinhold 1971).

52. R. Waser. Ber. Bunsenges. Phys. Chem. **90**(12), 1123 (1986).

53. G. Weber, S. Kapphan, and M. Wöhlecke. Phys. Rev. B **34**(12), 8406 (1986).

54. Herbert Engstrom, J.B. Bates, J.C. Wang, and M.M. Abraham. Phys. Rev. B **21**(4), 1520 (1980).

55. F. G. Gärtner, and E. Mollwo. Phys. Stat. Sol. B **90**(33), 33 (1978).

56. R. Gonzolez, Y. Chen, K.L. Tsang, and G.P. Summers. Appl. Phys. Lett. **41**(8), 739 (1982).

57. C. Boekema, unpublished.

58. C. Kittel. (Reference 49) pp. 606-610.

59. P. P. Ewald. Ann. Physik **64**, 253 (1921).

60. W. Jones & N. March. Theoretical Solid State Physics. (John Wiley & Sons, Inc. New York: 1973) pp. 613-615.

61. S. W. Leeuw and J.W. Perram. Molec. Phys. **37**(4), 1313 (1979).

62. Tim Clark. A Handbook of Computational Chemistry, A Practical Guide to Chemical Structure and Energy Calculations. (John Wiley & Sons, Inc. New York: 1985) pp. 233-317; Leonard I. Schiff. Quantum Mechanics. 3rd ed. (McGraw Hill, New York: 1968) pp. 255-263. David Park. Introduction to the Quantum Theory. 2nd ed. (McGraw Hill, New York: 1974) pp. 289-294.

63. Donald A. McQuarrie. Quantum Chemistry (University Science Books, Mill Valley CA: 1983) p. 279 (problem 10).

64. R.L. Lichti, T.R. Adams, and T.L. Gibson. Hyperfine Int. **63**, 199 (1990).

65. R.L. Lichti and T. Adams, private communications and reference 64; S. Barth, P. Birrer, F.N. Gygax, B. Hitti, F. Hullinger, E. Lippelt, H. R. Ott, and A. Schenck. Physica C **153-155**, 767 (1988); A. Golnik, J.I. Budnick, B. Chamberland, L. Lynde, Ch. Niedermayer, F. Otter, E. Recknagel, M. Rossmanith, A. Weidinger, and Z. Tan. Physica C **153-155**, 166 (1988).

66. D. McK. Paul, H.A. Mook, A.W. Hewat, B.C. Sales, L.A. Boatner, J.R. Thompson, and Mark Mostoller. Phys. Rev. B **37**(4), 2341 (1988).

67. Y. Kuno, N. Nishida, H. Miyatake, S. Okuma, Y. Watanabe, T. Yamazaki, M. Ishikawa, T. Takabatake, Y. Makazawa, J.H. Brewer, S.P. Kreitzman, and T.M. Riseman. Phys. Rev. B **38**(13), 9276 (1988).

68. H.A. Mook, D. McK Paul, B.C. Sales, L.A. Boatner, and L. Cussen. Phys. Rev. B **38**(16), 12008 (1988).

69. J. Brewer, private communications.

70. T. Chattopadhyay, H. Maletta, W. Wirges, K. Fisher, and P.J. Brown. Phys. Rev. B **38**(1), 838 (1988).

71. Y. Le Page, T. Siegrist, S.A. Sunshine, L.F. Schneemeyer, D.W. Murphy, S.M. Zahurak, J.V. Waszczak, W.R. McKinnon, J.M. Tarascon, G.W. Hull, and L.H. Greene. Phys Rev B **36**(7), 3617 (1987).

72. J.B. Boyce, F. Bridges, T. Claeson, R.S. Howland, and T.H. Geballe. Phys. Rev. B **36**(10), 5251 (1987).

73. J.E. Greedan, A.H. O'Reilly, C.V. Stager. Phys. Rev. B **35**(16), 8770 (1987).

74. N. Nishida, H. Miyatake, S. Okuma, Y. Kuno, Y. Watanabe, T. Yamazaki, S. Hikami, M. Ishikawa, T. Takabatke, Y. Nakazawa, S.R. Kreitzmann, J.H. Brewer, and Ch.-Y. Huang. J. Jour. Appl. Phys. **27**(1), L94 (1988).

75. P. Birrer, F.N. Gygax, B. Hitti, E. Lippelt, A. Schenck, and M. Weber. Phys. Rev. B **39**(16), 11449 (1989).

76. T.K. Lin, L. Lichti, C. Boekema, and A.B. Denison. Hyperfine Int. **31**, 475 (1986).

77. E. Holzschuh, A.B. Denison, W. Kündig, P.F. Meier, B.D. Patterson. Phys. Rev. B **27**(9), 5294 (1983).

78. C. Boekema, R.L. Lichti, and K.J. Rüegg. Phys. Rev. B **30**(11), 6766 (1984).

79. P. Balmer, H. Blum, M. Forster, A. Schweiger, and Hs.H. Gunthard. J. Phys. C **13**(4), 517 (1980); P. Balmer *et al.*, Helv. Phys. Acta **43**, 829 (1970).

80. H. Blum, R. Frey, Hs.H. Gunthard, and J.-K. Ha. Chem. Phys. **2**(3), 262 (1973).

81. D. W. Cooke, R.L. Hutson, R.S. Kwok, M. Maez, H. Rempp, M.E. Schillaci, R.L. Lichti, K.C. B. Chan, C. Boekema, S.P. Weathersby, J.A. Flint, and J. Oostens, Phys. Rev. B **37**(16), 9401 (1988).

82. D. W. Cooke, R.L. Hutson, R.S. Kwok, M. Maez, H. Rempp, M.E. Schillaci, J.L. Smith, J.O. Willis, R.L. Lichti, K.C.B. Chan, C. Boekema, S.P. Weathersby, and J. Oostens, Phys. Rev. B **39**(4), 2748 (1989).

83. R. L. Lichti, K.C.B. Chan, D.W. Cooke, and C. Boekema. Appl. Phys. Lett. **54**(23), 2361 (1989); D.W. Cooke *et al.*, APS Bulletin **33**, 734 (1988); C. Boekema *et al.*, APS Bulletin **33**, 735 (1988).

84. J.I. Budnick, A. Golnik, Ch. Niedermayer, E. Recknagel, M. Rossmanith, A. Weidinger, B. Chamberland, M. Filipkowski, and D.P. Yang. Phys. Lett. A **124**, 103 (1987).

85. A. Golnik, Ch. Niedermayer, E. Recknagel, M. Rossmanith, A. Wiedinger, J. Budnick, B. Chamberland, M. Filipkowsky, Y. Zhang, D. P. Yang, L. Lynds, F. Otter, and C. Baines. Phys. Lett. A **125**, 71 (1987).

86. Y. J. Uemura, W.J. Kossler, X.H. Yu, J.R. Kempton, H.E. Schone, D. Opie, C.E. Stronach, D.C. Johnston, M.S. Alvalez, and D.P. Goshorn. Phys. Rev. Lett. **59**, 1045 (1987); and references 102-105.

87. K.C. Chan *et al.*, APS Bulletin **33**, 734 (1988).

88. J. W. Lynn and W-H. Li. J. Appl. Phys. **64**(10), 6065 (1988); and reference 114.

89. A. H. Moudden, G. Shirane, J.M. Tranquada, R. Birgeneau, Y. Endoh, K. Yamada, Y. Hidaka, and T. Murakami. Phys. Rev. B **38**(13), 8720 (1988).

90. J. M. Tranquada. J. Appl. Phys. **64**(10), 6071 (1988).

91. H. Kadowaki, M. Hishi, Y. Yamada, H. Takeya, H. Takei, S.M. Shapiro, and G. Shirane. Phys. Rev. B **37**(13), 7932 (1988).

92. N. Nishida, H. Miyatake, D. Shimada, S. Okuma, T. Yamazaki, Y. Watanabe, Y. Kuno, M. Ishakawa, T. Takabatake, K. Hagamine, K. Hishayama, J.H. Brewer, and S.R. Kreitzmann. Physica C **153-155**, 761 (1988).

93. N. Nishida, H. Miyatake, D. Shimada, S. Okuma, M. Ishikawa, T. Takabatake, Y. Nakazawa, Y. Kuno, R. Keitel, J.H. Brewer, T.M. Riseman, D.Ll. Williams, Y. Watanabe, T. Yamazaki, K. Nishiyama, K. Nagamine, E.J. Ansaldo, and E. Torikai. J. Phys. Soc. of Japan **57**(2), 597 (1988).

94. C. Boekema *et al.*, Ref. 11 and in preparation.

95. R. L. Lichti, K.C.B. Chan, T.R. Adams, C. Boekema, W.K. Dawson, J.A. Flint, D.W. Cooke, R.S. Kwok, and J.O. Willis, J. Appl. Phys. **67**(9), 5055 (1990).

96. Levente Szasz. Pseudopotential Theory of Atoms and Molecules. (John Wiley & Sons, Inc. New York, Chichesher, Brisbane, Toranto, Sinapore: 1985).

97. G.A. Thomas, J. Orenstein, D.H. Rapkine, M. Capizzi, A.J. Millis, R.N. Bhatt, L.F. Schneemeyer, and J.V. Waszczak. Phys. Rev. Lett. **61**(11), 1313 (1988).

98. J. H. Brewer, E.J. Ansaldo, J.F. Carolan, A.C.D. Chaklader, W.J. Hardy, D.R. Harshman, M.E. Hayden, M. Ishikawa, N. Kaplan, R. Keitel, J. Kempton, R.F. Kiefl, W.J. Kossler, S.R. kreitzman, A. Kulpa, Y. Kuno, G.M. Lake, H. Kiyatake, K. Hagamine, Y. Nakazawa, N. Nishida, K. Hishiyama, S. Ohkuma, T.M. Riseman, G. Roehmer, P. Schleger, D. Shimada, C.E. Stronach, T. Takabatake, Y.J. Uemura, Y. Watanabe, D.Ll. Williams, T. Yamazaki, and B. Yang. Phys. Rev. Lett. **60**(11), 1073 (1988).

99. G. Aeppli, R.J. Cava, E.J. Ansaldo, J.H. Brewer, S.R. Kreitzman, G.M. Luke, D.R. Noakes, and R.F. Kiefl, Phys. Rev. B **35**(13), 7129 (1987).

100. W.J. Kossler, J. R. Kempton, X.H. Yu, H.E. Schone, Y.J. Uemura, A.R. Moodenbaugh, M. Suenaga, and C.E. Stronach, Phys. Rev. B **35**(13), 7133 (1987).

101. D. H. Harshman, G. Aeppli, E.J. Ansaldo, B. Batlogg, J.H. Brewer, J.F. Carolan, R.J. Cava, M. Celio, A.C.D. Chaklader, W.N. Hardy, S.R. Kreitzman, G.M. Luke, D.R. Noakes, and M. Senba, Phys. Rev. B 36(4), 2386 (1987).

102. F.N. Gygax, B. Hitti, E. Lippelt, A. Schenck, D. Cattani, J. Cors, M. Decroux, O. Fischer, and S. Barth. Europhys. 4, 473 (1987).

103. J.W. Schneider, Hp. Baumeler, H. Keller, W. Odermatt, B.D. Patterson, K.A. Müller, J.G. Bednorz, K.A. Blazey, and I. Morganstern. Phys. Lett. A 124(1,2), 107 (1987).

104. F.N. Gygax, B. Hitti, E. Lippelt, A. Schenck, S. Barth, and K. Kwasnitza. Phys. Lett. A 127(8,9), 447 (1988).

105. C. Bucci R. De Renzi, G. Guidi, M. Riccò, R. Tedeschi, F. Licci, G.H. Eaton, and C.A. Scott. Phys. Lett. A 127(8,9), 115 (1988).

106. Z. Fisk, J.D. Thompson, E. Zirngiebl, J.L. Smith, and S-W. Cheong. Solid State Commun. 62, 743 (1987).

107. Chan-Soo Jee, A. Kebede, T. Yuen, S.H. Bloom, M.V. Kuric, J.E. Crow, R.P. Guertin, T. Mihalisin, G.H. Myer, and P. Schlottmann. J. of Mag. and Mag. Mat 76-77, 617 (1988).

108. A. Kebede, Chan-Soo Jee, D. Nichols, M.V. Kuric, J.E. Crow, R.P. Guertin, T. Mihalisin, G.H. Myer, I. Perez, R.E. Salomon, and P. Schlottmann. J. Mag. and Mag. Mat. 76-77, 619 (1988).

109. A. Kebede, Chan-Soo Jee, J. Schwegler, J.E. Crow, T. Mihalisin, G.H. Myer, R.E. Salomon, P. Schlottmann, M.V. Kuric, S.H. Bloom, R.P. Guertin. Phys. Rev. B 40(7), 4453 (1989); and reference 113.

110. W-H. Li, J. W. Lynn, S. Skanthakumar, T.W. Clinton, A. Kebede, C.-S. Jee, J.E. Crow, and T. Mihalisin. Phys. Rev. B 40(7), 5300 (1989).

111. general (a) Z. Fisk, Solid State Commun. 62, 743 (1987).

112. S. Skanthakumar,W-H. Li, J.W. Lynn, A. Kebede, J.E. Crow, and T. Mihalisin. Physica B 163, 239 (1990); and reference 110.

113. M. E. López-Moralez, D. Rios-Jara, J. Tagüeña, R. Escudero, S. La Placa, A. Bezinge, V.Y. Lee, E.M. Engler, and P.M. Grant. Phys. Rev. B **41**, 6655 (1990).

114. H-W. Li, J.W. Lynn, and Z. Fisk. Phys. Rev. B **41**(7), 4098 (1990).

115. T. M. Riseman, J.H. Brewer, E.J. Ansaldo, P.M . Grant, M.E. López-Morales, and B.M. Sternlieb. μSR90 Conference Proceedings Hyperfine Int. **63**, (1990).

116. J. H. Brewer. Physica C **162-164**, 157 (1989).

117. Y. Dalichaouch, M.S. Torikachvili, E.A. Early, B.W. Lee, C.L. Seaman, K.N. Yang, H. Zhau, and M.B. Maple. Solid State Commun. **65**(9), 1001 (1988).

118. F.W. Lytle, G. van der Laan, R.B. Greegor, E.M. Larson, C.E. Violet, and Joe Wong. Phys. Rev. B **41**(13), 8955 (1990).

119. J.J. Neumeier, T. Bjørnholm, M.B. Maple, J.J. Rhyne, and J.A. Gotaas. Physica C **166**, 191 (1990); and references 131-134.

120. M. Weber. μSR90 Conference Proceedings Hyperfine Int. **63**, (1990).

121. W-H. Li, J.W. Lynn H.A. Mook, B.C. Sales, and Z. Fisk. Phys. Rev. B **37**(16), 9844 (1988).

122. J. M. Tranquada, A.H. Moudden, A.I. Goldman, P. Zolliker, D.E. Cox, G. Shirane, S.K. Sinha, D. Vaknin, D.C. Johnston, M.S. Alvarez, A.J. Jacobson, J.T. Lewandowski, and J.M. Newsam. Phys. Rev. B **38**(4), 2477 (1988).

123. J. M. Tranquada, D.E. Cox, W. Kunnmann, H. Moudden, G. Shirane, M. Suenage, P. Zolliker, D. Vaknin, S.K. Sinha, M.S. Alvarez, A.J. Jacobson, and D.C. Johnston. Phys. Rev. Lett. **60**(2), 156 (1988).

124. B. X. Yang, T.R. Thurston, J.M. Tranquada, and G. Shirane. Phys. Rev. B **39**(7), 4343 (1989).

125. G. Y. Guo and W. M . Temmerman. Phys. Rev. B **41**, 6372 (1990).

126. Mc. Laughlin, APS conference, **35**, G16.7 and G16.8, (1990).

127. A. P. Reyes, E.E. MacLaughlin, M. Takigawa, P.C. Hammel, R.H. Heffner, J.D. Thompson, J.E. Crow, A. Kebede, T. Mihalisin, J. Schwegler. Phys. Rev. B **42**(4), 2688 (1990).

128. H. Lütgemeier, R.A. Brand, Ch. Sauer, B. Rupp, P.M. Meuffels, and W. Zinn. Physica C **162-164**, 1367 (1989).

129. D.W. Cooke *et al.*, work done at LAMPF, private communitations--to be published at some future date.

130. J. W. Lynn, W-H. Li, H.A. Mook, B.C. Sales, and Z. Fisk. Phys. Rev. Lett. **60**(26), 2781 (1988); and references 122-123.

131. T. Siegrist, L.F. Schneemeyer, J.V. Waszczak, N.P. Singh, R.L. Opila, B. Batlogg, L.W. Rupp, and D.W. Murphy. Phys. Rev. B **36**(16), 8365 (1987).

132. J.M. Tarascon, P. Barboux, P.F. Miceli, L.H. Greene, G.W. Hull, M. Eibschutz, and S. A. Sunshine. Phys. Rev. B **37**(13), 7458 (1988).

133. Zh-X Cai, and S.D. Mahanti. Phys. Rev. B **40**(10), 6558 (1989).

134. J. L. Peng, P. Klavins, R.N. Shelton, H.B. Radousky, P.A. Hahn, and L. Bernardez. Phys. Rev. B **40**, 4517 (1989).

135. M. Sano, H. Inokuchi, M. Kobayashi, S. Kaneiwa, and I. Tsujikawa. J. Chem. Phys. **72**(6), 3840 (1980).

136. R. Stockmeyer, H. Stortnik, and R. Wagner. Ber. Bunsenges. Phys. Chem. **82**(12), 1314 (1978).

137. P.C. Strangeby, O. Auciello, A.A. Haasz, and B.L. Doyle. J. Nucl. Mater. **123**(1-3), 1592 (1984).

138. J.J. Reilly, M. Suenaga, J.R. Johnson, P. Thompson, and A.R. Moodenbaugh. Phys. Rev. B **36**(10), 5694 (1987).

139. M. Nicolas, J.N. Daou, I. Vedel, P. Vajda, J.P. Burger, J. Lesueur, and L. Dumoulin. Solid State Comm. **66**(11), 1157 (1988).

140. H. Fujii, H. Kawanaka, W. Ye, Sh. Orimo, and H. Fukuba. Jpn. J. Appl. Phys. **27**(4), L525 (1988).

141. I. Natkaniec, A.V. Belushkin, J. Brankowski, E.A. Goremychkin, J. Mayer, I.L. Sashin, V.K. Fedotov, A.I. Koleshikov, I.O. Bashkin, V.V. Sinicyn, and E.G. Ponyatovskii. Physica C **162-164**, 1369 (1989).

142. S. D. Goren, C. Korn, V. Volterra, M. Schaefer, H. Riesemeier, E. Rössler, H. Stenschke, H.M. Vieth, and K. Lüders. Solid State Comm. **70**(3), 279 (1989).

143. T. Kato, K. Usami, J. Kuniya, and Sh.-P Matsuda. Jpn. J. Appl. Phys. **27**(6), L1104 (1988).

144. T. Kamiyama, S. Tomiyoshi, M. Omori, H. Yamauchi, T. Kajitani, T. Matsunaga, and H. Yamamoto. Physica B **148**, 491 (1987).

145. C. Y. Yang, X.-Q. Yang, S.M. Heald, J.J. Reilly, T. Skotheim, A.R. Moodenbaugh, and M. Suenaga. Phys. Rev. B **36**(16), 8798 (1987).

146. H. Nishihara, N. Hishida, T. Takabatake, K. Kishio, A. Ohtomo, K. Hayashi, M. Ishikawa, Y. Nakazawa, K.-I. Koga, Ts. Tamegai, and K. Kitazawa. Jpn. J. Appl. Phys. **27**, 1652 (1988).

147. R.L. Lichti, D.W. Cooke, and C. Boekema. Phys. Rev. B **43**(1), 1154 (1991).

148. P. L. Gammel, L.F. Schneemeyer, J.V. Waszczak, and D.J. Bishop. Phys. Rev. Lett. **61**(14), 1666 (1988).

149. C.A. Murry, P.L. Gammel, D.J. Bishop, D.B. Mitzi, and A. Kapitulnik. Phys. Rev. Lett. **64**(19), 2312 (1990).

150. Matthew P. A. Fisher. Phys. Rev. Lett. **62**(12), 1415 (1989).

151. C. Rossel, Y. Maeno, and I. Morgenstern. Phys. Rev. Lett. **62**(6), 681 (1989).

152. R. H. Koch, V. Foglietti, W.J. Gallagher, G. Koren, A. Gupta, and M.P.A. Fisher. Phys. Rev. Lett. **63**(14), 1511 (1989).

153. T.W. Grahm Solomons. <u>Organic Chemistry</u>, 3rd ed. (John Wiley & Sons, Inc. New York, Chichesher, Brisbane, Toranto, Sinapore: 1984) pp. 463, 938, and 1055.

154. This fact is mentioned in virtually every theoretical band structure calculation published to date; an early example would be L.F. Mattheiss. Phys. Rev. Lett. **58**(10), 1023 (1987).

155. W.A. Little. Phys. Rev. **134**(6A), A1416 (1964).

156. D. Davis, H. Gutfreund, and W.A. Little. Phys. Rev. B **13**(11), 4766 (1976).

157. L. Lam, Molec. Cryst. Liq. Cryst. **155**, 531-538 (1988); K. Arya, unpublished (submitted to Phys. Rev. B).

158. M. Weber, private communication.

159. A.F. Hebbard, M.J. Rosseinsky, R.C. Hadden, D.W. Murphy, S.H. Glarum, T.T.M. Palstra, A.P. Ramirez, and A.R. Kortan, Nature Magazine **350**(6319), 600 (1991).

160. Proceedings from the conference Materials and Mechanisms of Superconductivity for High Temperature Superconductivity. July 22-27 1991, to be publish in Physica C.